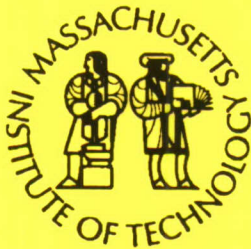


**Massachusetts Institute of Technology  
Woods Hole Oceanographic Institution**



**Joint Program  
in Oceanography/  
Applied Ocean Science  
and Engineering**



---

**DOCTORAL DISSERTATION**

The Dynamics of Oceanic Transform Faults:  
Constraints from Geophysical, Geochemical  
and Geodynamical Modeling

by

Patricia Michelle Marie Gregg

June 2008

**20080909177**

**MIT/WHOI**

**2008-06**

**The Dynamics of Oceanic Transform Faults:  
Constraints from Geophysical, Geochemical and Geodynamical Modeling**

by

Patricia Michelle Marie Gregg

Massachusetts Institute of Technology  
Cambridge, Massachusetts 02139

and

Woods Hole Oceanographic Institution  
Woods Hole, Massachusetts 02543

June 2008


**DOCTORAL DISSERTATION**

Funding was provided by the National Science Foundation Graduate Research Fellowship, Hollister Fellowship, and the Woods Hole Oceanographic Institution Academic Programs Office.

Reproduction in whole or in part is permitted for any purpose of the United States Government. This thesis should be cited as: Patricia Michelle Marie Gregg, 2008. The Dynamics of Oceanic Transform Faults: Constraints from Geophysical, Geochemical and Geodynamical Modeling. Ph.D. Thesis. MIT/WHOI, 2008-06.

Approved for publication; distribution unlimited.

**Approved for Distribution:**

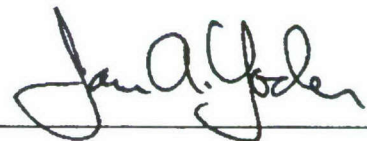


**Susan E. Humphris, Chair**

Department of Geology and Geophysics



**Paola Malanotte-Rizzoli**  
MIT Director of Joint Program



**James A. Yoder**  
WHOI Dean of Graduate Studies



The Dynamics of Oceanic Transform Faults:  
Constraints from Geophysical, Geochemical, and Geodynamical Modeling

by

Patricia Michelle Marie Gregg

B.S. Geology and Geophysics  
University of Missouri - Rolla, 2000

SUBMITTED TO THE MIT/WHOI JOINT PROGRAM IN PARTIAL  
FULFILLMENT OF THE REQUIREMENTS FOR THE DEGREE OF

DOCTOR OF PHILOSOPHY IN MARINE GEOPHYSICS  
AT THE  
MASSACHUSETTS INSTITUTE OF TECHNOLOGY  
AND THE  
WOODS HOLE OCEANOGRAPHIC INSTITUTION

JUNE 2008

© 2008 Patricia M. Gregg  
All Rights reserved

The author hereby grants to MIT and WHOI permission to reproduce  
and distribute publicly paper and electronic  
copies of this thesis document in whole or in part  
in any medium known or hereafter created.

Signature of Author: \_\_\_\_\_

*Patricia M. Gregg*

MIT/WHOI Joint Program in Oceanography  
May 16, 2008

Certified by: \_\_\_\_\_

*Jian Lin*

Jian Lin  
Senior Scientist, WHOI  
Thesis Supervisor

Accepted by: \_\_\_\_\_

*Bradford Hager*

Bradford H. Hager  
Professor of Geophysics, MIT  
Co-Chair, Joint Committee for Marine Geology and Geophysics

## CONTENTS

|  |           |
|--|-----------|
| <b>ABSTRACT .....</b>  | <b>7</b>  |
| <b>BIOGRAPHICAL SKETCH .....</b>   | <b>9</b>  |
| <b>ACKNOWLEDGEMENTS .....</b>  | <b>11</b> |
| FUNDING SOURCES.....   | 13        |
| <b>INTRODUCTION.....</b>   | <b>15</b> |
| FUTURE DIRECTIONS.....   | 17        |
| REFERENCES .....   | 21        |
| <b>CHAPTER 1: Segmentation of transform systems on the East Pacific Rise: Implications<br/>for earthquake processes at fast-slipping oceanic transform faults.....</b> | <b>25</b> |
| ABSTRACT .....   | 25        |
| INTRODUCTION .....   | 26        |
| TRANSFORM SEGMENTATION .....   | 29        |
| COULOMB STRESS CALCULATIONS .....  | 30        |
| EXAMPLES OF POSSIBLE STRESS INTERACTION.....   | 38        |
| CONCLUSIONS.....   | 39        |
| ACKNOWLEDGEMENTS .....   | 39        |
| REFERENCES CITED.....  | 40        |
| <b>CHAPTER 2: Spreading rate dependence of gravity anomalies along oceanic transform<br/>faults.....</b>   | <b>43</b> |
| ABSTRACT .....   | 43        |
| SUPPLEMENTARY INFORMATION.....   | 50        |
| <i>S1. Supplementary Figures.....</i>  | <i>50</i> |

|   |           |
|---|-----------|
| <i>S2. Supplementary Tables.....</i>  | <i>59</i> |
| <i>S3. Supplementary References .....</i>   | <i>60</i> |
| <b>CHAPTER 3: The effects of mantle rheology and fault segmentation on melt generation and extraction beneath oceanic transform faults.....</b> | <b>63</b> |
| ABSTRACT .....  | 63        |
| 1. INTRODUCTION.....  | 64        |
| 2. MODEL SETUP .....  | 67        |
| 2.1 Numerical Approach.....   | 67        |
| 2.2 Melt Generation and Extraction .....  | 70        |
| 2.2.1 Step 1: Fractional Melting.....   | 72        |
| 2.2.2 Step 2: Melt Migration .....  | 74        |
| 2.2.3 Step 3: Fractional Crystallization .....  | 76        |
| 3. NUMERICAL MODELING RESULTS .....   | 77        |
| 3.1 Benchmark: Comparison to EPR 9°N.....   | 77        |
| 3.2 3D Segmented transform fault results .....  | 83        |
| 4. APPLICATIONS TO THE SIQUEIROS TRANSFORM FAULT SYSTEM .....   | 86        |
| 4.1 Tectonic Setting.....   | 86        |
| 4.2 Crustal Thickness Predictions at Siqueiros .....  | 88        |
| 4.3 Geochemical Predictions at Siqueiros .....  | 90        |
| 5. DISCUSSION .....   | 93        |
| 5.1 Factors controlling crustal thickness variations .....  | 93        |
| 5.2 The Siqueiros Transform Effect on Mantle Melting .....  | 96        |
| 5.3 High-pressure Fractional Crystallization.....   | 97        |
| 5.4 Melt Extraction at Siqueiros Transform Fault.....   | 98        |
| 6. CONCLUSIONS .....  | 99        |
| 7. ACKNOWLEDGEMENTS .....   | 99        |
| 8. REFERENCES .....   | 100       |
| 9. TABLES.....  | 107       |

**APPENDIX: Seismicity characteristics of the equatorial East Pacific Rise and its offsets**  
..... **109**

ABSTRACT ..... 109

TABLES..... 110

FIGURES ..... 113





# The Dynamics of Oceanic Transform Faults: Constraints from Geophysical, Geochemical, and Geodynamical Modeling

by

Patricia Michelle Marie Gregg

Submitted to the MIT/WHOI Joint Program  
on May 16, 2008 in Partial Fulfillment of the  
Requirements for the Degree of Doctor of Philosophy in  
Marine Geophysics

## ABSTRACT

Segmentation and crustal accretion at oceanic transform fault systems are investigated through a combination of geophysical data analysis and geodynamical and geochemical modeling. Chapter 1 examines the effect of fault segmentation on the maximum predicted earthquake magnitude of an oceanic transform fault system. Results of thermal modeling suggest that fault segmentation by intra-transform spreading centers (ITSC) drastically reduces the available brittle area of a transform fault and thus limits the available earthquake rupture area. Coulomb stress models suggest that long ITSCs will prohibit static stress interaction between segments of a transform system and further limit the maximum possible magnitude of a given transform fault earthquake. In Chapter 2, gravity anomalies from a global set of oceanic transform fault systems are investigated. Surprisingly, negative residual mantle Bouguer gravity anomalies are found within fast-slipping transform fault domains. These gravity observations suggest a mass deficit within fast-slipping transform faults, which may result from porosity variations, mantle serpentinization, and/or crustal thickness variations. Two-dimensional forward modeling and the correlation of the negative gravity anomalies to bathymetric highs indicate crustal thickness excesses in these locations. Finally, in Chapter 3, mantle thermal and melting models for a visco-plastic rheology are developed to investigate the process of mantle melting and crustal accretion at ITSCs within segmented transform faults, and are applied to the Siqueiros transform fault system. Models in which melt migrates into the transform fault domain from a large region of the mantle best explain the gravity-derived crustal thickness variations observed at the Siqueiros transform. Furthermore, a mantle potential temperature of 1350°C and fractional crystallization at depths of 9 – 15.5 km best explain the major element composition variation observed at the Siqueiros transform.

**THESIS SUPERVISOR:**

Dr. Jian Lin, Senior Scientist, WHOI

**DEFENSE CHAIR:**

Dr. Henry J. B. Dick, Senior Scientist, WHOI

**THESIS COMMITTEE:**

Dr. Mark D. Behn, Assistant Scientist, WHOI

Professor Timothy L. Grove, MIT

Dr. Deborah K. Smith, Senior Scientist, WHOI

Professor Donald W. Forsyth, Brown University

## BIOGRAPHICAL SKETCH

Patricia M. Gregg

|                                |   |
|--------------------------------|---|
| <b>Education</b>               | Ph.D. Marine Geophysics<br>Massachusetts Institute of Technology / Woods Hole Oceanographic Institution<br>Joint Program, Thesis Supervisor: Dr. Jian Lin<br><br>B.S. Geology and Geophysics, University of Missouri-Rolla, 2000<br>Summa Cum Laude, Student Marshal, GPA 3.9/4.0   |
| <b>Honors &amp; Awards</b>     | 09/2003 - 08/2006: <b>NSF Graduate Research Fellow</b> (MIT/WHOI)<br>06/2002 - 08/2003: <b>Hollister Graduate Research Fellow</b> (MIT/WHOI)<br>08/1996 - 12/2000: <b>V.H. McNutt Geology Scholar</b> (UMR)<br>08/1997 - 12/2000: <b>Society of Exploration Geophysicists Scholar</b> (UMR)<br>08/1996 - 05/2000: <b>Missouri Bright Flight Scholar</b> (UMR)   |
| <b>Professional Experience</b> | 06/2001 - 06/2002: <b>Sprint</b> , Project Manager & Associate Engineer<br>Summer 2000: <b>Sandia National Laboratories</b> , Summer Intern<br>Summer 1999: <b>Woods Hole Oceanographic Institution</b> , Summer Fellow<br>08/1999 - 5/2000: <b>University of Missouri-Rolla</b> , Opportunities for Undergraduate Research Experience (OURE) Fellow<br>1/1998 - 5/2000: <b>KMNR FM Campus Radio Station</b> , Music Director<br>Summer 1995: <b>University of Missouri-Rolla</b> , Jackling Student Fellow   |
| <b>Field Experience</b>        | 2008: Chief Scientist, R/V New Horizon, Costa Rica Seismic Experiment<br>2004-2007: WHOI Geodynamics – Hawaii ('04), Iceland ('06), and Maine ('07)<br>2005: Ridge 2000 Cyprus Ophiolite Field School<br>2002: Shipboard Scientific Party, R/V Melville, Vancouver I, East Pacific Rise<br>2001: Shipboard Scientific Party, R/V Atlantis, AT4-4, NOAA/PMEL Hydrophone recovery and deployment, Mid-Atlantic Ridge<br>1996-2000: Participated in several geophysical data collection projects with the UMR Geophysics Group (GPR, EM, Seismic, and Resistivity)<br>1998: Boston University Summer Field Camp, Western Ireland   |
| <b>Invited Talks</b>           | Feb. 2008: Univ. of Hawaii SOEST, "Three-dimensional melt generation and extraction at fast-slipping oceanic transform faults"<br>Dec. 2007: Fall AGU, "The effect of fault segmentation on the dynamics of fast-slipping oceanic transform faults"<br>Sept. 2006: Oklahoma State University, "The spreading rate dependence of the gravity structure of oceanic transform faults"<br>April 2006: Brown University, "Fast-slipping transform faults: Gaining new understanding from gravity calculations at the East Pacific Rise"<br>Oct. 2005: WHOI Open House, "Understanding Oceanic Earthquakes"<br>Sept. 2004: UM - Rolla, "The Seismicity of Equatorial East Pacific Transform Faults" |



|                            |  |
|----------------------------|--|
| <b>Teaching Experience</b> | Spring 2007: Guest Lecturer, Boston College, GE530 Introduction to Marine Geology and Geophysics   |
| <b>Service</b>             | Session Co-Convener, Western Pacific Geophysical Meeting, Beijing, 2006<br>MIT Graduate Student Mentor, J. Elsenbeck (M.S. 2007) and E. Roland<br>Fall 2004: Taught two-day earth sciences and physics classes at Rolla Senior High School, MO<br>Reviewer for <i>Marine Geophysical Researches</i>  |
| <b>Publications</b>        | <p><b>P. M. Gregg, J. Lin, M. D. Behn, L. G. J. Montési</b>, Spreading rate dependence of the gravity structure of oceanic transform faults, <i>Nature</i>, 448, 183-187, 2007.</p> <p><b>P. M. Gregg, J. Lin, D. K. Smith</b>, Segmentation of transform systems on the East Pacific Rise: Implications for earthquake processes at fast-slipping oceanic transform faults, <i>Geology</i>, 34, 289-292, 2006.</p> <p>D. K. Smith, M. A. Tivey, <b>P. M. Gregg</b>, L. S. Kong, Magnetic anomalies at the Puna Ridge, a submarine extension of Kilauea Volcano: Implications for lava deposition, <i>Journal of Geophysical Research</i>, Vol. 106, No. B8, p. 16,047. 2001.</p>  |
| <b>Work in Progress</b>    | <b>P.M. Gregg, M. D. Behn, J. Lin, T. L. Grove</b> , The effects of mantle rheology and fault segmentation on melt generation and extraction beneath oceanic transform faults, <i>in prep for J. Geophys. Res.</i> , 2008.   |
| <b>Selected Abstracts</b>  | <p><b>P. M. Gregg, M. D. Behn, J. Lin, T. L. Grove, L. G. J. Montési</b>, The effect of fault segmentation on the dynamics of fast-slipping oceanic transform faults, Eos Trans. AGU, Fall Meet. Suppl., Abstract T22E-04, 2007, INVITED.</p> <p><b>P. M. Gregg, J. Lin, M. D. Behn, L. G. J. Montési</b>, Spreading rate dependence of the gravity structure of oceanic transform faults: Contrast between ultra-slow/slow and intermediate/fast slipping systems, Eos Trans. AGU, Fall Meet. Suppl. Abstract V23E-0698, 2006.</p> <p><b>P. M. Gregg, J. Lin, M. D. Behn, L. G. J. Montési</b>, Spreading rate dependence of the gravity structure of oceanic transform faults, WPGM Meet., T41B-05, 2006.</p> <p><b>P. M. Gregg, J. Lin, D. K. Smith</b>, Oceanic transform fault segmentation: constraints from hydroacoustic monitoring in the equatorial Pacific, Ridge 2000 Cyprus Field School, 2005.</p> <p><b>P. M. Gregg, J. Lin, D. K. Smith</b>, Characteristics and Possible Triggering Relationship of Earthquakes at the Pacific Transform Faults, Eos Trans. AGU, 85(47), Fall Meet. Suppl., Abstract T41A-1164, 2004.</p> <p><b>P. M. Gregg, D. K. Smith, L. S. Kong, K. Johnson, J. Reynolds, F. Trusdell, M. Tivey, W. Zhu, M. Bulmer, M. Avgerinos, D. Geist, T. Naumann, J. Mercer, T. Dulaney, E. Bergmanis</b>, Lava Depocenters at the Summit of the Submarine Puna Ridge, Kilauea Volcano, Fall AGU 2000.</p> <p>C. J. Weiss, <b>P. M. Gregg, G. A. Newman</b>, Electromagnetic Induction in a Fully 3D Heterogeneous Anisotropic Earth, Fall AGU 2000.</p> |

## ACKNOWLEDGEMENTS

*"It takes a village."*

Global Proverb, generally attributed to Africa

While this saying has become increasingly popular to describe the upbringing of a child, I believe that it is an equally accurate description of the efforts that go into raising a young scientist. I would not have reached this point in my career if it had not been for the valiant efforts of advisors, mentors, teachers, friends, and family. These are just some of the countless individuals who have helped me along the way.

First, many thanks to my advisor, Jian Lin - it has been an honor and a pleasure to be your graduate student. I am extremely grateful for your calm patience, tireless enthusiasm, encouragement, generosity, and constant advocacy. Your mentorship and advice have been critical for the development and execution of my thesis as well as my growth as a scientist. I am very grateful that you have encouraged me to become an independent thinker and to dig out areas of research that are of particular interest to me. Thank you for welcoming me into your home with wonderful meals (thanks also to Kelan!), introducing me to your colleagues and former students, and for the priceless experience of visiting China.

The project advisors who have worked with me during the past 6 years have been vital for helping me develop my research. I am very thankful for Debbie Smith who introduced me to the world of marine geophysics as a bright-eyed undergraduate Summer Student Fellow. Debbie's enthusiasm and love for science is contagious, and it is my interactions with her that inspired me to pursue a Ph.D. in marine geophysics. Having Mark Behn as a mentor during the final years of my graduate study has had a considerable influence on my scientific approach and the direction of my thesis. As my academic older brother, I have looked to him for guidance, encouragement, and an outstanding example of the scientist I am striving to become. I am extremely grateful for the time he has spent teaching and mentoring me as well as his generous loan of computing equipment. Tim Grove has been a constant, positive presence throughout my graduate matriculation. I got to know Tim through two of the most inspiring courses I have ever taken (Adv. Igneous Petrology and Thermodynamics), and it has been a pleasure to work with him to incorporate geochemistry into my thesis. Tim has been a tremendous resource and collaborator and the thought provoking conversations we have had over the years have manifested themselves in the final chapter of my thesis.

I am thankful to Don Forsyth who has provided insight and encouragement as a member of my thesis committee. I am very grateful for the hospitality of Henry Dick, not only in our many scientific discussions, but also for hosting dozens of meals and parties I have attended over my years at WHOI. Henry will forever be a fixture in my mind of how to bring a department together through excellent food and field trips. I am very honored to have Henry chair my thesis defense.



The scientific community of WHOI has played a significant role in my scientific growth over the past six years. I am constantly in awe at their generosity; they will take an hour out of their day to listen to a practice talk, and doors are always open when I have a question. Many thanks to Pablo Canales, my Clark South neighbor for 5 years, who has read drafts of proposals, listened to practice talks, and constantly encouraged me. Thanks also to Hans Schouten for delicious homemade meals, compelling scientific discussions, and for teaching me how not to give a bad seminar. Thanks to Dan Fornari, for his scientific generosity and sharing with me all he knows about the Siqueiros transform fault system (see Chapters 1-3 of this thesis). Many thanks to the WHOI geophysics group, including but not limited to – Laurent Montési, Dan Lizarralde, Adam Soule, Maurice Tivey, Chris German, Brian Tucholke, Jeff McGuire, and Ralph Stephen. Thanks to the WHOI geochemists who adopted me into their fold and gave me insight into the mantle - to Stan Hart for his kindness and advocacy, Nobu Shimizu for giving me “the other side of the story”, Zhenrong Wang for his help decoding KG92, Jurek Blusztajn, Alison Shaw, Mark Kurz, and Ken Sims. Thanks also to Jerry McManus for his encouragement and friendship.

Thank you to the continuous support of Pam Foster, Christina Cuellar, and the wonderful people in the Academic Programs Office - Marsha Gomes, Julia Westwater, Shona Vitelli, Valarie Caron and Christine Charette. Thanks also to Andrew and Peggy Daly and Rose for their friendship and kindness. I am grateful to BL Owens who, in the final weeks of my thesis, has rescued me from several computing mishaps and has become a new friend in the process.

I think it is fair to say that the MIT/WHOI Joint Program attracts some of the brightest students in the world. It has been a tremendous gift to learn from my fellow students and be persistently challenged by them. First to my classmates, Matt Jackson and Sharon Hoffmann, your friendship over these past years has been invaluable. A further thousand “thank you’s” to Sharon for day-to-day encouragement and her willingness to edit hundreds of pages of poorly written science for her fellow students. Abby Fusaro is unfailingly kind and generous. It is through tea and baked goods with this wonderful person that I survived my first year of graduate school. I am also indebted to her NH family who adopted Cory and me for several holidays and welcomed us into their home with open arms. Thanks to Hunter Oats and Vin Fusaro for their friendship and taking such good care of two of my favorite people. I am grateful for the friendships of Chris Waters, Casey Saenger, Andrea Burke, Mike Krawczynski, Andrea Llenos, Lynne Elkins, and Emily Roland who are a joy to have around; they constantly remind me of life outside of the walls of Clark. Jon Woodruff has been the ideal officemate in this push to the end; his tireless optimism has been greatly welcome. Last, and certainly not least, I owe a huge “thank you” to Rhea Workman for encouraging me to apply to the SSF at WHOI and being a friend and supporter for over a decade.

I have been truly blessed by an extended family of close friends who have known me since I was knee high to a grasshopper. I owe much of my continued sanity in life to their unwavering support. Sheri Redfearn has inspired me with her fearlessness and passion for life since we were 10 years old; she is in everyway my sister. Ted Miller has



kept me honest and true to myself with his tough love and unfailing loyalty. Bob Kumar keeps me in smiles and laughs and tries to be a positive influence on my health along the way – Please note that I can still school both Bob and Ted at basketball (can you say “treetop”?). Raj and Jess Kumar have been my twin pillars of support during trips to San Francisco for fall AGU. They always find time to take me to fantastic places to eat and give me a dose of unconditional love. Jeff Davis believed in me before I believed in myself. He has pushed me to be my best and not settle for less. Thank you to Micah Hackett for challenging me to think more deeply about my beliefs, his friendship has made me a better person. Thanks to Serena and Seth Bennett for their hospitality and friendship over the years and welcome respite at their home in Seattle. Finally, many thanks for the love and support of Franca Oboh-Ikuenobe and Rod and Nancy Lentz, my surrogate parents and friends.

My family has given me an unfaltering support system that has allowed me to grow and flourish with the knowledge that they are there when I need them. My father, Jay Gregg, introduced me to geology before I could walk. His passion and curiosity for the world around him has greatly influenced my approach to science and my passion for finding things out. I am thankful that he “dragged” me on field trips and encouraged my love of mathematics as well as art. My mother, Mickey, is the glue that holds our family together. Her insistence that her children be well-rounded as well as well-educated has had a profound impact on me. She fostered my love for swimming and running, and encouraged me to balance my study time with outside hobbies and activities. She instilled in me a healthy work ethic with an emphasis on doing my best while not trying to be perfect. My brother, Nick is by far one of the kindest, most likeable people I have ever met. I am incredibly glad that he is my brother and close friend. He, his wife, Erin, and sons, Mason, Aidan, and Eamon, have allowed me to escape into their real world of family and laughter, reminding me that life is not made up of equations and computers. This grounding has meant the world to me during the past six years. My youngest brother William keeps us all from taking things too seriously; this is a precious skill that I hope he will never lose. I have also been blessed by two adopted parents, and loving in-laws, PJ and Robin Pettijohn. I am thankful for their care packages, emails, and phone conversations. To those I have lost during these past years – my profound thanks to my grandmothers, Patricia and Ella Mae, for giving me marvelous examples of strong, independent women.

Finally, I offer my gratitude to my life partner and husband, Cory Pettijohn. I feel incredibly fortunate and blessed to have such a fervent supporter and kindred spirit in Cory, my best friend and lonely planet tour guide.

## **FUNDING SOURCES**

NATIONAL SCIENCE FOUNDATION GRADUATE RESEARCH FELLOWSHIP  
HOLLISTER GRADUATE RESEARCH FELLOWSHIP  
WHOI ACADEMIC PROGRAMS OFFICE – RESEARCH FELLOWSHIP





## INTRODUCTION

The global mid-ocean ridges are segmented by more than 120 transform fault systems. These transform fault systems are critical for accommodating the geometry of the ridge system as well as crustal accretion. The primary focus of this Ph.D. thesis is the investigation of oceanic transform faults using a multidisciplinary approach. Chapter 1 explores the seismicity of oceanic transform faults and examines the relationship between fault segmentation and earthquake rupture. Chapter 2 utilizes residual mantle Bouguer gravity anomaly (RMBA) calculations, 3D thermal models, and 2D forward models to investigate the structure of a global set of transform faults. Finally, in Chapter 3, I develop combined geodynamical and geochemical models to constrain melt generation and extraction at segmented transform fault systems. Below, I present a brief description of each of these studies and their primary conclusions.

In Chapter 1, I combine Coulomb static stress models with available geological and seismicity data to illustrate the importance of fault segmentation in models of earthquake interaction at oceanic transform faults. The 2D thermal models demonstrate that fault segmentation decreases the maximum magnitude of earthquakes by decreasing the brittle area thus limiting the fault rupture of the transform fault system [Gregg *et al.*, 2006]. Coulomb static stress models are used to explore whether adjacent fault segments behave independently of each other, and how their stress interaction depends on their offset distance. I find that, if intra-transform spreading centers are sufficiently long, adjacent transform fault segments will be decoupled and behave independently of each other. I also demonstrate the likelihood of stress interaction between strike-slip earthquakes and normal faults at nearby spreading centers. These findings are important for understanding the seismic budget of oceanic transform faults.

In Chapter 2, I analyze 3D gravity anomalies for 19 oceanic transform fault

systems globally. By evaluating transform faults from several mid-ocean ridge systems using 3D gravity inversions, 3D thermal models, and 2D forward models, I show that there is systematic variation in the gravity signature of oceanic transform faults as a function of their slip rate [Gregg *et al.*, 2007b]. The spreading-rate dependency of the gravity anomalies is especially evident at fast-slipping transform faults where I find more negative RMBA values in comparison to the adjacent ridge axes. All previous studies of slow-spreading mid-ocean ridges have shown more positive RMBA values within the transform fault domain instead, indicating crustal thinning at the end of ridge segments and focused crustal accretion at ridge segment centers [Kuo and Forsyth, 1988; Lin *et al.*, 1990]. Based on 2D forward models and available geological data, I propose that the negative RMBA values observed at fast-slipping transform faults indicate that fast-slipping systems have excess magma supply and increasing crustal production within the transform fault domain. These findings directly contradict the classic models of crustal accretion at mid-ocean ridges and require further investigation to determine the source of the negative RMBA at fast-slipping transform faults.

In the final chapter of my thesis, I look at the process of mantle melting and melt extraction at fast-slipping transform faults in an effort to explain the findings of increased crustal accretion at these systems [Gregg *et al.*, 2007b]. I combine thermal models of segmented ridge-transform-ridge systems with fractional melting [Kinzler and Grove, 1992b; a; 1993] and fractional crystallization models [Yang *et al.*, 1996]. The melt migration model of Sparks and Parmentier [1991] is used to investigate the source region of intra-transform spreading centers and examine two end-member melt aggregation models of wide vs. narrow melt pooling regions. I apply these models to the specific case of Siqueiros transform fault on the East Pacific Rise where there has been extensive geological and geophysical mapping [Fornari *et al.*, 1989; Carbotte and Macdonald, 1992; Gregg *et al.*, 2007b], as well as sampling via dredge and Alvin dives [Perfit *et al.*, 1996; Hays *et al.*, 2004]. Our findings suggest that in order to explain the estimated crustal



thicknesses indicated by the RMBA calculated at Siqueiros, melt must be pooled from large distances into the transform fault domain. Furthermore, we find that a mantle potential temperature of 1350C and fractional crystallization at depths of 9-15.5 km best fits the geochemical observations at the Siqueiros transform fault system [Perfit *et al.*, 1996; Hays, 2004]. These melt migration models provide us with first-order insights into the geological processes that may be occurring at the Siqueiros transform fault.

## **FUTURE DIRECTIONS**

The research contained in this thesis is a starting point for the development of many exciting projects for the coming years. In the future, I plan to extend my investigation to study several first-order geological processes.

Coulomb stress modeling is an invaluable tool for estimating static stress transfer following an earthquake or diking episode and determining likely locations for subsequent events [e.g., King *et al.*, 1994]. As part of this thesis, I successfully used stress models to illustrate earthquake interaction at oceanic transform faults and the stress interaction between strike-slip earthquakes and normal faults at nearby spreading centers [Gregg *et al.*, 2006]. It has also been suggested that stress transfer due to tectonic events can stimulate interactions between volcanoes and earthquakes. In particular, recent research on Hawaii has illustrated striking correlations between dike intrusions and earthquake occurrence at Mauna Loa [Walter and Amelung, 2004; 2006; Amelung *et al.*, 2007; McGovern, 2007]. These techniques can also be applied to understanding continental rifting; specifically, what is the stress interaction between dike injection during rifting change and subsequent faulting events? For example, temporal and spatial seismicity patterns along the East African Rift system indicate that there is ongoing stress interaction between adjacent rift segments via diking and faulting events [Aronovitz *et al.*, 2007]. Increasing our understanding of how earthquakes and volcanoes interact in settings



such as Hawaii and Africa is also important for aiding our ability to assess future hazards, which is a direction I plan to pursue.

The spreading rate dependence of mid-ocean ridge morphology is widely observed. Typical slow-spreading ridges are characterized by axial valleys and large topographic variations, whereas fast-spreading ridges are generally associated with axial highs and smoother topography [Macdonald, 1983]. However, in many locations it appears that magma supply may play an even greater role in controlling the ridge morphology than spreading rate. This paradox remains one of the first-order problems in understanding the dynamics of mid-ocean ridges. For example, the Cleft segment of the Juan de Fuca Ridge north of the 350 km-long Blanco transform fault has the morphology of a fast-spreading ridge and is thought to be magmatically robust, while the Gorda ridge to the south of Blanco, which is also spreading at a rate of 5.8 cm/yr, exhibits an axial valley typical of a slow-spreading ridge and is considered magmatically starved [Embley and Wilson, 1992; Hooft and Detrick, 1995]. Other examples include two adjacent segments at  $\sim 18^{\circ}\text{S}$  on the fast-spreading East Pacific Rise separated by a small non-transform discontinuity [Sinton *et al.*, 2002] and adjacent segments at  $\sim 114^{\circ}\text{E}$  along the intermediate spreading South East Indian Ridge (SEIR), which are separated by a 100 km-long transform fault [Cochran and Sempere, 1997; Buck *et al.*, 2005; Gregg *et al.*, 2007b]. Not only is the apparent decrease in magma budget visible in the morphology of these ridge segments, it is also observed in seismic and gravity data [Hooft and Detrick, 1995] as well as in the major and trace element geochemistry of lavas from these settings [Rubin and Sinton, 2007]. At present it is unclear why adjacent segments spreading at the same rate are in such stark contrast to each other, and our current understanding of the physics behind mid-ocean ridge spreading does not fully address this problem. Possible explanations may include thermal effects due to ridge offsets, regional tectonics, mantle flow variations, mantle buoyancy [Buck *et al.*, 2005], and mantle source heterogeneities. I plan to explore this research direction in the future.

In chapter 3 of this thesis I have developed techniques for coupling geodynamical and geochemical models, which can be constrained by geochemical and geophysical data to examine the driving forces governing the magma budget of a ridge segment and the resultant ridge morphology and geochemistry. These models can be further developed by accounting for the effect of fractional melting and crystallization on the trace element composition of extruded lavas at mid-ocean ridges. As part of my thesis work, we have made significant advancements in understanding geodynamical models by coupling them with fractional melting [Kinzler and Grove, 1992a, b; 1993] and fractional crystallization models [Yang *et al.*, 1996]. Incorporation of trace elements into these models will further strengthen their capabilities and provide another independent variable for comparison with geochemical observations, a direction that I am interested in exploring in collaboration with geochemist colleagues.

Hydrated oceanic lithosphere is an important component of the subduction zone system. It is widely accepted that water plays a fundamental role in the processes of mantle melting and, subsequently, arc volcanism in the subduction setting. However, very little is known about the actual water budget available from hydration of the oceanic lithosphere. Two popular models for oceanic lithosphere hydration include: 1) the serpentinization of the upper lithosphere at oceanic transform faults and fracture zones; and 2) hydration of the upper mantle to depths of 40 km at large-scale normal faults flanking the outer rise (thought to be the result of the bending of the slab as it subducts) [Hacker *et al.*, 2003]. However, it is unclear whether these two mechanisms are viable and if so, how much water is locked into hydrous phases within the down-going plate at these locations. This is another direction for future exploration.

During my thesis work, I have become increasingly interested in the effects of lithospheric hydration as a way to explain negative gravity anomalies found within fast-slipping oceanic transform faults [Gregg *et al.*, 2007b] as well as seismic moment deficits observed at many oceanic transform faults [Boettcher and Jordan, 2004]. In the past

couple of years we have developed several 3D thermal models for various transform fault geometries and mantle rheologies [Behn *et al.*, 2007; Gregg *et al.*, 2007a], as well as the inclusion of hydrous phase stability fields to assess localized hydration [Roland *et al.*, 2007]. A powerful result of these modeling efforts is the ability to estimate water budgets expected from oceanic transform faults of varying spreading rate and geometry. The next step in these calculations is to look at hydration in the inactive fracture zones and explore the dehydration of these sections of the oceanic lithosphere as they are incorporated at subduction zones at settings such as the Chile Triple Junction or the Blanco Fracture Zone.



## REFERENCES

- Amelung, F., S. H. Yun, T. R. Walter, P. Segall, and S. W. Kim (2007), Stress control of deep rift intrusion at Mauna Loa Volcano, Hawaii, *Science*, *316*, 1026-1030.
- Aronovitz, A. C., C. J. Ebinger, E. Campbell, D. B. Keir, A. Ayele, and G. Mitra (2007), Segment linkage in Afar via magma intrusion: The birth of a transform fault?, *Eos Trans. AGU*, *88*, Fall Meet. Suppl., T41A-0354.
- Behn, M. D., M. S. Boettcher, and G. Hirth (2007), Thermal structure of oceanic transform faults, *Geology*, *35*, 307-310.
- Boettcher, M. S., and T. H. Jordan (2004), Earthquake scaling relations for mid-ocean ridge transform faults, *109*, B12, doi:10.1029/2004JB003110.
- Buck, W. R., L. L. Lavier, and A. N. B. Poliakov (2005), Modes of faulting at mid-ocean ridges, *Nature*, *434*, 719-723.
- Carbotte, S., and K. Macdonald (1992), East Pacific Rise 8°-10° 30'N - Evolution of ridge segments and discontinuities from Seamarc II and 3-dimensional magnetic studies, *J. Geophys. Res.*, *97*, 6959-6982.
- Cochran, J. R., and J. C. Sempere (1997), The Southeast Indian Ridge between 88°E and 118°E: Gravity anomalies and crustal accretion at intermediate spreading rates, *J. Geophys. Res.*, *102*, 15463-15487.
- Embley, R. W., and D. S. Wilson (1992), Morphology of the Blanco transform-fault zone-NE Pacific - Implications for its tectonic evolution, *Mar. Geophys. Res.*, *14*, 25-44.
- Fornari, D. J., D. G. Gallo, M. H. Edwards, J. A. Madsen, M. R. Perfit, and A. N. Shor (1989), Structure and topography of the Siqueiros transform-fault system - Evidence for the development of intra-transform spreading centers, *Mar. Geophys. Res.*, *11*, 263-299.
- Gregg, P. M., J. Lin, and D. K. Smith (2006), Segmentation of transform systems on the East Pacific Rise: Implications for earthquake processes at fast-slipping oceanic



- transform faults, *Geology*, 34, 289-292.
- Gregg, P. M., M. D. Behn, J. Lin, and T. L. Grove (2007a), The effect of fault segmentation on the dynamics of fast-slipping oceanic transform faults, *Eos. Trans. AGU*, 88, Fall Meet. Suppl., Abstract T22E-04.
- Gregg, P. M., J. Lin, M. D. Behn, and L. G. J. Montesi (2007b), Spreading rate dependence of gravity anomalies along oceanic transform faults, *Nature*, 448, 183-185.
- Hacker, B. R., G. A. Abers, and S. M. Peacock (2003), Subduction factory - 1. Theoretical mineralogy, densities, seismic wave speeds, and H<sub>2</sub>O contents, *J. Geophys. Res.*, 108, doi:10.1029/2001JB001127.
- Hays, M. R. (2004), Intra-transform volcanism along the Siqueiros Fracture Zone 8°20' n - 8°30'N, East Pacific Rise, 251 pp, University of Florida, Gainesville.
- Hays, M. R., M. R. Perfit, D. J. Fornari, and W. Ridley (2004), Magmatism in the Siqueiros Transform: Major and trace element evidence for mixing and multiple sources, 85, Fall Meet. Suppl., Abstract T41A-1165.
- Hooft, E. E. E., and R. S. Detrick (1995), Relationship between axial morphology, crustal thickness, and mantle temperature along the Juan de Fuca and Gorda ridges, *J. Geophys. Res.*, 100, 22499-22508.
- King, G. C. P., R. S. Stein, and J. Lin (1994), Static stress changes and the triggering of earthquakes, *Bull. Seismol. Soc. Amer.*, 84, 935-953.
- Kinzler, R. J., and T. L. Grove (1992a), Primary magmas of midocean ridge basalts 2. Applications, *J. Geophys. Res.*, 97, 6907-6926.
- Kinzler, R. J., and T. L. Grove (1992b), Primary magmas of midocean ridge basalts 1. Experiments and methods, *J. Geophys. Res.*, 97, 6885-6906.
- Kinzler, R. J., and T. L. Grove (1993), Corrections and further discussion of the primary magmas of midocean ridge basalts, 1 and 2, *J. Geophys. Res.*, 98, 22339-22347.
- Kuo, B. Y., and D. W. Forsyth (1988), Gravity anomalies of the ridge transform intersection system in the south Atlantic between 31° and 34.5°S: Upwelling centers

- and variations in crustal thickness, *Mar. Geophys. Res.*, *10*, 205-232.
- Lin, J., G. M. Purdy, H. Schouten, J.-C. Sempere, and C. Zervas (1990), Evidence from gravity data for focused magmatic accretion along the Mid-Atlantic Ridge, *Nature*, *344*, 627-632.
- Macdonald, K. C. (1983), A geophysical comparison between fast and slow spreading centers: Constraints on magma chamber formation and hydrothermal activity, in *Hydrothermal processes at seafloor spreading centers*, edited by P. A. Rona, et al., pp. 27-51, Plenum, New York.
- McGovern, P. J. (2007), Flexural stresses beneath Hawaii: Implications for the October 15, 2006 earthquakes and magma ascent, *Submitted to Geophys. Res. Lett.*
- Perfit, M. R., D. J. Fornari, W. I. Ridley, P. D. Kirk, J. Casey, K. A. Kastens, J. R. Reynolds, M. Edwards, D. Desonie, R. Shuster, and S. Paradis (1996), Recent volcanism in the Siqueiros transform fault: Picritic basalts and implications for MORB magma genesis, *Earth Planet. Sci. Lett.*, *141*, 91-108.
- Roland, E. C., M. D. Behn, and G. Hirth (2007), Thermal-mechanical behavior of oceanic transform faults - Implications for hydration of the upper oceanic mantle, *Eos Trans. AGU*, *88*, Fall Meet. Suppl., Abstract T32B-06.
- Rubin, K. H., and J. M. Sinton (2007), Inferences on mid-ocean ridge thermal and magmatic structure from MORB compositions, *Earth Planet. Sci. Lett.*, *260*, 257-276.
- Sinton, J., E. Bergmanis, K. Rubin, R. Batiza, T. K. P. Gregg, K. Gronvold, K. C. Macdonald, and S. M. White (2002), Volcanic eruptions on mid-ocean ridges: New evidence from the superfast spreading East Pacific Rise, 17°-19°S, *J. Geophys. Res.*, *107*.
- Sparks, D. W., and E. M. Parmentier (1991), Melt extraction from the mantle beneath spreading centers, *Earth and Planet. Sci. Lett.*, *105*, 368-377.
- Walter, T. R., and F. Amelung (2004), Influence of volcanic activity at Mauna Loa, Hawaii, on earthquake occurrence in the Kaoiki seismic zone, *Geophys. Res. Lett.*, *31*,

L07622, doi:10.1029/2003GL019131.

Walter, T. R., and F. Amelung (2006), Volcano-earthquake interaction at Mauna Loa Volcano, Hawaii, *J. Geophys. Res.*, *111*, B05204, doi:10.1029/2005JB003861.

Yang, H. J., R. J. Kinzler, and T. L. Grove (1996), Experiments and models of anhydrous, basaltic olivine-plagioclase-augite saturated melts from 0.001 to 10 kbar, *Contrib. Mineral. Petrol.*, *124*, 1-18.

## **CHAPTER 1: Segmentation of transform systems on the East Pacific Rise: Implications for earthquake processes at fast-slipping oceanic transform faults**

### **ABSTRACT**

Seven of the eight transform systems along the equatorial East Pacific Rise from 12°N to 15°S have undergone extension due to reorientation of plate motions and have been segmented into two or more strike-slip fault strands offset by intratransform spreading centers (ITSCs). Earthquakes recorded along these transform systems both teleseismically and hydroacoustically suggest that segmentation geometry plays an important role in how slip is accommodated at oceanic transforms. Results of thermal calculations suggest that the thickness of the brittle layer of a segmented transform fault could be significantly reduced by the thermal effect of ITSCs. Consequently, the potential rupture area, and thus maximum seismic moment, is decreased. Using Coulomb static stress models, we illustrate that long ITSCs will prohibit static stress interaction between transform segments and limit the maximum possible magnitude of earthquakes on a given transform system. Furthermore, transform earthquakes may have the potential to trigger seismicity on normal faults flanking ITSCs.

---

Published as P. M. Gregg, J. Lin, and D. K. Smith, Segmentation of transform systems on the East Pacific Rise: Implications for earthquake processes at fast-slipping oceanic transform faults. *Geology*, v. 34, no. 4, p. 289-292, 2006.



## INTRODUCTION

Segmented transform systems are composed of several fault strands offset by short ridges or rifts referred to as intra-transform spreading centers (ITSCs) (Menard and Atwater, 1969; Searle, 1983; Pockalny et al., 1997), where active seafloor spreading and crustal accretion are occurring (Fornari et al., 1989; Hekinian et al., 1992; Perfit et al., 1996). Along the equatorial East Pacific Rise between 15°S and 12°N (Fig. 1), the Siqueiros, Quebrada, Discovery, Gofar, Yaquina, Wilkes, and Garrett transform systems have all undergone transtension due to changes in plate motions, and each of these transforms is segmented by at least one ITSC (Searle, 1983; Fornari et al., 1989; Lonsdale, 1989; Goff et al., 1993; Pockalny et al., 1997). The Clipperton transform system has undergone several periods of transpression (Pockalny, 1997), and is the only unsegmented transform system along the equatorial East Pacific Rise.

The global deficiency of seismic moment release on oceanic transform systems has led researchers to hypothesize that a significant portion of oceanic transform slip is accommodated aseismically (e.g., Boettcher and Jordan, 2004). However, global seismicity studies have yet to consider the prevalence of transform fault segmentation. Dziak et al. (1991) observed that earthquake sizes generally correlate with the lengths of individual fault segments at the Blanco transform fault. Our observations of earthquakes recorded on East Pacific Rise transform faults indicate that segmentation is an important factor influencing rupture of large earthquakes at oceanic transforms. While it has been shown that segmentation and fault steps play an important role in controlling the earthquake behavior of continental strike-slip faults (e.g., Harris and Day, 1993), the influence of segmentation and ITSCs on earthquake processes at an oceanic transform system has not been studied in detail.

In this paper, we use teleseismically and hydroacoustically recorded seismicity data from the equatorial East Pacific Rise and Coulomb static stress models to explore the effect of ITSCs on static stress interaction between transform fault segments. We

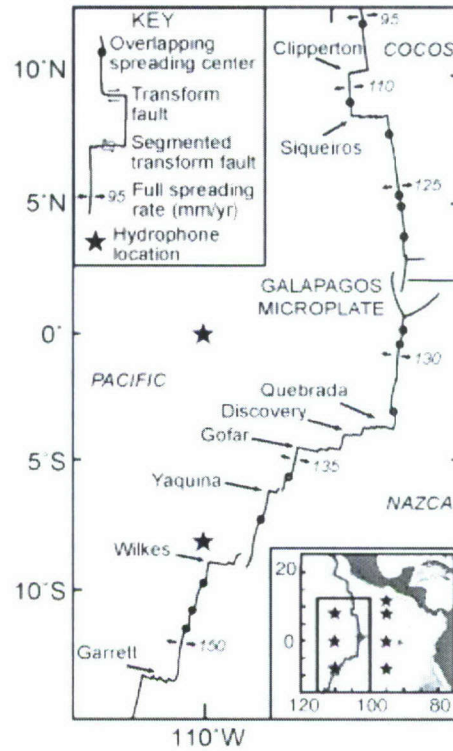


**Figure 1.** Regional map of the equatorial EPR showing large transform and non-transform offsets. Segmentation geometry is included based on previous geological mapping of the transform systems (e.g., Fornari et al., 1989; Lonsdale, 1989). Inset: Regional map showing location of the full array of NOAA Pacific Marine Environmental Laboratory hydrophones.

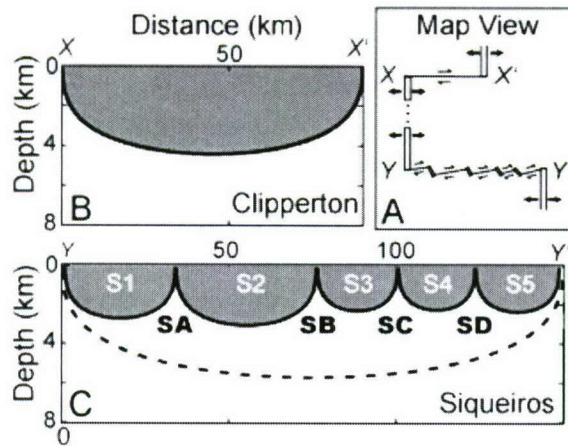


**Figure 2.** Comparison of estimated areas of brittle lithosphere using a one-dimensional, steady-state lithosphere cooling model (McKenzie, 1969) for the Clipperton (B) and Siqueiros (C) transforms. A: The 90 km Clipperton transform system (X–X') and the 150 km Siqueiros transform system (Y–Y'), which is broken into five major segments S1, S2, S3, S4, and S5 separated by four ITSCs SA, SB, SC, and SD (Fornari et al., 1989). B: Calculated area of brittle lithosphere for temperatures  $<600^{\circ}\text{C}$  (shaded region) for the Clipperton transform. C: Comparison of the calculated areas of brittle lithosphere for the Siqueiros transform for a model of unsegmented geometry (area above the dotted line) versus a model consisting of five individual segments offset by steady-state ITSCs (shaded area).



investigate whether adjacent fault segments can behave independently of one another, and how the interaction between segments depends on their offset distance.

### TRANSFORM SEGMENTATION

Segmentation of the transtensional transform systems at the equatorial East Pacific Rise has resulted in individual strike-slip fault strands with lengths of 18–89 km, with an average of ~37 km. The ITSCs separating the fault strands have lengths of 5–20 km, with an average length of ~11 km. Fresh lavas collected from the ITSCs within the Siqueiros and Garrett transforms (Hekinian et al., 1992; Perfit et al., 1996) indicate that ITSCs are magmatically active, implying that the regions beneath them are hotter, and thus the lithospheric plate is thinner than the surrounding domains. To explore the effect of segmentation on the transform fault thermal structure, we use a half-space steady-state lithospheric cooling model (McKenzie, 1969; Abercrombie and Ekstrom, 2001). The temperature within the crust and mantle,  $T$ , is defined as  $T = T_m \text{erf}[y(2\kappa t)^{-1/2}]$ , where  $T_m$  is the mantle temperature at depth, assumed to be 1300°C;  $y$  is the depth;  $\kappa$  is the thermal diffusivity, assumed to be 1,026 m<sup>2</sup>s<sup>-1</sup>; and  $t$  is the age of the lithosphere obtained by dividing distance from the ridge axis by half the spreading rate.

Figure 2 compares the calculated areas of brittle deformation, defined as regions with calculated temperatures  $\leq 600^\circ\text{C}$ , for the geometries of the Clipperton and Siqueiros transform systems. The calculated area under the 600 °C isotherm for the Clipperton transform fault is 326 km<sup>2</sup>, compared to 710 km<sup>2</sup> for a model of a single unsegmented fault with the cumulative length of the Siqueiros transform system. When the actual segmentation geometry of the Siqueiros transform system is considered, however, the integrated area of the calculated brittle deformation region is decreased by ~60% to 277 km<sup>2</sup>.

Seismic moment ( $M_0$ ), which reflects the energy released by an earthquake, is a function of the rupture area of the fault. Specifically,  $M_0 = G \times D \times S$ , where  $G$  is the shear modulus, estimated to be 27 GPa from seismic velocities (Canales et al., 2003),  $D$  is the average slip, and  $S$  is the estimated brittle area. The resulting moment magnitude is

$M_w = (2/3) \times \log(M_0) - 10.73$ . For a model of constant stress drop during pure strike-slip earthquakes,  $M_0 = (\pi/2) \times \Delta\sigma \times w \times S$ , where  $\Delta\sigma$  is the earthquake stress drop, and  $w$  is the fault width, estimated from  $S$  divided by fault length (Stein and Wysession, 2003).

Curves in Figure 3 show the predicted earthquake magnitudes for a given fault area, assuming models of constant fault slip (Fig. 3A) or constant stress drop (Fig. 3B) during earthquakes. Earthquakes recorded teleseismically as listed in the Harvard Centroid-Moment Tensor (CMT) catalog were relocated to a specific transform segment using hydroacoustically recorded earthquakes, which have smaller location errors ( $<6$  km) (Fox et al., 2001). The maximum earthquake magnitudes observed on each of the transform fault segments at the equatorial East Pacific Rise from 1996 to 2001 are plotted in Figure 3. Assuming the complete rupture of a given individual fault segment, we can estimate the amount of slip or the stress drop for a given earthquake. For example, the largest earthquake observed on the Clipperton transform has a  $M_w$  of 6.6 (Fig. 3). If the entire brittle area of Clipperton ( $326 \text{ km}^2$ ) was ruptured during this earthquake, the estimated average slip is 1 m, or the estimated average stress drop is 53 bar or 5.3 MPa.

### COULOMB STRESS CALCULATIONS

Evidence for potential earthquake interactions along oceanic transform faults has been noted in several investigations (e.g., Toda and Stein, 2000; Bohnenstiehl et al., 2002, 2004; McGuire et al., 2002; Forsyth et al., 2003). We utilize the methods of King et al. (1994) and Toda et al. (1998) to calculate how static stress from a moderate-sized earthquake is transferred to adjacent faults, and assess the likelihood of rupturing multiple transform segments during a single earthquake. According to Coulomb failure criteria, when an earthquake occurs on a source fault, changes in Coulomb failure stress ( $\Delta\sigma_f$ ) on a receiver fault are expressed as  $\Delta\sigma_f = \Delta\tau_s + \mu' \times \Delta\sigma_n$ , where  $\Delta\tau_s$  and  $\Delta\sigma_n$  are changes in shear and normal stresses, on the receiver fault, and  $\mu'$  is the apparent friction coefficient adjusted for the pore pressure effect (King et al., 1994).

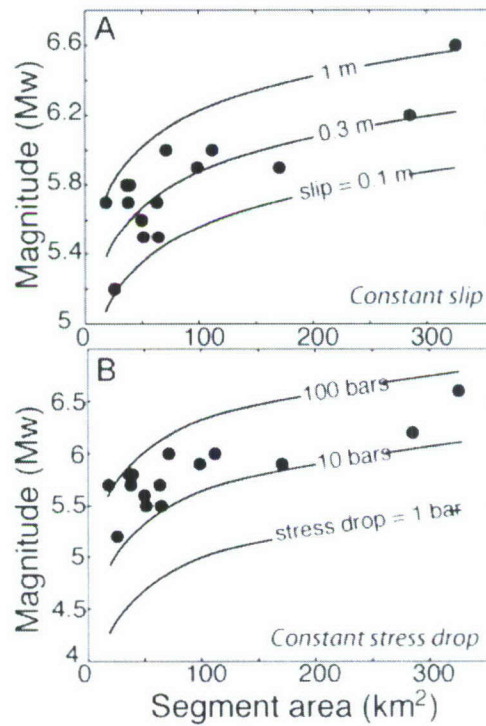


**Figure 3.** A: The predicted maximum moment magnitude,  $M_w$ , of earthquakes (curved lines) for a given transform segment area and a constant slip of 0.1, 0.3, and 1.0 m. The calculations assume that the earthquake ruptures the entire transform segment. Black dots mark the observed maximum  $M_w$  recorded on the transform segments of the equatorial East Pacific Rise. The rightmost data point,  $M_w = 6.6$ , corresponds to the Clipperton transform. B: The predicted maximum  $M_w$  assuming a constant stress drop of transform earthquakes of 1, 10, and 100 bar.



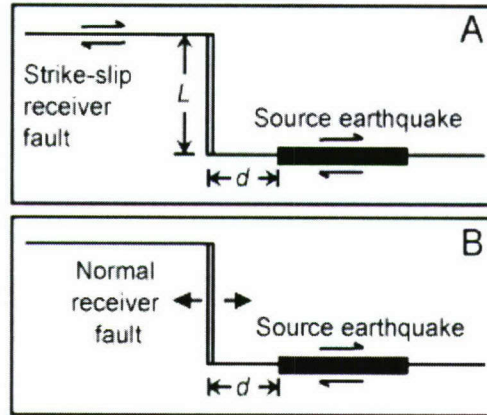


**Figure 4.** Schematic models showing the geometry of two transform segments bisected by a single ITSC of variable length,  $L$ . The source earthquake is located on the bottom right transform segment with its left edge located at a distance,  $d$ , from the ITSC-transform intersection. The source earthquake is assumed to be a strike-slip event on a vertical plane parallel to the transform segment. A: A scenario in which the receiver fault is a strike-slip fault located on the top left transform segment, which is assumed to have the same dip, strike, and rake as the source earthquake. B: A scenario in which the receiver fault is a normal fault located along the ITSC, which is assumed to have a dip of  $60^\circ$  and is parallel to the ITSC.

We consider a simple geometry in which two adjacent transform segments are offset by an ITSC of variable length,  $L$ , for two scenarios assuming the receiver faults are either strike-slip events along the adjacent transform segment (Fig. 4A) or normal-faulting events located along the ITSC (Fig. 4B). The rupture size for the source earthquake in both cases is varied to reflect typical earthquake magnitudes observed along the segmented transforms of the equatorial East Pacific Rise.

For the first scenario, the calculated maximum change in static stress,  $||\Delta\sigma_f||$ , transferred to the receiver fault is plotted versus  $L$  for  $M_w = 5.0, 5.5$ , and  $6.0$  (Fig. 5). As the separation distance between the two transform segments increases, the predicted maximum induced Coulomb stress change on the receiver fault decreases. For example, if  $M_w = 6.0$ ,  $d = 0$  km, and  $L$  is increased from 5 to 15 km, the calculated  $||\Delta\sigma_f||$  decreases from 1.35 bar to 0.25 bar (Fig. 5A). The proximity of the earthquake to the ITSC-transform intersection (ITI) is also very important: the closer the source earthquake is located to the ITI (i.e., smaller  $d$ ), the greater the predicted maximum Coulomb stress change on the receiver fault (Fig. 5). For example, if  $M_w = 6.0$ ,  $L = 5$  km, and  $d$  is increased from 0 to 10 km, the calculated  $||\Delta\sigma_f||$  decreases from 2.5 bars to 0.1 bars. Previous studies have shown statistically significant correlations between regions of seismicity rate changes following continental strike-slip earthquakes and areas of calculated stress changes  $> 0.2$ -1.0 bars (Toda et al., 1998).

In the second scenario (Fig. 6), for  $M_w \geq 5.0$ , a source earthquake with relatively small  $d$  is calculated to cause significant Coulomb static stress increases on ITSC parallel secondary normal faults. Such Coulomb stress changes correspond to a decrease in normal confining pressure across the ITSC axis, which may result in triggering of normal faulting earthquakes or magmatic diking events along the ITSCs. The predicted Coulomb stress changes on secondary normal faults along the ITSC are a strong function of the location of the source earthquake. For example, if  $M_w = 6.0$  and  $d$  is increased from 5 to 10 km, the calculated  $||\Delta\sigma_f||$  decreases from 2.5 bars to 0.5 bar.

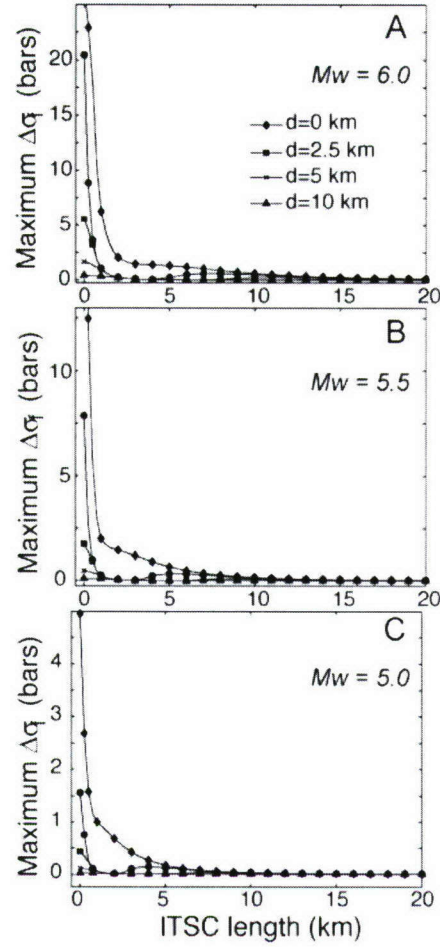


**Figure 5.** Calculated maximum Coulomb stress changes on a secondary strike-slip receiver fault caused by a strike-slip source earthquake (geometry shown in Fig. 4A) for source earthquake  $M_w$  5 6.0, 5.5, and 5.0. Note that the vertical scale is different for each panel. All stress calculations were carried out using a three-dimensional boundary-element model, Coulomb 2.6 (Toda et al., 1998), assuming that both the source and receiver faults extend to a depth of 5 km. For each Coulomb calculation, we used a Young's modulus of 62.5 GPa, a Poisson's ratio of 0.25, an apparent friction coefficient,  $\mu_0$ , of 0.4 (e.g., King et al., 1994), and a tapered slip distribution. Stresses are sampled on a horizontal plane at a depth of 2 km. The maximum change in Coulomb stress is taken directly from the point on the receiver fault where Coulomb stress reaches a maximum value. Calculations were carried out for  $L$  5 1 to 20 km and  $d$  5 0, 2.5, 5, and 10 km. ITSC.



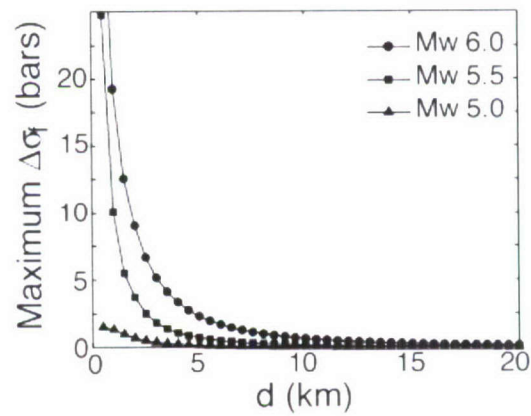


**Figure 6.** Calculated maximum Coulomb stress changes on a secondary normal receiver fault along the ITSC caused by a strike-slip source earthquake on the adjacent transform segment with geometry shown in Figure 4B. The maximum change in Coulomb stress is taken from the point on the ITSC where Coulomb stress reaches a maximum value. The results shown are for calculations assuming a tapered slip distribution along the source earthquake.

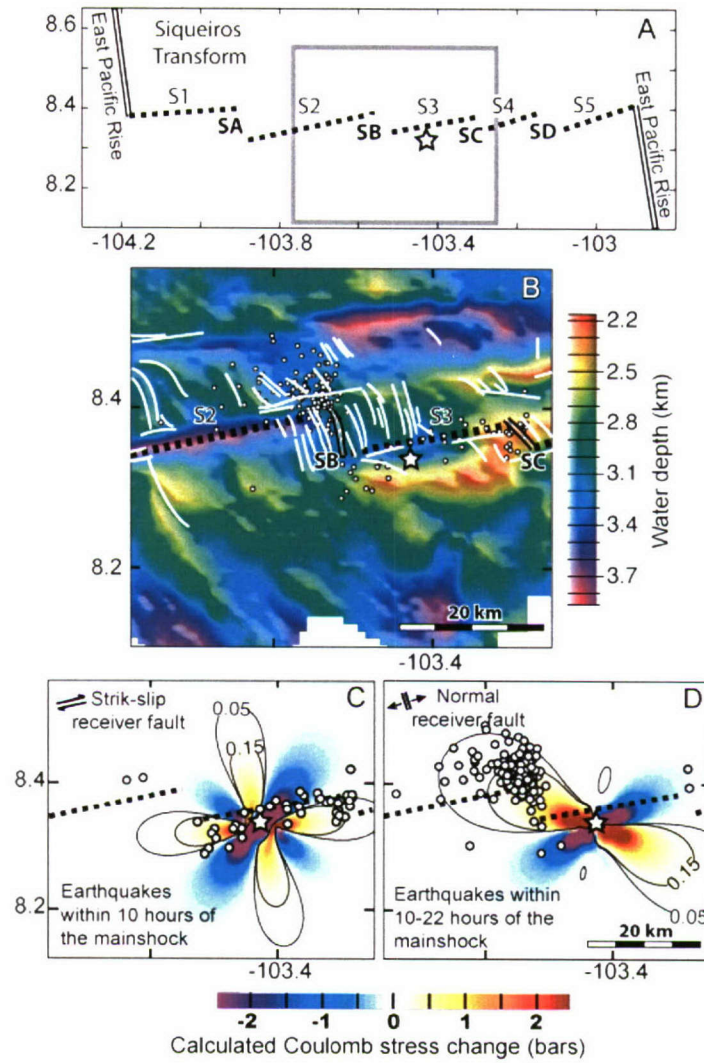


**Figure 7.** Coulomb stress models for a teleseismically recorded earthquake ( $M_w = 5.7$ , 26 April 2001) on the Siqueiros transform system. Earthquake location is shown by white star on each panel. A: Location map shows the segmentation geometry of Siqueiros. Outlined region indicates area investigated in B, C, and D. B: Bathymetric map overlain by the geologic interpretations (thin white lines) of Fornari et al. (1989). White circles indicate the locations of the 170 aftershocks. C: Calculated Coulomb static stress changes on secondary strike-slip receiver faults with the same dip, strike, and rake as the source earthquake. Source fault parameters from Harvard CMT focal mechanism: strike =  $263^\circ$ , dip =  $81^\circ$ , and scalar moment =  $4.49 \times 10^{24}$  dyne-cm. We assume rupture length = 5 km, width = 5 km and slip = 0.36 m. We used a tapered slip distribution and stresses were sampled on a horizontal plane at a depth of 2 km. Fox et al. (2001) estimates a lower threshold for earthquakes recorded within the hydrophone array of  $M_b = 1.0$ -1.8. The first 45 aftershocks (shown as white circles) occurred within 10 hours of the mainshock and fall along fault segment S3. The 0.15 bar and 0.05 bar contours are shown as solid black lines. We observe that  $\sim 31\%$  of the first 45 aftershocks occurred in regions with stress increases  $\geq 0.15$  bars, and  $\sim 56\%$  in areas with stress increases  $\geq 0.05$  bars. D: Calculated Coulomb static stress changes on secondary normal faults dipping  $60^\circ$  and parallel to the ITSC SB. The later 125 aftershocks (shown as white circles) correspond well with predictions of increased normal stress thus suggesting that they might be associated with normal receiver faults. We observe that  $\sim 63\%$  of the latter 125 aftershocks occurred in regions with stress increases  $\geq 0.15$  bars, and  $\sim 90\%$  occurred in areas with stress increases  $\geq 0.05$  bars.



## EXAMPLES OF POSSIBLE STRESS INTERACTION

Hydroacoustic monitoring of the EPR (Fox et al., 2001) has allowed us to investigate several moderate sized earthquakes to determine the role of transform segmentation in earthquake processes. Here, we have chosen one  $M_w = 5.7$  teleseismically recorded earthquake that occurred in April 2001 along the S3 segment of the Siqueiros transform fault, which appears to have triggered seismicity on the S2 segment as well as on the ITSC SB (Fig. 7). Coulomb stress models were calculated using the source earthquake focal mechanism recorded in the Harvard CMT catalog, and the earthquake source location was taken from the hydroacoustic earthquake catalog.

The mainshock ruptured the 24-km long S3 fault segment ~10 km from its intersection with the 8 km-long ITSC SB. Approximately 170 aftershocks were recorded hydroacoustically within 24 hr and 50 km of the epicenter of the mainshock. The first 45 aftershocks (Fig. 7C) occurred along the fault segment S3 within 10 hr of the mainshock, and were spatially truncated by the ITSCs SB and SC. These aftershock locations correspond well with areas of predicted static stress increase along the source fault and on secondary strike-slip receiver faults along segment S3. Furthermore, the termination of the aftershocks east of the source fault at ITSC SC agrees with predicted estimates for segment interaction.

The subsequent 125 aftershocks (Fig. 7D) occurred on ITSC SB and the eastern end of the adjacent fault segment S2. The static stress models assuming transform-parallel strike-slip receiver faults do not predict this pattern of seismicity (Fig. 7C). Geologic interpretations of Siqueiros transform by Fornari et al. (1989) indicate several ITSC-parallel faults flanking ITSC SB to the east, west, and north (Fig. 7B). As the latter 125 aftershock locations correspond well with areas of increased Coulomb stress for normal receiver faults, we hypothesize that these aftershocks might be associated with triggered seismicity on the normal faults mapped by Fornari et al. (1989). The ITSC parallel tectonic fabric was created by ITSCs SA and SB, which appear to have slow-spreading ridge morphology (Fornari et al., 1989); this may account for the development of seismically active normal faults. Another possibility is that these aftershocks may reflect

a diking event near ITSC SB resulting from mainshock-triggered decreases in confining pressure. Dynamic stress changes might also trigger aftershocks, but are difficult to evaluate due to the lack of detailed mainshock rupture models.

## CONCLUSIONS

Detailed analysis of earthquakes on transform systems at the EPR suggests that segmentation geometry plays an important role in how slip is accommodated at fast-slipping oceanic transforms. Results of Coulomb stress models suggest that the length of the ITSC that offsets two transform fault strands will determine whether the adjacent fault segments will interact by static stress transfer. If the ITSC is sufficiently long, the adjacent segments will be decoupled and behave independently of each other. This is particularly important in studies of earthquakes at oceanic transforms since a long oceanic transform system, could be composed of several decoupled fault segments. Moreover, we illustrate that the thermal effect of ITSCs may reduce the thickness of the brittle layer, thus decreasing the potential rupture area and the maximum seismic moment of an oceanic transform fault system. Finally, we suggest that transform earthquakes may have the potential to trigger seismicity on secondary normal faults flanking ITSCs.

## ACKNOWLEDGEMENTS

This work was supported by a NSF Graduate Research Fellowship (P. M. Gregg), NSF Grant OCE-0221386 (D. K. Smith and J. Lin), and the WHOI Deep Ocean Exploration Institute (J. Lin). We are grateful for helpful discussions with C. Williams, M. Behn, M. Boettcher, J. Cann, D. Fornari, D. Forsyth, J. McGuire, H. Schouten, and the WHOI geophysics group, and to D. Bohnenstiehl, E.A. Okal, and S. Toda for constructive and insightful reviews.



## REFERENCES CITED

- Abercrombie, R.E., and Ekstrom, G., 2001, Earthquake slip on oceanic transform faults: *Nature*, v. 410, p. 74-77.
- Boettcher, M.S., and Jordan, T.H., 2004, Earthquake scaling relations for mid-ocean ridge transform faults: *Journal of Geophysical Research-Solid Earth*, v. 109, B12, doi:10.1029/2004JB003110.
- Bohnenstiehl, D.R., Tolstoy, M., and Chapp, E., 2004, Breaking into the plate: A 7.6 Mw fracture-zone earthquake adjacent to the Central Indian Ridge: *Geophysical Research Letters*, v. 31, B2, doi:10.1029/2003GL018981.
- Bohnenstiehl, D.R., Tolstoy, M., Dziak, R.P., Fox, C.G., and Smith, D.K., 2002, Aftershock sequences in the mid-ocean ridge environment: an analysis using hydroacoustic data: *Tectonophysics*, v. 354, p. 49-70.
- Canales, J.P., Detrick, R., Toomey, D.R., and Wilcock, S.D., 2003, Segment-scale variations in the crustal structure of 150-300 kyr old fast spreading oceanic crust (East Pacific Rise, 8°15'N-10°5'N) from wide-angle seismic refraction profiles: *Geophysical Journal International*, v. 152, p. 766-794.
- Dziak, R.P., Fox, C.G., and Embley, R.W., 1991, Relationship between seismicity and geologic structure of the Blanco Transform Zone: *Marine Geophysical Researches*, v. 13, p. 203-208.
- Fornari, D.J., Gallo, D.G., Edwards, M.H., Madsen, J.A., Perfit, M.R., and Shor, A.N., 1989, Structure and topography of the Siqueiros transform-fault system - Evidence for the development of intra-transform spreading centers: *Marine Geophysical Researches*, v. 11, p. 263-299.
- Forsyth, D.W., Yang, Y.J., Mangriotis, M.D., and Shen, Y., 2003, Coupled seismic slip on adjacent oceanic transform faults: *Geophysical Research Letters*, v. 30, doi:10.1029/2002GL016454.



- Fox, C.G., Matsumoto, H., and Lau, T.-K.A., 2001, Monitoring Pacific Ocean Seismicity from an autonomous hydrophone array: *Journal of Geophysical Research*, v. 106, p. 4183-4206.
- Goff, J.A., Fornari, D.J., Cochran, J.R., Keeley, C., and Malinverno, A., 1993, Wilkes transform system and nannoplate: *Geology*, v. 21, p. 623-626.
- Harris, R.A., and Day, S.M., 1993, Dynamics of fault interaction - Parallel strike-slip faults: *Journal of Geophysical Research-Solid Earth*, v. 98, p. 4461-4472.
- Hekinian, R., Bideau, D., Cannat, M., Francheteau, J., and Hebert, R., 1992, Volcanic activity and crust mantle exposure in the ultrafast Garrett transform-fault near 13-degrees-28s in the Pacific: *Earth and Planetary Science Letters*, v. 108, p. 259-275.
- King, G.C.P., Stein, R.S., and Lin, J., 1994, Static stress changes and the triggering of earthquakes: *Bulletin of the Seismological Society of America*, v. 84, p. 935-953.
- Lonsdale, P., 1989, Segmentation of the Pacific-Nazca Spreading Center, 1°N-20°S: *Journal of Geophysical Research*, v. 94, p. 12,197-12,225.
- McGuire, J.J., Jordan, T.H., and Lin, J., 2002, Complexities of transform boundaries in the oceans, *in* Stein, S., and Freymueller, J., eds., *Plate Boundary Zones*, Volume 30: Washington, D.C., AGU, p. 425.
- McKenzie, D.P., 1969, Speculations on the consequences and causes of plate motions: *Geophysical Journal of the Royal Astronomical Society*, v. 18, p. 1-32.
- Menard, H.W., and Atwater, T., 1969, Origin of fracture zone topography: *Nature (London)*, v. 222, p. 1037-1040.
- Perfit, M.R., Fornari, D.J., Ridley, W.I., Kirk, P.D., Casey, J., Kastens, K.A., Reynolds, J.R., Edwards, M., Desonie, D., Shuster, R., and Paradis, S., 1996, Recent volcanism in the Siqueiros transform fault: Picritic basalts and implications for MORB magma genesis: *Earth and Planetary Science Letters*, v. 141, p. 91-108.
- Pockalny, R.A., 1997, Evidence of transpression along the Clipperton Transform: Implications for processes of plate boundary reorganization: *Earth and Planetary*

Science Letters, v. 146, p. 449-464.

Pockalny, R.A., Fox, P.J., Fornari, D.J., Macdonald, K.C., and Perfit, M.R., 1997, Tectonic reconstruction of the Clipperton and Siqueiros Fracture Zones: Evidence and consequences of plate motion change for the last 3 Myr: *Journal of Geophysical Research-Solid Earth*, v. 102, p. 3167-3181.

Searle, R.C., 1983, Multiple, closely spaced transform faults in fast-slipping fracture zones: *Geology*, v. 11, p. 607-610.

Stein, S., and Wysession, M., 2003, *An introduction to seismology, earthquakes, and earth structure*: Malden, MA, Blackwell Publishing Ltd., 498 p.

Toda, S., and Stein, R.S., 2000, Did stress triggering cause the large off-fault aftershocks of the 25 March 1998 M-w=8.1 Antarctic plate earthquake?: *Geophysical Research Letters*, v. 27, p. 2301-2304.

Toda, S., Stein, R.S., Reasenber, P.A., Dieterich, J.H., and Yoshida, A., 1998, Stress transferred by the 1995 M-w = 6.9 Kobe, Japan, shock: Effect on aftershocks and future earthquake probabilities: *Journal of Geophysical Research-Solid Earth*, v. 103, p. 24543-24565.

## CHAPTER 2: Spreading rate dependence of gravity anomalies along oceanic transform faults

### ABSTRACT

Mid-ocean ridge morphology and crustal accretion are known to depend on the spreading rate of the ridge. Slow-spreading mid-ocean ridge segments exhibit significant crustal thinning towards transform and non-transform offsets<sup>1-12</sup>, which is thought to arise from a three-dimensional process of buoyant mantle upwelling and melt migration focused beneath the centres of ridge segments<sup>1,2,4-7,9,10,12</sup>. In contrast, fast-spreading mid-ocean ridges are characterized by smaller, segment-scale variations in crustal thickness, which reflect more uniform mantle upwelling beneath the ridge axis<sup>13-15</sup>. Here we present a systematic study of the residual mantle Bouguer gravity anomaly of 19 oceanic transform faults that reveals a strong correlation between gravity signature and spreading rate. Previous studies have shown that slow-slipping transform faults are marked by more positive gravity anomalies than their adjacent ridge segments<sup>1,2,4,6</sup>, but our analysis reveals that intermediate and fast-slipping transform faults exhibit more negative gravity anomalies than their adjacent ridge segments. This finding indicates that there is a mass deficit at intermediate and fast-slipping transform faults, which could reflect increased rock porosity, serpentinization of mantle peridotite, and/or crustal thickening. The most negative anomalies correspond to topographic highs flanking the transform faults, rather than to transform troughs (where deformation is probably focused and porosity and alteration are expected to be greatest), indicating that crustal thickening could be an important contributor to the negative gravity anomalies observed. This finding in turn suggests that three-dimensional magma accretion may occur near intermediate and fast-slipping transform faults.

---

Published as P. M. Gregg, J. Lin, M. D. Behn, L. G. J. Montési, Spreading rate dependence of the gravity structure of oceanic transform faults, *Nature*, 448, 183-187, 2007.

Reprinted by permission from Macmillan Publishers Ltd: [NATURE] (P. M. Gregg, J. Lin, M. D. Behn, L. G. J. Montési, Spreading rate dependence of the gravity structure of oceanic transform faults, *Nature*, 448, 183-187, 2007.), © 2007



# Spreading rate dependence of gravity anomalies along oceanic transform faults

Patricia M. Gregg<sup>1</sup>, Jian Lin<sup>2</sup>, Mark D. Behn<sup>2</sup> & Laurent G. J. Montési<sup>2</sup>

Mid-ocean ridge morphology and crustal accretion are known to depend on the spreading rate of the ridge. Slow-spreading mid-ocean-ridge segments exhibit significant crustal thinning towards transform and non-transform offsets<sup>1–12</sup>, which is thought to arise from a three-dimensional process of buoyant mantle upwelling and melt migration focused beneath the centres of ridge segments<sup>1,2,4–7,9,10,12</sup>. In contrast, fast-spreading mid-ocean ridges are characterized by smaller, segment-scale variations in crustal thickness, which reflect more uniform mantle upwelling beneath the ridge axis<sup>13–15</sup>. Here we present a systematic study of the residual mantle Bouguer gravity anomaly of 19 oceanic transform faults that reveals a strong correlation between gravity signature and spreading rate. Previous studies have shown that slow-slipping transform faults are marked by more positive gravity anomalies than their adjacent ridge segments<sup>1,2,4,6</sup>, but our analysis reveals that intermediate and fast-slipping transform faults exhibit more negative gravity anomalies than their adjacent ridge segments. This finding indicates that there is a mass deficit at intermediate- and fast-slipping transform faults, which could reflect increased rock porosity, serpentinization of mantle peridotite, and/or crustal thickening. The most negative anomalies correspond to topographic highs flanking the transform faults, rather than to transform troughs (where deformation is probably focused and porosity and alteration are expected to be greatest), indicating that crustal thickening could be an important contributor to the negative gravity anomalies observed. This finding in turn suggests that three-dimensional magma accretion may occur near intermediate- and fast-slipping transform faults.

We analyse the residual mantle Bouguer gravity anomaly (RMBA) from 19 oceanic transform fault systems and their adjacent ridge segments at ultraslow- to fast-spreading mid-ocean ridges (Supplementary Fig. 1) with fault slip rates of 1.3–14.5 cm yr<sup>−1</sup> and fault lengths of 70–350 km (see Methods). RMBA is used to infer local density variations relative to a reference model that includes a 6-km-thick crust. A negative RMBA indicates a mass deficit, which can be due to thickened crust, increased porosity, and/or serpentinized mantle. Conversely, a positive RMBA typically implies crustal thinning. Our results reveal a systematic disparity in the gravity signature between ultraslow-/slow-slipping transform faults and intermediate-/fast-slipping transform faults.

To illustrate these differences, we compare the RMBA at the fast-slipping Siqueiros transform to the RMBA at the slow-slipping Atlantis transform (Fig. 1). The 150-km-long Siqueiros transform located at ~8.3°N on the East Pacific Rise is slipping at ~11.8 cm yr<sup>−1</sup> and includes five fault segments connected by four intra-transform spreading centres<sup>16</sup> (Fig. 1a). The ridge segments to the north and south of Siqueiros are typical of fast-spreading ridges with axial highs as shallow as 2.0–2.8 km. The ridge transform

intersections bounding Siqueiros display overshooting ridge tips<sup>16</sup> typical of ridge transform intersections at magmatically robust ridge segments (Supplementary Figs 2–5). In contrast, the 70-km-long Atlantis transform at 30°N on the Mid-Atlantic Ridge is slipping at ~2.4 cm yr<sup>−1</sup> and contains a single strike-slip fault zone (Fig. 1b). The ridge segments adjacent to the Atlantis transform display slow-spreading rift valleys and a wide range of axial depths.

As seen in previous gravity studies of the Atlantis transform<sup>17,18</sup>, more negative RMBA is associated with adjacent ridge segment centres (up to ~80 mGal less than the transform offset), whereas the most positive RMBA is located in the transform fault and fracture zone (Fig. 1d). In contrast, at Siqueiros more positive RMBA is observed along the adjacent ridge segments and more negative values are found within the transform fault and fracture zone domains (up to ~40 mGal less than the adjacent ridge segments). RMBA minima often correspond to bathymetric highs along the eastern and southern flanks of the fault (Fig. 1c).

The difference in the average RMBA values between transform fault domains and their adjacent ridge segments— $\Delta\text{RMBA}_{\text{T}-\text{R}}$ —varies systematically with spreading rate for the 19 transform faults included in this study (Fig. 2, see Methods section for  $\Delta\text{RMBA}_{\text{T}-\text{R}}$  calculation).  $\Delta\text{RMBA}_{\text{T}-\text{R}} > 0$  implies more positive RMBA along the transform fault domain than along the adjacent ridge segments, whereas  $\Delta\text{RMBA}_{\text{T}-\text{R}} < 0$  implies more negative values within the transform fault domain. Along ultraslow- and slow-spreading ridges, the average RMBA in transform fault domains is systematically more positive than along the adjacent ridge segments with  $\Delta\text{RMBA}_{\text{T}-\text{R}}$  of up to 45 mGal. However, for spreading rates exceeding ~5 cm yr<sup>−1</sup> the average RMBA within transform fault domains becomes more negative than on the adjacent ridge segments. Most intermediate- and fast-slipping transforms are associated with  $\Delta\text{RMBA}_{\text{T}-\text{R}}$  of −4 to −14 mGal, whereas the Blanco transform is associated with a  $\Delta\text{RMBA}_{\text{T}-\text{R}}$  of −40 mGal (Fig. 2 and Supplementary Table 1).

Previous studies attribute positive RMBA along slow-slipping transform faults to decreased crustal accretion towards the end of ridge segments and therefore crustal thinning within the transform fault domain<sup>1,2,4,6</sup>. If the negative RMBA observed at intermediate- and fast-slipping transforms also reflects variations in crustal thickness, these anomalies indicate crustal thickening within the transform domain. However, negative RMBA can also arise from other factors, such as cracking and alteration at transform fault offsets<sup>5,8–10</sup>. Therefore, we use two-dimensional (2D) gravity models to estimate the amplitude of  $\Delta\text{RMBA}_{\text{T}-\text{R}}$  corresponding to: (1) increased rock porosity; (2) serpentinization of mantle peridotite; and (3) crustal thickening (Fig. 3, Supplementary Fig. 7, and Supplementary Methods).

Low seismic velocities recorded in the Clipperton transform and near the Siqueiros transform have been attributed to increased cracking and porosity within the transform domain<sup>15,18</sup>. The observed

<sup>1</sup>Department of Geology and Geophysics, Massachusetts Institute of Technology/Woods Hole Oceanographic Institution Joint Program, <sup>2</sup>Department of Geology and Geophysics, Woods Hole Oceanographic Institution, Woods Hole, Massachusetts 02543, USA.



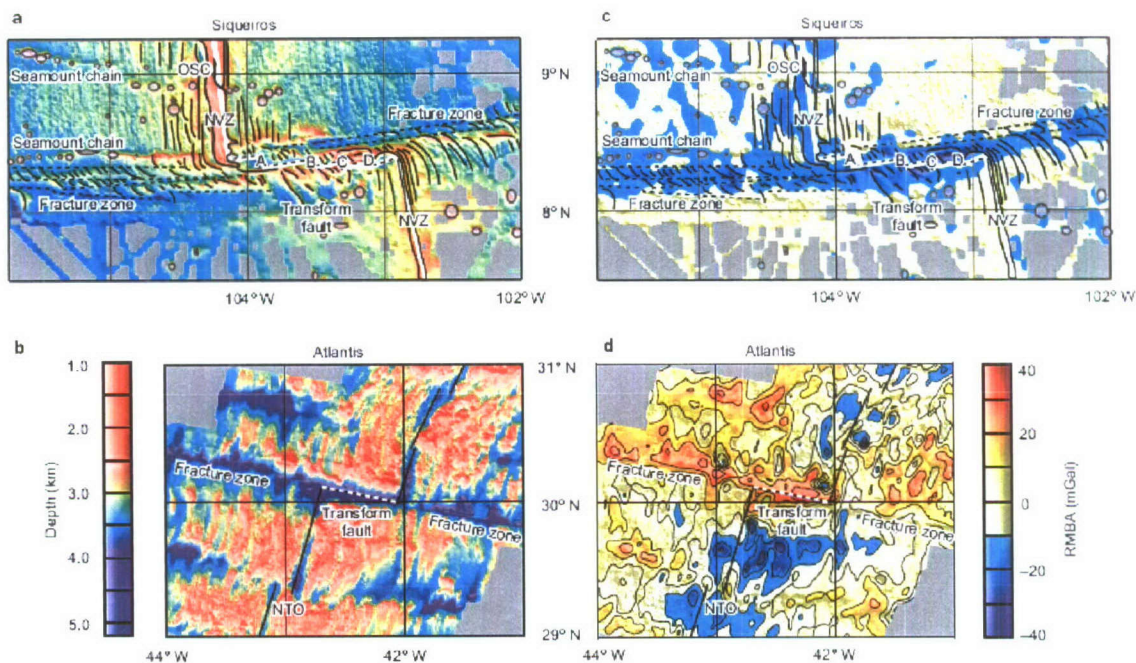


**Figure 1 | Comparison of bathymetry and RMBA of the Siqueiros transform on the East Pacific Rise and Atlantis transform on the Mid-Atlantic Ridge, at the same map scale. a.** Bathymetric map for the Siqueiros transform with geologic interpretation<sup>18</sup>. Solid black lines indicate the seafloor fabric, circles show locations of seamounts, and dashed black lines show the locations of the fracture zones and transform fault. The solid white line indicates the location of the plate boundary used in the 3D thermal model. ITSCs are labelled A, B, C and D<sup>26</sup>. NVZ, neo-volcanic zone; OSC, overlapping

spreading centre. **b.** Bathymetric map for the Atlantis transform. The solid black line indicates location of the plate boundary used in the 3D thermal model, and the dashed portion indicates the Atlantis transform fault. **c.** Calculated RMBA map for the Siqueiros transform fault with geologic interpretation overlaid from **a**. **d.** Calculated RMBA map for the Atlantis transform fault. Seabeam bathymetry compiled by the RIDGE multibeam synthesis project (<http://ocean-ridge.ldeo.columbia.edu/general/html/home.html>).

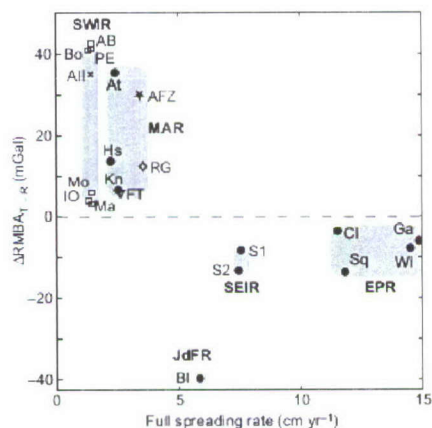


**Figure 2 | Compilation of  $\Delta\text{RMBA}_{T-R}$  values for the 19 transform systems analysed.** The new RMBA calculations from this study are marked with solid circles. Previous RMBA studies are indicated by the open symbols: square<sup>29</sup>, triangle<sup>24</sup>, cross<sup>10</sup>, star<sup>1</sup>, diamond<sup>1</sup>. Abbreviations for ridges: SWIR, Southwest Indian Ridge; MAR, Mid-Atlantic Ridge; JdFR, Juan de Fuca Ridge; SEIR, Southeast Indian Ridge; EPR, East Pacific Rise. Abbreviations for transform faults: Bo, Bouvet; IO, Islas Orcadas; AB, Andrew Bain; PE, Prince Edward; All, Atlantis II; Mo, Moshesh; Ma, Marion; At, Atlantis; Hs, Hayes; Kn, Kane; FT, Fifteen-Twenty; AFZ, Ascension; RG, Rio Grande; BI, Blanco; S2, SEIR2; S1, SEIR1; Cl, Clipperton; Sq, Siqueiros; Wi, Wilkes; Ga, Garrett.

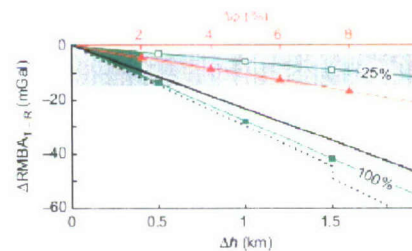


**Figure 3 | Results of 2D forward models showing the predicted  $\Delta\text{RMBA}_{T-R}$ .** Data are shown as a function of increase in crustal thickness through layer 2A (dotted black line) or overall crustal thickening (solid black line); increases in porosity ( $\Phi$ , red line); or the presence of serpentinized mantle (green lines indicate percentage; green shading indicates serpentine stability field).  $\Delta h$  indicates change in layer thickness. Grey shading indicates the observed  $\Delta\text{RMBA}_{T-R}$  at fast-slipping transforms. The kink in the curve for increase in layer 2A corresponds to thickening of layer 2A beyond the thickness of layer 2B in the reference model. See Supplementary Fig. 7 for model details.



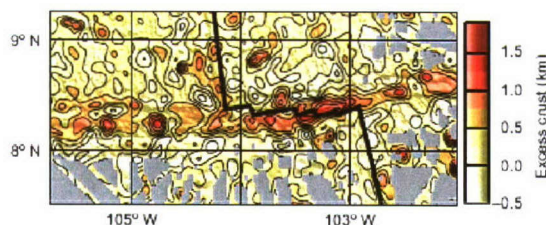


**Figure 4 |** Lateral variations in crustal thickness required to explain the observed RMBA in the Siqueiros transform system (Fig. 1c). Excess crust is defined as the deviation from the reference crustal thickness of 6 km, assuming sea water, crust and mantle densities of 1,030, 2,730 and 3,300 kg m<sup>-3</sup>, respectively.

an increase in porosity in excess of 5% at slow-slipping transforms will negate the effect of crustal thinning and result in negative  $\Delta\text{RMBA}_{T-R}$  (Supplementary Fig. 7). Consequently, a porosity increase of 2–5% is consistent with observed  $\Delta\text{RMBA}_{T-R}$  and seismic data at both slow- and fast-slipping transform faults.

Serpentinization of mantle peridotite can also generate negative  $\Delta\text{RMBA}_{T-R}$ . However, the calculated 500 °C isotherm, which represents the upper limit of serpentine stability<sup>29</sup>, is located within the crust at all fast-slipping transform faults considered in this study (see Methods) and therefore predicts no mantle serpentinization. Invoking hydrothermal cooling (see Supplementary Methods) depresses the 500 °C isotherm to an average depth of 6.4 km at Siqueiros transform fault. Assuming 100% serpentinization (density of 2,550 kg m<sup>-3</sup>) of the mantle where temperatures are <500 °C results in a negative  $\Delta\text{RMBA}_{T-R}$  of 0 to –10 mGal, which is slightly less than the values of up to –14 mGal observed at fast-slipping transform faults (Fig. 3). However, if 100% serpentinization were pervasive above the 500 °C isotherm at slow-slipping transform faults, it would negate the effects of crustal thinning and produce negative  $\Delta\text{RMBA}_{T-R}$  < –100 mGal (Supplementary Fig. 7g). Therefore, although low degrees of mantle serpentinization might contribute to the observed negative RMBA along fast-slipping transform faults, current thermal models for oceanic transform faults make it unlikely that serpentinization alone can explain the systematic differences between fast- and slow-slipping transforms.

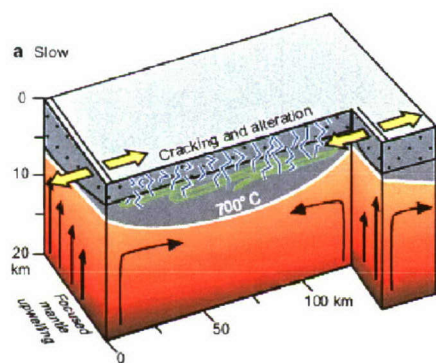
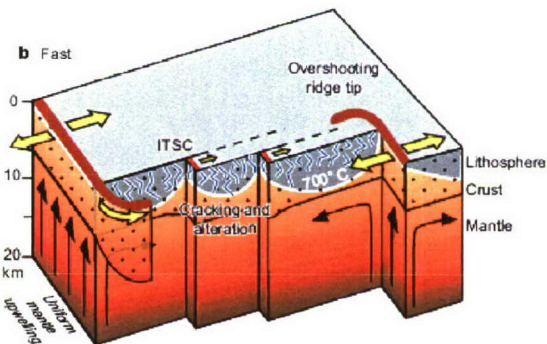


**Figure 5 |** A spreading-rate-dependent model of crustal accretion and mantle upwelling based on observed RMBA calculations and morphological features at transform fault systems on slow- and fast-spreading ridges. Large yellow arrows indicate plate motion vectors; smaller black arrows indicate mantle flow. The grey area with white outline represents the lithosphere as defined by the 700 °C isotherm, while the crust is identified by dotted pattern. The blue cracks and the green wiggles indicate regions of increased porosity and serpentinization, respectively. **a**, Slow-spreading

Finally, we estimate the magnitude of variations in crustal thickness required to explain the RMBA observed along the Siqueiros transform by inverting the observed RMBA relative to a reference model with average crustal density of 2,730 kg m<sup>-3</sup> (ref. 1) (Fig. 4). Along the eastern domain of Siqueiros transform, we predict an excess crustal thickness of >1.5 km, while in the western domain of the transform and in the off-axis fracture zones excess crust ranges from 0.5–1.5 km. The  $\Delta\text{RMBA}_{T-R}$  observed at fast-slipping transform faults can also be produced by increasing layer 2A by 0.25–0.6 km (Fig. 3).

Although increased rock porosity and mantle serpentinization could both contribute to the observed negative RMBA along intermediate- and fast-slipping transform faults, we believe that local crustal thickening is probably the dominant mechanism. Areas of localized deformation, such as fault zones, are expected to exhibit enhanced cracking and alteration. However, the most negative RMBA values observed at intermediate- and fast-slipping transform faults correspond to bathymetric highs flanking the transforms instead of the transform troughs where deformation is likely to be localized. Local excess crust within intermediate- and fast-slipping transform fault domains may result from a combination of magmatic accretion mechanisms including: (1) lateral transport of excess magma from the ridge axis into the transform fault domain<sup>16,21</sup>; (2) magmatic accretion at intra-transform spreading centres<sup>16,22</sup>; (3) the pooling of lava within topographic lows<sup>23</sup>; and/or (4) 'leaky' magmatic accretion along the entire transform fault<sup>24</sup>.

Lateral dyke propagation from a central magma chamber has been proposed to explain crustal thickness variations along slow-spreading ridge segments<sup>25</sup>. At magmatically robust segments along intermediate and fast-spreading ridges, a continuous magma chamber may exist beneath the entire segment and feed dykes from the ridge transform intersection into the transform fault domain. A possible geologic expression of this mechanism is overshooting ridge tips, which are common bathymetric features of robust ridge segments at intermediate- and fast-spreading ridge transform intersections<sup>16</sup> (see Supplementary Figs 2–5). Bathymetry and RMBA of overshooting ridge tips at intermediate and fast-spreading ridges suggest that dykes propagating along the ridge axis penetrate past the transform fault into juxtaposed old oceanic crust, curve in the direction of the transform, and locally increase the crustal thickness of an already full-thickness crust (Fig. 5b). Geologic evidence from the northwestern segment of Blanco transform indicates significant



ridges exhibit focused mantle upwelling at segment centres and crustal thinning towards segment ends and transform faults. **b**, Fast-spreading ridges have relatively uniform mantle upwelling. The negative  $\Delta\text{RMBA}_{T-R}$  at fast-spreading ridges may result from: (1) excess magma supply on ridge segments causing over-shooting ridges and dyke injection into the transform fault domain; (2) increased porosity within the transform; (3) actively accreting ITSCs; (4) pooling of extruded lavas within the transform fault.



increases in the extrusive lava layer with a possible overshooting ridge tip source<sup>23</sup>. However, for this model to explain the RMBA along the entire transform fault (rather than just in the fracture zone), transform-parallel dyke propagation must extend at least half the distance between ridge transform intersections (~50–75 km). Bathymetric data demonstrate that overshooting ridge tips wrap around and into transform faults, but the cause of this curvature is unclear. Possible explanations include response to the local stress field at the ridge transform intersection, and/or dyke propagation along preferential pathways created by pre-existing transform-parallel cracks.

Fast-slipping transform faults typically contain multiple fault segments separated by intra-transform spreading centres (ITSC)<sup>13,26</sup>. Several ITSCs at East Pacific Rise transform faults have been sampled and contain fresh basaltic lavas indicating crustal accretion within the transform fault domain<sup>16,22</sup>. In some cases, such as the Garrett transform fault (Supplementary Fig. 2), the ITSCs occur in pull-apart basins and do not appear to increase the crustal thickness. Alternatively, along the eastern portion of Siqueiros transform (Fig. 1a) ITSCs are associated with negative RMBA. Thus, ITSCs may thicken crust in some localities.

A third possible mechanism for local crustal thickening is the pooling of erupted lavas in topographic lows within the transform fault domain<sup>23</sup> (Fig. 5b). However, the majority of the negative RMBA values we have observed correspond with topographic highs, indicating that this might not be a dominant mechanism. Finally, because off-axis melt is considered abundant at fast-spreading ridges<sup>27</sup>, 'leaky' magmatic accretion might occur along the entire length of some transform faults<sup>24</sup>. This mechanism could cause increases in crustal thickness and may be enhanced by trans-tensional forces acting upon a transform fault owing to plate motion reorganizations<sup>24</sup>.

Thus the observed negative RMBA values at intermediate- and fast-slipping transform faults may be the result of a combination of mechanisms, including increases in rock porosity, mantle serpentinization and/or crustal thickening. Further detailed constraints are required to distinguish among the potential contributors to the observed gravity anomalies. However, the strong correlation of the negative RMBA with topographic highs flanking the transforms suggests crustal thickening as a potentially important mechanism for at least some of the observed negative RMBA values. Systematic occurrence of crustal thickening, if confirmed, would require a modification of our current understanding of how three-dimensional magma accretion occurs along intermediate- and fast-spreading ridges in the vicinity of transform fault discontinuities.

## METHODS SUMMARY

The mantle Bouguer anomaly was calculated following the method of ref. 1. This technique removes the effect of seafloor topography and 6 km of reference crust from the satellite free air gravity<sup>28</sup>. The RMBA was calculated by removing from the mantle Bouguer anomaly the effects of lithospheric cooling as estimated from a three-dimensional (3D) passive mantle upwelling model calculated using the commercial finite-element modelling software package COMSOL MULTIPHYSICS 3.2 (for model details see Supplementary Tables 1 and 2). The RMBA reflects the deviation of sub-seafloor density structure from the reference model described in Supplementary Table 2. When constructing the thermal models for segmented transform faults, we incorporated the best-known geometry of transform fault segments and assumed steady-state crustal accretion at the ITSCs.

We define  $\Delta\text{RMBA}_{\text{T-R}} = \{(\text{RMBA}_{\text{T}} - \text{RMBA}_{\text{R1}}) + (\text{RMBA}_{\text{T}} - \text{RMBA}_{\text{R2}})\}/2$ , where  $\text{RMBA}_{\text{R1}}$  and  $\text{RMBA}_{\text{R2}}$  are the average RMBA values on the adjacent ridge segments 1 and 2, respectively, and  $\text{RMBA}_{\text{T}}$  is the average RMBA value along the transform fault domain (see Supplementary Fig. 8). Where digital data are available<sup>22,9</sup>,  $\text{RMBA}_{\text{R1}}$  and  $\text{RMBA}_{\text{R2}}$  were calculated by averaging the values at the centre of each adjacent ridge segment within a 20-km-wide and 50-km-long box. At the East Pacific Rise, Juan de Fuca Ridge, and Southeast Indian Ridge, where the transform fault zones are wider owing to segmentation,  $\text{RMBA}_{\text{T}}$  was calculated by averaging over a 20-km-wide swath centred 20 km from the ridge transform intersections. At the Mid-Atlantic Ridge and Southwest Indian Ridge the RMBA values were averaged over a 10-km-wide swath centred 20 km from the

ridge transform intersections. Where digital data are unavailable<sup>13,16</sup>, average values were estimated from published profiles and maps of the transform faults and their adjacent ridge segments.

Full Methods and any associated references are available in the online version of the paper at [www.nature.com/nature](http://www.nature.com/nature).

Received 22 September 2006; accepted 24 May 2007.

1. Kuo, B. Y. & Forsyth, D. W. Gravity anomalies of the ridge transform intersection system in the South Atlantic between 31 and 34° S: Upwelling centers and variations in crustal thickness. *Mar. Geophys. Res.* **10**, 205–232 (1988).
2. Lin, J., Purdy, G. M., Schouten, H., Sempere, J.-C. & Zervas, C. Evidence from gravity data for focused magmatic accretion along the Mid-Atlantic Ridge. *Nature* **344**, 627–632 (1990).
3. Blackman, D. K. & Forsyth, D. W. Isostatic compensation of tectonic features of the Mid-Atlantic Ridge: 25–27°30' S. *J. Geophys. Res.* **96**, 11741–11758 (1991).
4. Lin, J. & Phipps Morgan, J. The spreading rate dependence of three-dimensional mid-ocean ridge gravity structure. *Geophys. Res. Lett.* **19**, 13–16 (1992).
5. Tolstoy, M., Harding, A. & Orcutt, J. Crustal thickness on the Mid-Atlantic Ridge: bulls-eye gravity anomalies and focused accretion. *Science* **262**, 726–729 (1993).
6. Detrick, R. S., Needham, H. D. & Renard, V. Gravity anomalies and crustal thickness variations along the Mid-Atlantic Ridge between 33° N and 40° N. *J. Geophys. Res.* **100**, 3767–3787 (1995).
7. Escartin, J. & Lin, J. Ridge offsets, normal faulting, and gravity anomalies of slow spreading ridges. *J. Geophys. Res.* **100**, 6163–6177 (1995).
8. Minshull, T. A. Along-axis variations in oceanic crustal density and their contribution to gravity anomalies at slow-spreading ridges. *Geophys. Res. Lett.* **23**, 849–852 (1996).
9. Canales, J. P., Detrick, R. S., Lin, J., Collins, J. A. & Toomey, D. R. Crustal and upper mantle seismic structure beneath the rift mountains and across a nontransform offset at the Mid-Atlantic Ridge (35° N). *J. Geophys. Res.* **105**, 2699–2719 (2000).
10. Hooft, E. E., Detrick, R. S., Toomey, D. R., Collins, J. A. & Lin, J. Crustal thickness and structure along three contrasting spreading segments of the Mid-Atlantic Ridge, 33° S–35° N. *J. Geophys. Res.* **105**, 8205–8226 (2000).
11. Bruguier, N. J., Minshull, T. A. & Brozena, J. M. Morphology and tectonics of the Mid-Atlantic Ridge, 7°–12° S. *J. Geophys. Res.* **108**, 2093. doi:10.1029/2001JB000172 (2003).
12. Fujivara, T. et al. Crustal evolution of the Mid-Atlantic Ridge near the Fifteen-Twenty Fracture Zone in the last 5 Ma. *Geochem. Geophys. Geosyst.* **4**, 1024. doi:10.1029/2002GC000364 (2003).
13. Fox, P. J. & Gallo, D. G. A tectonic model for ridge-transform-ridge plate boundaries: Implications for the structure of oceanic lithosphere. *Tectonophysics* **104**, 205–242 (1984).
14. Macdonald, K. C. et al. A new view of the mid-ocean ridge from the behavior of ridge-axis discontinuities. *Nature* **335**, 217–225 (1988).
15. Canales, J. P., Detrick, R., Toomey, D. R. & Wilcock, S. D. Segment-scale variations in the crustal structure of 150–300 kyr old fast spreading oceanic crust (East Pacific Rise, 8°15'N–10°5'N) from wide-angle seismic refraction profiles. *Geophys. J. Int.* **152**, 766–794 (2003).
16. Fornari, D. J. et al. Structure and topography of the Siqueiros transform-fault system—Evidence for the development of intra-transform spreading centers. *Mar. Geophys. Res.* **11**, 263–299 (1989).
17. Blackman, D. K., Cann, J. R., Janssen, B. & Smith, D. K. Origin of extensional core complexes: Evidence from the Mid-Atlantic Ridge at Atlantis Fracture Zone. *J. Geophys. Res.* **103**, 21315–21333 (1998).
18. Van Avendonk, H. J. A., Harding, A. J., Orcutt, J. A. & McClain, J. S. Contrast in crustal structure across the Clipperton transform fault from travel time tomography. *J. Geophys. Res.* **106**, 10961–10981 (2001).
19. Wilkens, R. H., Fryer, G. J. & Karsten, J. Evolution of porosity and seismic structure of upper oceanic crust—Importance of aspect ratios. *J. Geophys. Res.* **96**, 17981–17995 (1991).
20. Ulmer, P. & Trommsdorff, V. Serpentine stability to mantle depths and subduction-related magmatism. *Science* **268**, 858–861 (1995).
21. Karson, J. A., Tivey, M. A. & Delaney, J. R. Internal structure of uppermost oceanic crust along the Western Blanco Transform Scarp: Implications for subaxial accretion and deformation at the Juan de Fuca Ridge. *J. Geophys. Res.* **107**, 2181. doi:10.1029/2000JB000051 (2002).
22. Perfit, M. R. et al. Recent volcanism in the Siqueiros transform fault: Picritic basalts and implications for MORB magma genesis. *Earth Planet. Sci. Lett.* **141**, 91–108 (1996).
23. Begnaud, M. L., McClain, J. S., Barth, G. A., Orcutt, J. A. & Harding, A. J. Velocity structure from forward modeling of the eastern ridge-transform intersection area of the Clipperton Fracture Zone, East Pacific Rise. *J. Geophys. Res.* **102**, 7803–7820 (1997).
24. Menard, H. W. & Atwater, T. Origin of fracture zone topography. *Nature* **222**, 1037–1040 (1969).
25. Fialko, Y. A. & Rubin, A. M. Thermodynamics of lateral dike propagation: Implications for crustal accretion at slow spreading mid-ocean ridges. *J. Geophys. Res.* **103**, 2501–2514 (1998).

26. Gregg, P. M., Lin, J. & Smith, D. K. Segmentation of transform systems on the East Pacific Rise: Implications for earthquake processes at fast-slipping oceanic transform faults. *Geology* 34, 289–292 (2006).
27. Sohn, R. A. & Sims, K. W. W. Bending as a mechanism for triggering off-axis volcanism on the East Pacific Rise. *Geology* 33, 93–96 (2005).
28. Smith, W. H. F. & Sandwell, D. T. Global seafloor topography from satellite altimetry and ship depth soundings. *Science* 277, 1957–1962 (1997).
29. Georgen, J. E., Lin, J. & Dick, H. J. B. Evidence from gravity anomalies for interactions of the Marion and Bouvet hotspots with the Southwest Indian Ridge: Effects of transform offsets. *Earth Planet. Sci. Lett.* 187, 283–300 (2001).
30. Muller, M. R., Minshull, T. A. & White, R. S. Crustal structure of the Southwest Indian Ridge at the Atlantis II Fracture Zone. *J. Geophys. Res.* 105, 25809–25828 (2000).

**Supplementary Information** is linked to the online version of the paper at [www.nature.com/nature](http://www.nature.com/nature).

**Acknowledgements** This work was supported by a National Science Foundation (NSF) Graduate Research Fellowship (P.M.G.), the NSF (M.D.B.), and the Woods Hole Oceanographic Institution Deep Ocean Exploration Institute (J.L. and L.G.J.M.). We are grateful for discussions with J. P. Canales, A. Cruse, H. J. B. Dick, D. Fornari, D. Forsyth, J. Georgen, J. Gregg, T. Grove, G. Hirth, D. Lizarralde, J. McGuire, M. Perfit, H. Schouten, D. Smith and the WHOI geophysics group. This manuscript was greatly improved by a review by R. Buck.

**Author Information** Reprints and permissions information is available at [www.nature.com/reprints](http://www.nature.com/reprints). The authors declare no competing financial interests. Correspondence and requests for materials should be addressed to P.G. ([pgregg@whoi.edu](mailto:pgregg@whoi.edu)).



## METHODS

Because there is an inherent non-uniqueness in gravity calculations, we have created several 2D forward models<sup>31</sup> to quantify the effects of various mechanisms on the gravity signature of a ridge-transform system (Supplementary Fig. 7). The light blue and orange shaded regions in Supplementary Fig. 7 indicate the extent of  $\Delta\text{RMBA}_{\text{T-R}}$  observed along transform faults at slow- and fast-spreading ridges, respectively. The density used for each of the layers is indicated in Supplementary Fig. 7. These values do vary in nature<sup>32-35</sup>.

In the first suite of models we varied the crustal thickness by  $\Delta h$  either entirely as a change of layer 2A, layer 2B, or proportionally throughout the entire crust (Supplementary Figs 7a, b and c, respectively). All three mechanisms act to decrease  $\Delta\text{RMBA}_{\text{T-R}}$  within the range of fast-slipping transforms with  $<1$  km of excess material. Increasing layer 2A requires the least amount of excess material with 0.25–0.6 km. The kink in model A results from increasing layer 2A beyond the thickness of layer 2B.

The second suite of models considers increased porosity in the brittle layer (temperatures  $<600$  °C). Two 3D thermal models were calculated to obtain the average depth to the 600 °C isotherm along the Siqueiros transform fault: (1) the initial 3D passive mantle upwelling model, outlined in the Method (the red dashed line at  $\sim 3$  km depth on Supplementary Figs 7d and e), and (2) a hydrothermally cooled model in which heat conductivity is increased tenfold to 4 km depth (the blue dashed line at 6.4 km depth on Supplementary Figs 7d and e). Density changes due to variations in porosity are defined as:  $\rho(\Phi) = (1 - \Phi)\rho_{\text{rock}} + \Phi\rho_{\text{sw}}$ , where  $\Phi$  is the porosity,  $\rho_{\text{rock}}$  is the density of the host rock, and  $\rho_{\text{sw}}$  is the density of sea water. Assuming that the brittle-ductile transition is at  $\sim 3$  km, porosity would need to be increased 2–7% to achieve the  $\Delta\text{RMBA}_{\text{T-R}}$  values of magnitude  $\sim 14$  mGal observed at fast-slipping transform faults.

Similar calculations were performed for slow-slipping transforms, assuming a thicker brittle layer, as was calculated for the Atlantis transform fault. These results indicate that it is difficult to explain the  $\Delta\text{RMBA}_{\text{T-R}}$  at both fast and slow-slipping transforms simultaneously, assuming similar porosity structures in both regions. Because it is unlikely that there will be large increases in porosity down to 9 km depth at slow-slipping transform faults, even though it is within the pressure constraints suggested by ref. 36, we have rerun the 2D slow-slipping transform model with increased porosity to 6 km depth. While porosity increases in excess of 8% still act to negate the effect of crustal thinning at slow-slipping transform faults, moderate increases of 2–5% are consistent with  $\Delta\text{RMBA}_{\text{T-R}}$  values at both slow- and fast-slipping transform faults (Supplementary Fig. 7e).

The final set of forward models includes serpentinization of the mantle beneath the transform fault (Supplementary Figs 7f and g). As in the porosity models, we have incorporated two 3D thermal calculations at the Siqueiros transform to obtain average depths to the 500 °C isotherm, which limits the serpentine stability field<sup>36</sup> to 2.5 km for uncooled and 6.4 km for hydrothermally cooled lithosphere. Without hydrothermal cooling the 500 °C isotherm lies well within the upper crust and there is no predicted mantle serpentinization. However, if hydrothermal cooling is applied from 0 to 4 km depth, an end member model of 100% serpentinization will result in a  $\Delta\text{RMBA}_{\text{T-R}}$  of  $\sim 10$  mGal, which is the average of the observed  $\Delta\text{RMBA}_{\text{T-R}}$  for fast-slipping transform faults. If a similar model for mantle serpentinization is applied at a slow-slipping transform fault, mantle serpentinization down to the hydrothermally cooled 500 °C isotherm would produce such a large negative RMBA that it would completely offset the effect of crustal thinning, which is inconsistent with observations.

Additionally, we calculated a modified RMBA at the Siqueiros transform using the hydrothermally cooled thermal model and the density for 100% serpentine ( $2,550 \text{ kg m}^{-3}$ ) in all regions of the mantle ( $>6$  km depth) where the temperature is  $<500$  °C. Even though this correction maximizes the effect of serpentine, it decreases the average  $\Delta\text{RMBA}_{\text{T-R}}$  within the Siqueiros transform fault domain by only  $<2$  mGal, and reduces the calculated excess crustal thickness by  $<200$  m.

Laboratory experiments suggest that, if the crust is thinned and mantle upwelling occurs, hydrothermal fluid penetration through thermal cracking and grain boundary wetting will reach only  $\sim 4$ –6 km depth<sup>37</sup>. Therefore, it is unlikely that hydrothermal fluids will penetrate to great enough depths to serpentinize large regions of mantle beneath fast-slipping transform faults. Moreover, depressing the 500 °C isotherm through hydrothermal cooling is inconsistent with calculated earthquake depths at oceanic transform faults<sup>38</sup>. On the other hand, slow-slipping transform faults display significant crustal thinning and are cooler than intermediate- and fast-slipping transform faults, implying that a larger portion of the underlying mantle resides in the serpentine stability field. However, the locally positive RMBA observed at slow-slipping transform faults reflects crustal thinning despite the potential for significant serpentinized peridotite<sup>9</sup>. Together, these results indicate that, while mantle serpentinization may

occur at intermediate and fast-slipping transform faults, the direct contribution of serpentinization to the gravity signature is likely to be negligible.

31. Blakely, R. J. *Potential Theory in Gravity and Magnetic Applications* 378 (Cambridge Univ. Press, New York, 1996).
32. Cochran, J. R., Fornari, D. J., Coakley, B. J., Herr, R. S. & Tivey, M. A. Continuous near-bottom gravity measurements made with a BGM-3 gravimeter in DSV Alvin on the East Pacific Rise crest near 9° 31' N and 9° 50' N. *J. Geophys. Res.* 104, 10841–10861 (1999).
33. Stevenson, J. M., Hildebrand, J. A., Zumberge, M. A. & Fox, C. G. An ocean-bottom gravity study of the southern Juan De Fuca Ridge. *J. Geophys. Res.* 99, 4875–4888 (1994).
34. Johnson, H. P., Pruis, M. J., Van Patten, D. & Tivey, M. A. Density and porosity of the upper oceanic crust from seafloor gravity measurements. *Geophys. Res. Lett.* 27, 1053–1056 (2000).
35. Escartin, J., Hirth, G. & Evans, B. Nondilatant brittle deformation of serpentinites: Implications for Mohr-Coulomb theory and the strength of faults. *J. Geophys. Res.* 102, 2897–2914 (1997).
36. Behn, M. D. & Kelemen, P. B. Relationship between seismic P-wave velocity and the composition of anhydrous igneous and meta-igneous rocks. *Geochim. Geophys. Geosyst.* 4, 1041, doi:10.1029/2002GC00393 (2003).
37. deMarlin, B., Hirth, G. & Evans, B. In *Mid-Ocean Ridges: Hydrothermal Interactions Between Lithosphere and Oceans* (eds German, C. R., Lin, J. & Parsons, L. M.) 318 (American Geophysical Union, Washington DC, 2004).
38. Abercrombie, R. E. & Ekstrom, G. Earthquake slip on oceanic transform faults. *Nature* 410, 74–77 (2001).



## Spreading rate dependence of gravity anomalies along oceanic transform faults

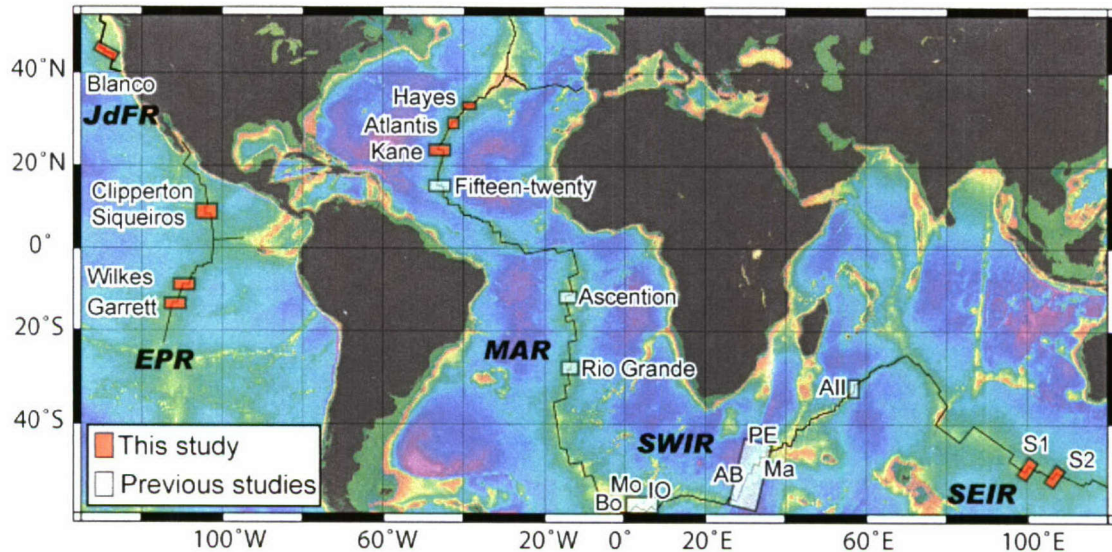
Patricia M. Gregg<sup>1</sup>, Jian Lin<sup>2</sup>, Mark D. Behn<sup>2</sup>, and Laurent G.J. Montési<sup>2</sup>

<sup>1</sup> Dept. of Geology and Geophysics, MIT/WHOI Joint Program, Woods Hole, Massachusetts 02543, USA

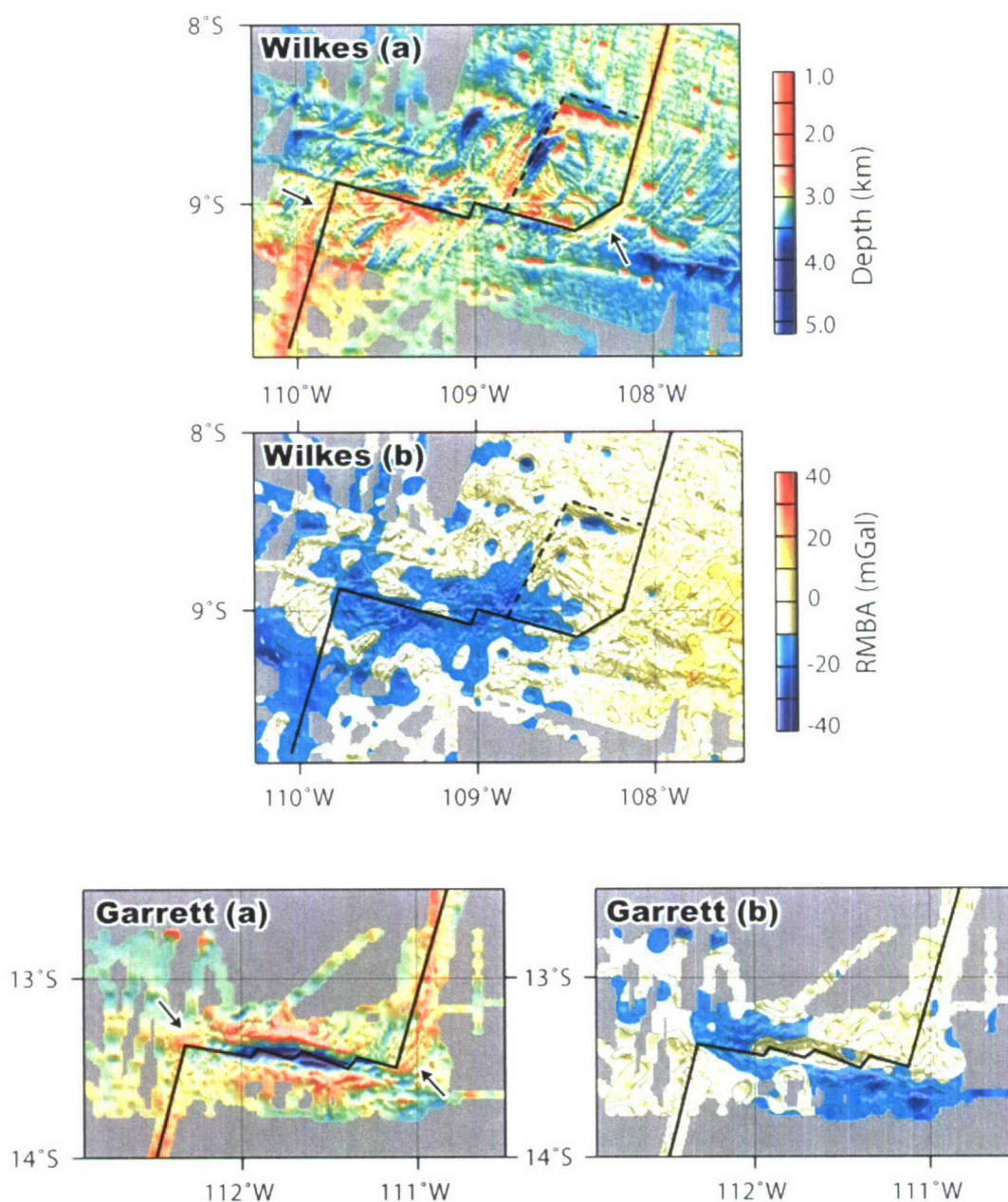
<sup>2</sup> Dept. of Geology and Geophysics, Woods Hole Oceanographic Institution, Woods Hole, Massachusetts 02543, USA

### SUPPLEMENTARY INFORMATION

#### S1. Supplementary Figures

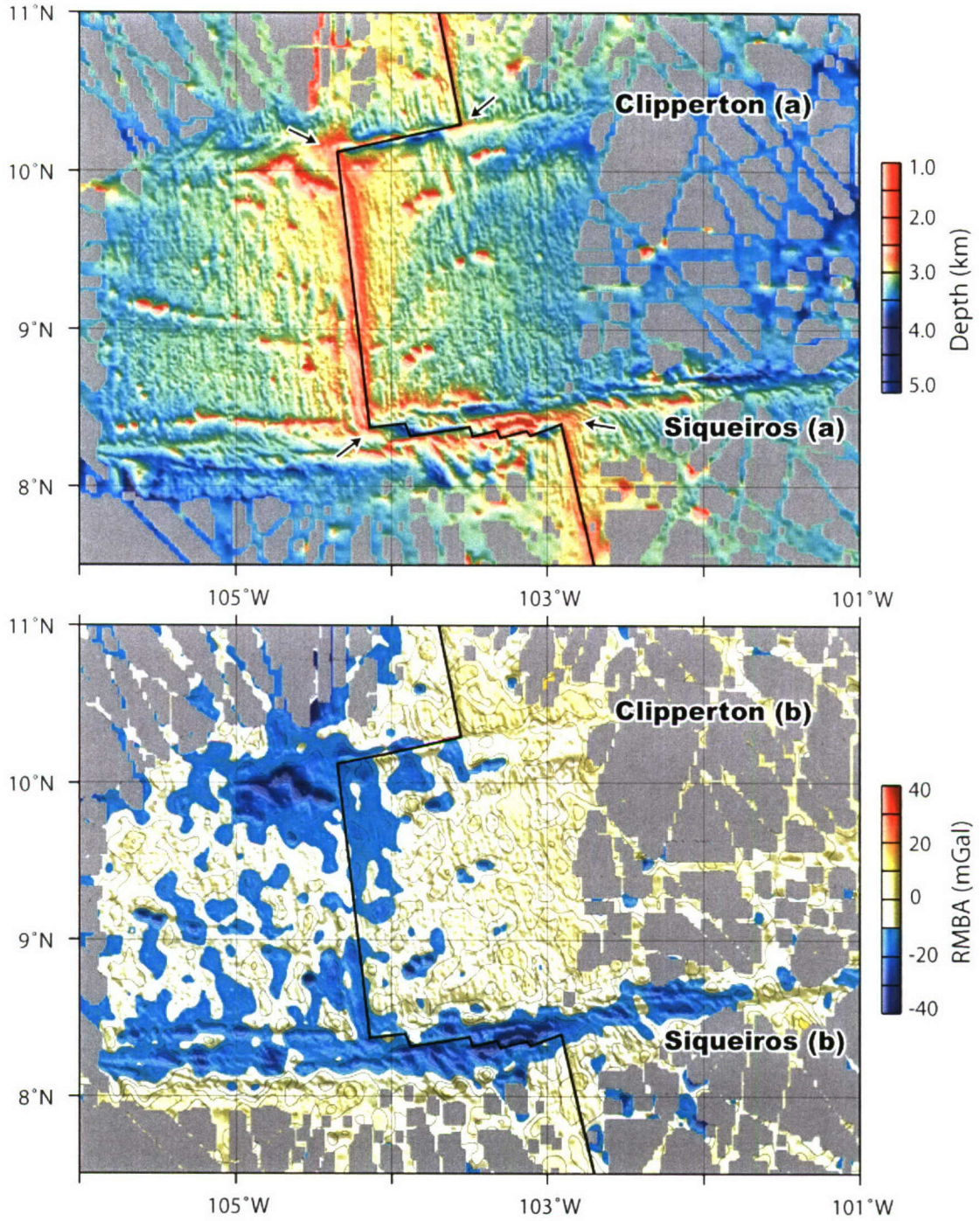


**Supplementary Figure 1.** Bathymetric map indicating the location of the 19 transform faults analyzed. Thin black lines show the location of plate boundaries for the areas of interest. New residual mantle Bouguer anomaly (RMBA) calculations have been performed for transform faults in orange boxes (presented in Supplemental Figs. 2-5). Regions where RMBA calculations have been previously published<sup>1-5</sup> are indicated by transform faults in white boxes. We included previous RMBA studies only if both transform fault and corresponding ridges were analyzed by the same authors using the same parameters. All other RMBA studies we considered from slow-spreading ridges implied  $\Delta\text{RMBA}_{\text{T-R}} > 0$ . MAR – Mid Atlantic Ridge, EPR – East Pacific Rise, JdFR – Juan de Fuca Ridge, SWIR – Southwest Indian Ridge, SEIR – Southeast Indian Ridge, AB – Andrew Bain FZ, Bo – Bouvet FZ, Mo – Moshesh FZ, PE – Prince Edward FZ, AII – Atlantis II FZ, IO – Islas Orcadas FZ, Ma – Marion FZ, S1 – SEIR1, S2 – SEIR2.



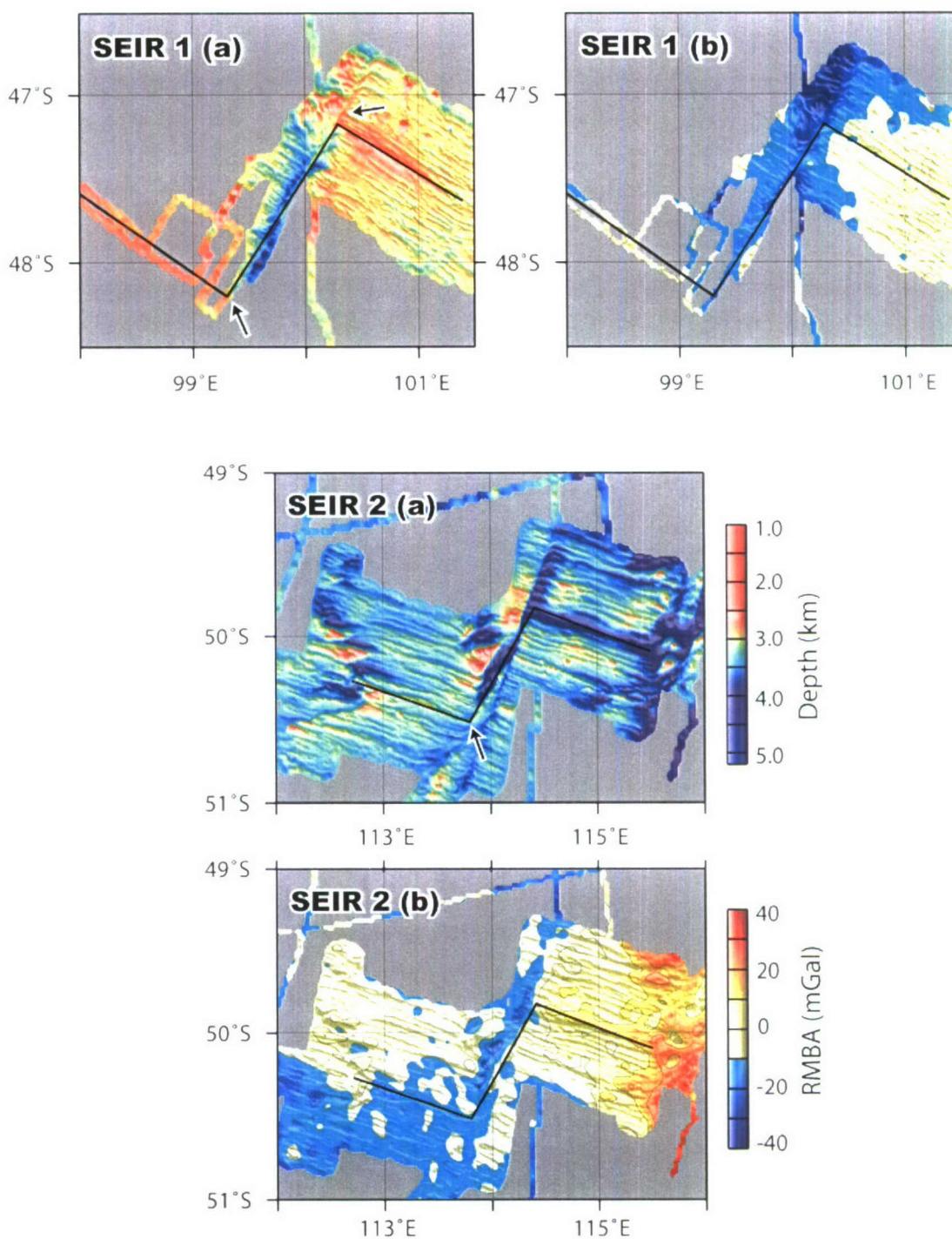
**Supplementary Figure 2.** (a) Seafloor depth and (b) RMBA for the Wilkes and Garrett transform faults on the East Pacific Rise. The solid black line indicates the plate boundary used for 3D thermal models at each region<sup>6,7</sup>. Arrows specify the location of overshooting ridge tips (ORTs) at ridge transform intersections (RTI). The dotted line outlines the Wilkes nanoplate<sup>6</sup>. All supplemental maps (Supplemental Figs 2-6) are at the same map scale.



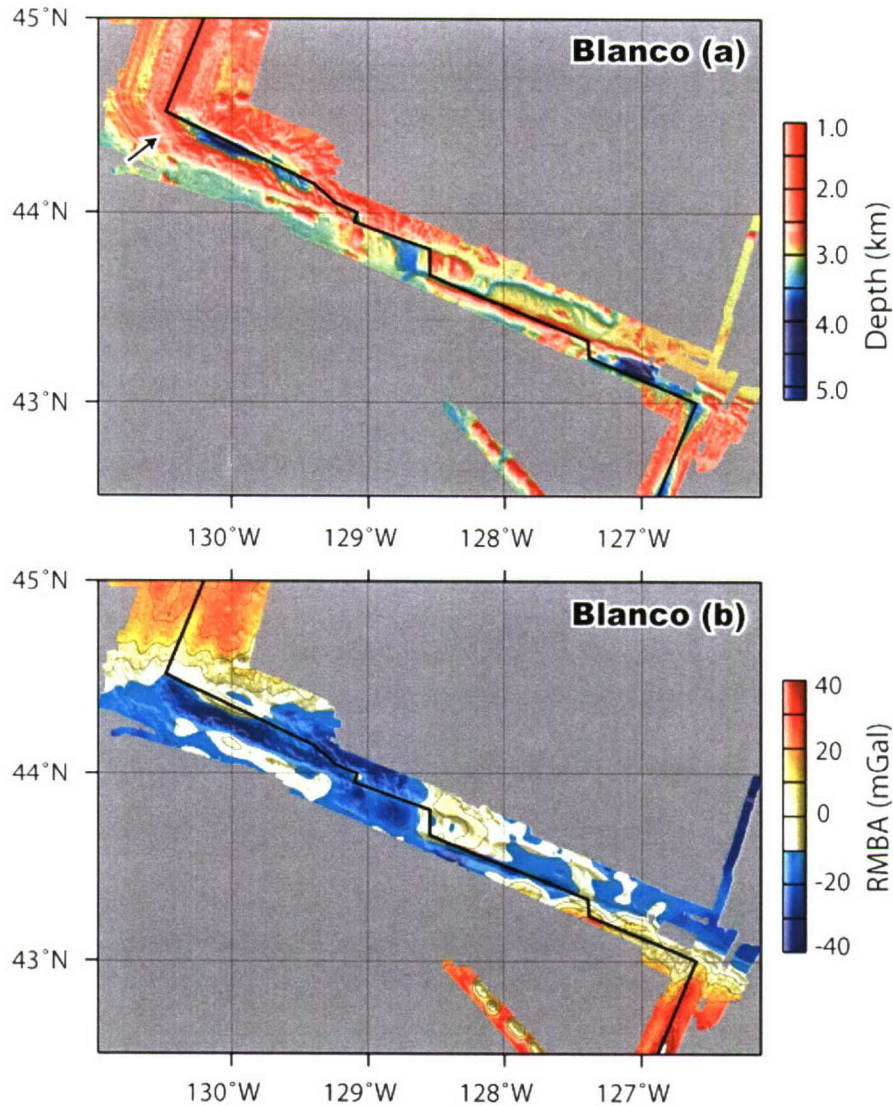


**Supplementary Figure 3.** (a) Seafloor depth and (b) RMBA for the Siqueiros and Clipperton transform faults on the EPR. The solid black line indicates the plate boundary used for the 3D thermal models, and black arrows indicate location of ORTs<sup>8</sup>. Note the Clipperton seamount chain to the south and west of the western RTI.



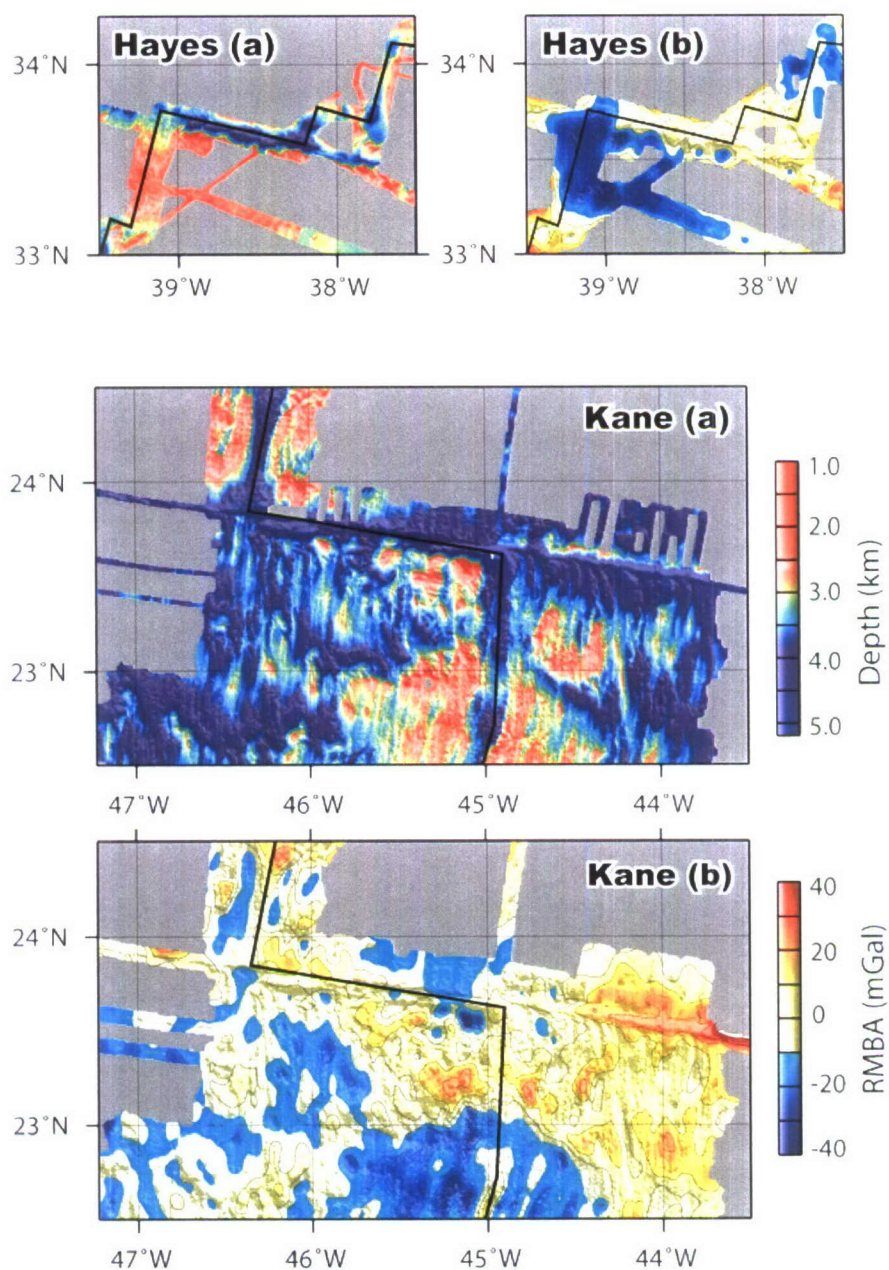


**Supplementary Figure 4.** (a) Scafloor depth and (b) RMBA for Southeast Indian Ridge transform 1 and transform 2. The solid black line indicates the plate boundary used for 3D thermal models at each region<sup>9,10</sup>, and black arrows indicate ORTs.



**Supplementary Figure 5.** (a) Seafloor depth and (b) RMBA for the Blanco transform fault on the Juan de Fuca Ridge. The solid black line indicates the plate boundary used for 3D thermal models at each region<sup>11</sup>. The Blanco transform fault is the most anomalous of the  $\Delta\text{RMBA}_{\text{T-R}}$  calculated (main text Fig. 2). There are several complications in this region, which are not incorporated into the 3D thermal model, including the close proximity to the Cascadia subduction zone as well as a proposed serpentine intrusion forming Blanco Ridge along the southeastern portion of the transform fault ( $\sim 128^\circ\text{W}$ ,  $43.5^\circ\text{N}$ )<sup>11,12</sup>. While a serpentine block has been proposed along the southeastern portion of the transform, the most negative RMBA values are associated with overshooting ridge tip and bathymetric highs along the northwestern portion of the transform fault ( $\sim 130^\circ\text{W}$ ,  $44.25^\circ\text{N}$ ), and are likely due to crustal increases. Karson et al. (2002)<sup>13</sup> note that the extrusive volcanic layer along the northwestern portion of Blanco is substantially thicker than what is predicted by seismic studies in this region. An increase in layer 2A agrees with our observation of negative RMBA along this portion of the Blanco transform.



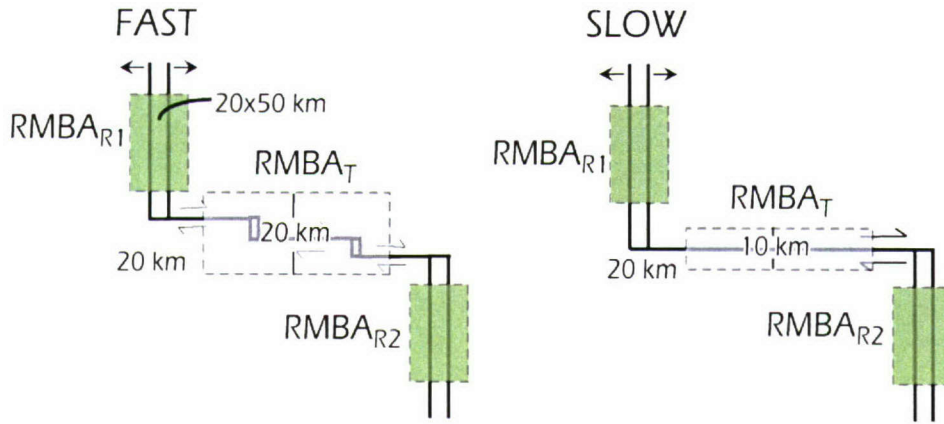


**Supplementary Figure 6.** (a) Seafloor depth and (b) RMBA for the Hayes and Kane transform faults on the Mid-Atlantic Ridge. Clear RMBA “bulls-eye” minima are observed at segment centers, in agreement with previous studies at slow-spreading mid-ocean ridges.





**Supplementary Figure 7.** Three suites of forward models. The calculated  $\Delta\text{RMBA}_{\text{T-R}}$  are plotted on the top panels. The light blue and orange shaded region indicates the extent of  $\Delta\text{RMBA}_{\text{T-R}}$  observed at slow and fast-slipping transform faults, respectively. A) Change in layer 2A thickness (dotted line), B) Change in layer 2B thickness (dashed line), C) Proportional change in crustal thickness (solid black line). D) Porosity increase in the brittle layer at an EPR-type fast-spreading ridge-transform system. The model illustration demonstrates that porosity is increased down to the brittle-ductile transition, the 600°C isotherm, for both an un-cooled (red dashed line) and hydrothermally cooled (blue dashed line) thermal model. The red line with solid red triangles indicates un-cooled 600°C isotherm and blue line with solid blue triangles indicates hydrothermally cooled 600°C isotherm in the model results. E) Porosity increase in the brittle layer at a MAR-type slow-spreading ridge-transform system. The red line with open triangles indicates un-cooled 600°C isotherm and blue line with open triangles indicates hydrothermally cooled 600°C isotherm. Black dashed line indicates the effect of increasing porosity only to 6 km depth. F) Serpentinization of the mantle at an EPR-type system (green line with solid green squares). 100% and 25% serpentinization is shown, and the shaded region marks the serpentine stability field for the hydrothermally cooled ridge-transform system. The model illustration demonstrates that extent of serpentine stability, the 500°C isotherm, for both an un-cooled (red dashed line) and hydrothermally cooled (blue dashed line) thermal model. The depth of the 500°C isotherm represents the average depth calculated by the 3D thermal model within the Siqueiros transform. G) Serpentinization of the mantle at an MAR-type system (green line with open squares). The kinks visible in the 100% and to a lesser extent the 25% curve result when the thickness of the serpentine layer exceeds 6 km depth, the replacement thickness of layer 3.



**Supplementary Figure 8.** A schematic of the calculation of  $\Delta\text{RMBA}_{\text{T-R}}$ .  $\Delta\text{RMBA}_{\text{T-R}} = [(\text{RMBA}_{\text{T}} - \text{RMBA}_{\text{R1}}) + (\text{RMBA}_{\text{T}} - \text{RMBA}_{\text{R2}})]/2$ , where  $\text{RMBA}_{\text{R1}}$  and  $\text{RMBA}_{\text{R2}}$  are the average RMBA values on the adjacent ridge segments 1 and 2, respectively, and  $\text{RMBA}_{\text{T}}$  is the average RMBA value along the transform fault domain. The ridge RMBA values,  $\text{RMBA}_{\text{R1}}$  and  $\text{RMBA}_{\text{R2}}$ , were calculated by averaging the values at the centre of each adjacent ridge segment within a 20 km-wide and 50 km-long box shown by green boxes. At the East Pacific Rise, Juan de Fuca Ridge, and Southeast Indian Ridge, where the transform fault zones are wider due to segmentation,  $\text{RMBA}_{\text{T}}$  was calculated by averaging over a 20 km-wide swath centred 20 km from the RTIs, indicated by the blue boxes. At the Mid-Atlantic Ridge and Southwest Indian Ridge the RMBA values were averaged over a 10 km-wide swath centred 20 km from the RTIs. This convention is also used in determining  $\Delta\text{RMBA}_{\text{T-R}}$  for the 2D models.



## S2. Supplementary Tables

**Supplementary Table 1.** Transform fault characteristics<sup>6-11,23,24</sup>.

| Transform fault | Ridge System | Appx. Latitude | Full-slip rate (cm/yr) | Length (km) | No. of Segments | $\Delta\text{RMBA}_{\text{T-R}}$ (mGals) |
|-----------------|--------------|----------------|------------------------|-------------|-----------------|--|
| Garrett*        | EPR          | 12°S           | 14.9                   | 130         | 4               | -6.0                                     |
| Wilkes          | EPR          | 8°S            | 14.5                   | 100         | 3               | -7.7                                     |
| Siqueiros       | EPR          | 8°N            | 11.8                   | 150         | 5               | -13.6                                    |
| Clipperton      | EPR          | 10°N           | 11.5                   | 90          | 1               | -3.6                                     |
| SEIR 1          | SEIR         | 48°S           | 7.54                   | 135         | 1               | -8.2                                     |
| SEIR 2          | SEIR         | 50°S           | 7.44                   | 80          | 1               | -13.2                                    |
| Blanco          | JdFR         | 42°N           | 5.8                    | 350         | 5               | -39.7                                    |
| Kane            | MAR          | 24°N           | 2.5                    | 160         | 1               | 6.6                                      |
| Atlantis        | MAR          | 30°N           | 2.4                    | 70          | 1               | 35.4                                     |
| Hayes           | MAR          | 34°N           | 2.2                    | 90          | 1               | 13.7                                     |

\* Asymmetry of slip at Garrett transform<sup>23</sup> has been incorporated in the thermal model of Garrett transform fault.

**Supplemental Table 2.** Parameters used in RMBA calculation.

| Parameter  | Value                |
|--|----------------------|
| Sea water density, $\text{kg m}^{-3}$                          | 1,030                |
| Reference crustal density, $\text{kg m}^{-3}$                  | 2,730                |
| Reference mantle density, $\text{kg m}^{-3}$                   | 3,300                |
| Serpentine density (100% serpentinization), $\text{kg m}^{-3}$ | 2,550                |
| Reference crustal thickness, km                                | 6                    |
| Thermal boundary layer thickness, km                           | 100                  |
| Asthenospheric temperature, °C                                 | 1,350                |
| Thermal diffusivity, $\text{m}^2\text{s}^{-1}$                 | $10^{-6}$            |
| Coefficient of thermal expansion, $^{\circ}\text{C}^{-1}$      | $2.4 \times 10^{-5}$ |

### S3. Supplementary References

1. Blackman, D. K. & Forsyth, D. W. Isostatic compensation of tectonic features of the Mid-Atlantic Ridge - 25°-27°30'S. *J. Geophys. Res.* **96**, 11741-11758 (1991).
2. Bruguier, N. J., Minshull, T. A. & Brozena, J. M. Morphology and tectonics of the Mid-Atlantic Ridge, 7°-12°S. *J. Geophys. Res.* **108** (2003).
3. Fujiwara, T. et al. Crustal evolution of the Mid-Atlantic Ridge near the Fifteen-Twenty Fracture Zone in the last 5 Ma. *Geochem. Geophys. Geosyst.* **4** (2003).
4. Georgen, J. E., Lin, J. & Dick, H. J. B. Evidence from gravity anomalies for interactions of the Marion and Bouvet hotspots with the Southwest Indian Ridge: Effects of transform offsets. *Earth Planet. Sci. Lett.* **187**, 283-300 (2001).
5. Muller, M. R., Minshull, T. A. & White, R. S. Crustal structure of the Southwest Indian Ridge at the Atlantis II Fracture Zone. *J. Geophys. Res.* **105**, 25809-25828 (2000).
6. Goff, J. A., Fornari, D. J., Cochran, J. R., Keeley, C. & Malinverno, A. Wilkes transform system and nannoplate. *Geology* **21**, 623-626 (1993).
7. Hekinian, R., Bideau, D., Cannat, M., Francheteau, J. & Hebert, R. Volcanic activity and crust mantle exposure in the ultrafast Garrett transform-fault near 13°28'S in the Pacific. *Earth Planet. Sci. Lett.* **108**, 259-275 (1992).
8. Fornari, D. J. et al. Structure and topography of the Siqueiros transform-fault system - Evidence for the development of intra-transform spreading centers. *Mar. Geophys. Res.* **11**, 263-299 (1989).
9. Cochran, J. R., Fornari, D. J., Coakley, B. J., Herr, R. & Tivey, M. A. Continuous near-bottom gravity measurements made with a BGM-3 gravimeter in DSV Alvin on the East Pacific Rise crest near 9 degrees 31 ' N and 9 degrees 50 ' N. **104**, 10841-10861 (1999).
10. West, B. P. & Sempere, J. C. Gravity anomalies, flexure of axial lithosphere, and along-axis asthenospheric flow beneath the southeast Indian ridge. *Earth Planet. Sci. Lett.* **156**, 253-266 (1998).

11. Dziak, R. P. et al. Recent tectonics of the Blanco Ridge, eastern blanco transform fault zone. *Mar. Geophys. Res.* **21**, 423-450 (2000).
12. Bonatti, E. Vertical tectonism in oceanic fracture zones. *Earth Planet. Sci. Lett.* **37**, 369-379 (1978).
13. Karson, J. A., Tivey, M. A. & Delaney, J. R. Internal structure of uppermost oceanic crust along the Western Blanco Transform Scarp: Implications for subaxial accretion and deformation at the Juan de Fuca Ridge. *J. Geophys. Res.* **107** (2002).
14. Blakely, R. J. *Potential Theory in Gravity and Magnetic Applications* (Cambridge University Press, New York, NY, 1996).
15. Stevenson, J. M., Hildebrand, J. A., Zumberge, M. A. & Fox, C. G. An ocean-bottom gravity study of the southern Juan-De-Fuca Ridge. *J. Geophys. Res.* **99**, 4875-4888 (1994).
16. Johnson, H. P., Pruis, M. J., Van Patten, D. & Tivey, M. A. Density and porosity of the upper oceanic crust from seafloor gravity measurements. *Geophys. Res. Lett.* **27**, 1053-1056 (2000).
17. Escartin, J., Hirth, G. & Evans, B. Nondilatant brittle deformation of serpentinites: Implications for Mohr-Coulomb theory and the strength of faults. *J. Geophys. Res.* **102**, 2897-2914 (1997).
18. Behn, M. D. & Kelemen, P. B. Relationship between seismic P-wave velocity and the composition of anhydrous igneous and meta-igneous rocks. *Geochem. Geophys. Geosyst.* **4** (2003).
19. Ulmer, P. & Trommsdorff, V. Serpentine stability to mantle depths and subduction-related magmatism. *Science* **268**, 858-861 (1995).
20. deMartin, B., Hirth, G. & Evans, B. Experimental constraints on thermal cracking of peridotite at oceanic spreading centers in *Mid-Ocean Ridges: Hydrothermal Interactions Between Lithosphere and Oceans* (eds. German, C. R., Lin, J. & Parsons, L. M.) 318 (American Geophysical Union, Washington, DC, 2004).
21. Abercrombie, R. E. & Ekstrom, G. Earthquake slip on oceanic transform faults. *Nature* **410**, 74-77 (2001).



22. Canales, J. P., Detrick, R. S., Lin, J., Collins, J. A. & Toomey, D. R. Crustal and upper mantle seismic structure beneath the rift mountains and across a nontransform offset at the Mid-Atlantic Ridge (35 degrees N). *J. Geophys. Res.* **105**, 2699-2719 (2000).
23. Conder, J. A., Forsyth, D. & Parmentier, E. M. Asthenospheric flow and asymmetry of the East Pacific Rise, MELT area. *J. Geophys. Res.* **107**, 2344, doi:10.1029/2001JB000807 (2002).
24. Lin, J., Purdy, G. M., Schouten, H., Sempere, J.-C. & Zervas, C. Evidence from gravity data for focused magmatic accretion along the Mid-Atlantic Ridge. *Nature* **344**, 627-632 (1990).

## CHAPTER 3: The effects of mantle rheology and fault segmentation on melt generation and extraction beneath oceanic transform faults

### ABSTRACT

We examine mantle melting and melt extraction beneath fast-slipping, segmented oceanic transform fault systems. Three-dimensional (3-D) mantle flow and thermal structure are calculated using a temperature dependent rheology that incorporates a visco-plastic approximation for the brittle lithosphere. Thermal solutions are combined with the near-fractional, polybaric melting model of *Kinzler and Grove* [1992a, b; 1993] to determine extents of melting as well as major element melt geochemistry. We investigate the mantle source region of intra-transform spreading centers using the melt migration model of *Sparks and Parmentier* [1991] for two end member pooling models: (1) a wide mantle region that incorporates all of the melt focused to the intra-transform spreading center; and (2) a narrow pooling region that assumes melt will not migrate across a transform fault or fracture zone. Models of a 100 km-long transform fault bisected by a single intra-transform spreading center (ITSC) reveal that crustal thickness at the ITSC is primarily dependent on the pooling model and the mantle potential temperature,  $T_p$ . Assuming that melt is pooled into the transform fault domain over a large region of the surrounding mantle (model 1), we find that crustal production is enhanced at ITSCs by up to 3–6.5 km. These model predictions may explain the systematic crustal thickness excesses observed at intermediate and fast-slipping transform faults [*Gregg et al.*, 2007]. Furthermore, we find that the variability in major element lava composition is primarily controlled by  $T_p$ . Applying these techniques to the Siqueiros transform we find that both the visco-plastic rheology and a wide melt pooling region are required to explain the observed variations in both crustal thickness and major element geochemistry. Finally, we find that  $T_p = 1350^\circ\text{C}$  and fractional crystallization at depths of 9–15.5 km fit the majority of the geochemical observations at the EPR 9°N segment and the Siqueiros transform fault system.

---

To be submitted as P. M. Gregg, M. D. Behn, J. Lin, T. L. Grove, The effects of mantle rheology and fault segmentation on melt generation and extraction beneath oceanic transform faults, *J. Geophys. Res.*

## 1. INTRODUCTION

Transform faults are a first order feature of the global mid-ocean ridge system. Transform fault offsets range from 50 km to > 350 km in length and greatly influence the thermal structure, mantle flow dynamics, and melting at mid-ocean ridges [Fox and Gallo, 1984; Parmentier and Forsyth, 1985; Phipps Morgan and Forsyth, 1988]. Investigations of transform faults suggest that cool, deep lithosphere at transform fault offsets effectively divides mid-ocean ridges into unique segments focusing melt toward segment centers and prohibiting shallow across-transform mantle flow. Gravity and seismic studies at slow-spreading ridges indicate along-segment variations in crustal thickness with enhanced magma accretion at ridge segment centers and crustal thinning towards transform and non-transform offsets [Kuo and Forsyth, 1988; Lin et al., 1990; Lin and Phipps Morgan, 1992; Tolstoy et al., 1993; Detrick et al., 1995; Escartin and Lin, 1995; Canales et al., 2000; Hooft et al., 2000]. Juxtaposing the cold, thick lithosphere of a transform fault next to a warm steady-state ridge segment also influences the resultant lava chemistry. The geochemical transform fault edge effect has been noted by several studies and suggests that the cooler mantle region surrounding the transform fault system promotes deeper and lower extents of melting near segment ends [Bender et al., 1978; Bender et al., 1984; Langmuir and Bender, 1984; Langmuir et al., 1986; Reynolds et al., 1992; Reynolds and Langmuir, 1997].

Recent analyses of residual mantle Bouguer gravity anomalies (RMBA) along several intermediate and fast-slipping transform fault systems indicate that for spreading rates  $> \sim 50$  mm/yr full-rate, the observed RMBA values within the transform fault domain are more negative than their adjacent ridge segments [Gregg et al., 2007]. The more negative RMBA calculated within the transform fault domain at fast-slipping transform fault systems indicates a mass deficit within these settings. If the mass deficit is due to crustal thickness variations, these findings contradict the classic model for



transform faults as regions of thin crust relative to adjacent ridge segments. One

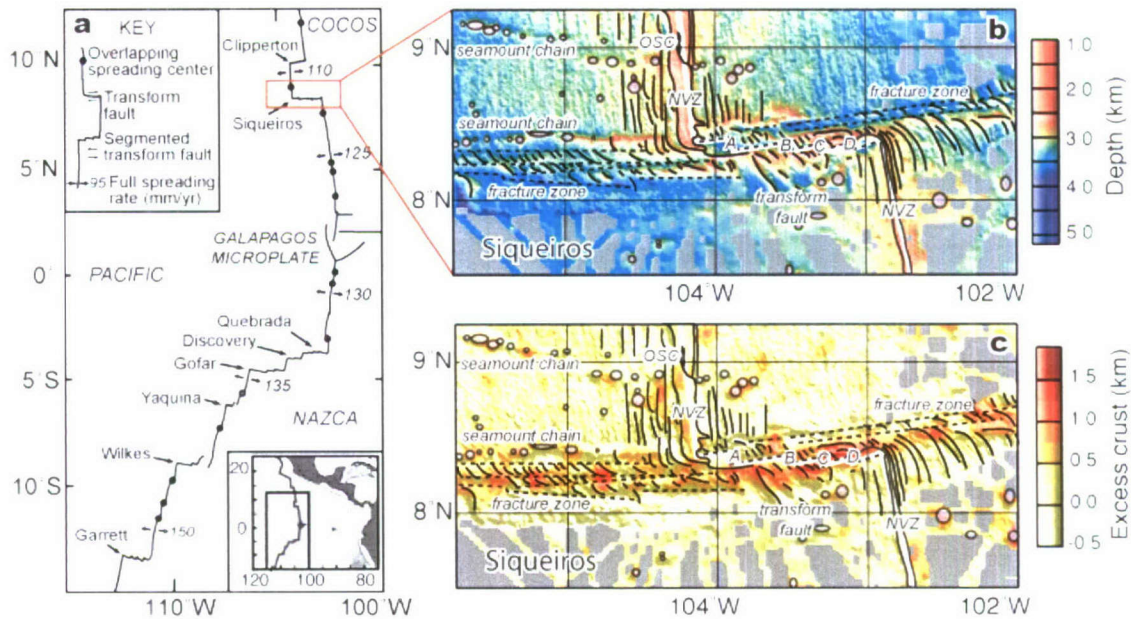


**Figure 1.** Comparison of bathymetry and crustal thickness predictions for Siqueiros transform fault along the EPR. (a) EPR segmentation and location of transform faults. Note that all of the transform faults, except for Clipperton, are segmented by at least one ITSC. (b) Siqueiros transform fault bathymetry with structural interpretation [Fornari *et al.*, 1989]. Solid black lines indicate the seafloor fabric, circles show locations of seamounts, and dashed black lines show the locations of the fracture zones and transform fault. (c) Lateral variations in crustal thickness derived from RMBA calculations. Excess crust is defined as the deviation for the reference crustal thickness of 6 km, assuming seawater, crust and mantle densities of 1030, 2730, and 3300 kg m<sup>-3</sup>, respectively.

explanation for these observations is that long-lived spreading centers within a transform fault system may focus mantle upwelling beneath the transform domain, warm the fault system and result in excess crustal accretion.

Oceanic transform faults along fast-spreading ridges are often characterized by segmentation by intra-transform spreading centers [Menard, 1967; Menard and Atwater, 1969; Searle, 1983; Fox and Gallo, 1984]. In the case of several transform fault systems along the fast-spreading East Pacific Rise (EPR) (e.g., Siqueiros, Garrett, Gofar, Discovery, and Quebrada transform systems), fresh basalts sampled on ITSCs and detailed magnetic data suggest accretion is actively occurring [Fornari *et al.*, 1989; Carbotte and Macdonald, 1992; Hekinian *et al.*, 1992; Hekinian *et al.*, 1995; Perfit *et al.*, 1996; Nagle *et al.*, 2007]. Segmentation of oceanic transform faults is generally thought to be the result of transtensional forces imposed on the transform fault zone by plate motion reorganization of the mid-ocean ridge system [Menard and Fisher, 1958; Menard and Atwater, 1969]. Specifically, the change in spreading direction enables mantle upwelling beneath the transform fault domain and the formation of small intra-transform spreading centers (ITSC) [Searle, 1983; Fornari *et al.*, 1989; Pockalny, 1997; Pockalny *et al.*, 1997].

In this study, we develop 3-D models of ridge-transform-ridge systems to explore the effect of transform segmentation on mantle flow, melt generation, and melt extraction. Recent modeling investigations of ridge-transform-ridge systems have illustrated the importance of incorporating visco-plastic rheology into thermal models of these settings [Behn *et al.*, 2007]. We compare the results of models with both a constant viscosity rheology and a visco-plastic rheology that approximates a brittle lithosphere [Chen and Morgan, 1990; Behn *et al.*, 2007]. Calculated thermal structures are used in conjunction with the fractional melting model of Kinzler and Grove [1992a, b; 1993] and fractional crystallization model of Yang *et al.* [1996] to calculate crustal thickness and predict major element lava compositions. First, crustal thickness and lava composition are calculated in 2-D and compared to observations at 9°N on the EPR to calibrate parameters such as mantle potential temperature and the maximum distance of melt



migration. Second, we investigate a suite of generic 3-D transform fault models segmented by a single ITSC. Finally, we consider a case appropriate for the Siqueiros transform fault system (Figures 1b, c) and compare our model-predicted crustal thicknesses and lava composition to geophysical and geochemical observations in this region.

## 2. MODEL SETUP

The 3-D mantle flow field and temperature are calculated using the finite element modeling software COMSOL 3.3 Multiphysics. Mantle flow is driven by the divergence of two plates each moving with a half-spreading rate,  $U_0$  (Figure 2). A stress free boundary is assumed at the base of the model (100 km depth) allowing for convective flux from the mantle below. The sides of the models are also stress free. Potential temperature at the surface ( $T_c$ ) and the base ( $T_p$ ) of the model are set to 0°C and  $T_p$  respectively. The model geometry is varied to explore the effect of fault segmentation by imposing a single ITSC of length,  $L_{ITSC}$ , which bisects a transform fault of length  $L_T$  (Figure 2). All model parameters are given in Table 1.

### 2.1 Numerical Approach

Conservation of mass, momentum, and energy are given by:

$$\nabla \cdot \mathbf{u} = 0 \quad (1)$$

$$\rho \left( \frac{\partial \mathbf{u}}{\partial t} + \mathbf{u} \cdot \nabla \mathbf{u} \right) = -\nabla p + \eta_{tot} \nabla^2 \mathbf{u} \quad (2)$$

$$\rho C_p \mathbf{u} \cdot \nabla T + k \nabla^2 T = 0 \quad (3)$$

where  $\rho$  is the density of the mantle,  $p$  is pressure,  $\mathbf{u}$  is the velocity field,  $\eta_{tot}$  is the mantle viscosity,  $C_p$  is the heat capacity,  $T$  is temperature, and  $k$  is thermal conductivity.



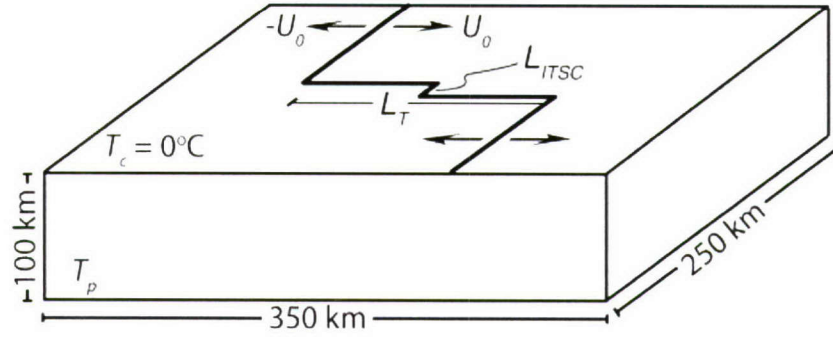


**Figure 2.** 3D setup for modeling mantle temperature structure beneath a segmented transform fault. Spreading velocities are imposed at the surface. Other model parameters include temperatures at the surface,  $T_c$ , and at the base of the model box,  $T_p$ ; the length of transform,  $L_T$ , and the length of intra-transform spreading center,  $L_{ITSC}$ .

Mantle flow and temperature are both largely dependent on the assumed mantle viscosity. To explore the importance of incorporating a visco-plastic rheology, we compare isoviscous solutions to those calculated using a temperature-dependent viscosity that incorporates a visco-plastic approximation for brittle failure [Chen and Morgan, 1990; Behn *et al.*, 2007]. The effective mantle viscosity is defined by:

$$\eta_{tot} = \left( \frac{1}{\eta_{td}} + \frac{1}{\eta_{byr}} + \frac{1}{\eta_0} \right)^{-1} \quad (4)$$

where  $\eta_{td}$  is the temperature dependent viscosity,  $\eta_{byr}$  is a brittle strength approximation using Byerlee's law, and  $\eta_0$  is the maximum viscosity ( $10^{23}$  Pa·s). The temperature dependence of viscosity is approximated by:

$$\eta_{td} = \eta_0 \exp \left( \frac{Q}{R} \left( \frac{1}{T} - \frac{1}{T_p} \right) \right), \quad (5)$$

where  $Q$  is the activation energy and  $R$  is the universal gas constant. The viscosity associated with brittle failure is approximated by [Chen and Morgan, 1990]:

$$\eta_{byr} = \frac{S}{\sqrt{2}\dot{\epsilon}_{II}}, \quad (6)$$

where  $\dot{\epsilon}_{II}$  is the second invariant of the strain rate tensor, and the maximum shear stress,  $S$ , is defined by:

$$S = \frac{2}{5}(p_r - p_w), \quad (7)$$

where  $p_r$  is the lithostatic pressure, and  $p_w$  is the hydrostatic pressure.

The incorporation of a visco-plastic rheology promotes focused mantle upwelling in areas with high strain rates [Behn *et al.*, 2007]. This effect is most pronounced beneath the ridge axis and beneath the transform fault domain where strain rates are particularly high. Therefore, models containing a visco-plastic rheology result in a warmer thermal

structure beneath the ridge axis and transform fault domain than those calculated with a constant viscosity rheology (Figure 3a).

Hydrothermal circulation within the upper crust will promote more effective heat loss and therefore decrease temperatures in the upper mantle [Phipps Morgan *et al.*, 1987; Phipps Morgan and Chen, 1993; Baker *et al.*, 1996; MacLennan *et al.*, 2005]. This effect is likely to be particularly important at oceanic transform faults where extensive brittle deformation increases permeability and produces pathways for fluids to reach greater depths. We assume that hydrothermal circulation is present at temperatures < 600°C and depths < 6 km [Phipps Morgan *et al.*, 1987; Phipps Morgan and Chen, 1993]. Where hydrothermal circulation is assumed to occur we increase the thermal conductivity by an enhancement factor or Nusselt number, Nu [Phipps Morgan *et al.*, 1987]. Because permeability most likely decreases with depth due to increased confining pressure and temperature, the enhancement in conductivity is assumed to decay exponentially as the depth and temperature approach the cutoff values for fluid circulation:

$$k = k_0 + k_0 * (Nu - 1) * \exp\left(A * \left(1 - \frac{T}{T_{max}}\right)\right) * \exp\left(A * \left(1 - \frac{z}{z_{max}}\right)\right), \quad (8)$$

where  $k$  is the effective thermal conductivity,  $k_0$  is the reference thermal conductivity,  $A$  is a smoothing factor,  $T_{max}$  is the cutoff maximum temperature (600°C),  $z$  is depth, and  $z_{max}$  is the cutoff maximum depth (6 km).

## 2.2 Melt Generation and Extraction

Melting within the mantle at mid-ocean ridges is dependent on pressure and temperature as well as the chemical composition of the mantle [Grove *et al.*, 1992; Langmuir *et al.*, 1992; Asimow and Langmuir, 2003]. As such, we utilize the fractional melting model of Kinzler and Grove [1992b; a; 1993], in which mantle melting is a function of temperature, pressure, and mantle composition. The benefit of this method is that the model simultaneously tracks residual mantle and melt compositions, as well as



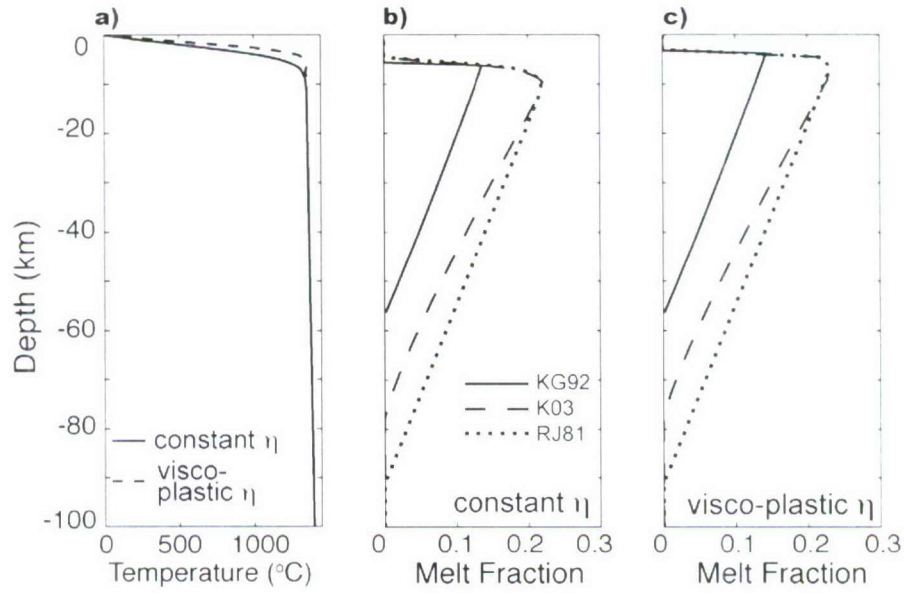


**Figure 3.** Comparison of melting models for two mantle rheologies. (a) Comparison of mantle temperature sampled beneath the oceanic spreading center for constant and visco-plastic rheology models. Calculated melt fraction for constant viscosity rheology model (b) and visco-plastic rheology model (c). The effect of latent heat of melting has been incorporated into all melting models. KG92 – *Kinzler and Grove* [1992a, b; 1993], the solid line; RJ81 – *Reid and Jackson* [1981], the dashed line; and K03 – *Katz et al.* [2003], the dotted line.  $U_0 = 50$  mm/yr,  $T_p = 1350^{\circ}\text{C}$ ,  $\text{Nu} = 4$ , and latent heat of melting,  $L = 400$  J/kg.

extents of melting. The extent of melting and resultant lava composition are predicted using a 3-step process: (1) melt production and composition are calculated at each point in the melting region using polybaric fractional melting; (2) melt migrates to a point at the top of the melt surface and pools; and (3) the pooled melt undergoes fractional crystallization in the shallow mantle lithosphere and lava composition is predicted.

### 2.2.1 Step 1: Fractional Melting

The polybaric fractional melting model of Kinzler and Grove (hereafter “KG92”) utilizes a parameterized solidus derived from experimental data to calculate extents of melting [Kinzler and Grove, 1992b; a; 1993]. Specifically, in the spinel stability field (pressure,  $p \geq 9$  kbars), the solidus temperature,  $T_s$ , is given by the following parameterization:

$$T_s = 1157 + 16*(p - 0.001) - 38.7*(1 - Mg\#) - 181*(NaK\#) - 0*(TiO_2), \quad (9)$$

and in the plagioclase stability field ( $p < 9$  kbars):

$$T_s = 1242 + 9*(p - 0.001) - 120*(1 - Mg\#) - 89*(NaK\#) - 6.6*(TiO_2). \quad (10)$$

The oxides  $TiO_2$ ,  $Na_2O$ ,  $CaO$ , and  $K_2O$  are estimated with the nonmodal batch melting equation:

$$C_{i,m} = \frac{C_0}{(D_{i,s} + F(1 - P_{i,m}))}, \quad (11)$$

where  $C_{i,m}$  is the concentration of oxide ( $i$ ) in the melt ( $m$ ),  $C_0$  is the initial mantle concentration,  $D_{i,s}$  is the bulk partition coefficient of oxide ( $i$ ) in the initial solid ( $s$ ),  $P_{i,m}$  is the bulk partition coefficient of the oxide in the melt, and  $F$  is the melt fraction. The oxide concentrations are calculated iteratively using a bisection method.  $[MgO]_r$  and  $[FeO]_r$  are also calculated iteratively by solving the mass balance equations:

$$[MgO]_b = [MgO]_m F - [MgO]_r (1 - F), \quad (12)$$

$$[FeO]_b = [FeO]_m F - [FeO]_r (1 - F), \quad (13)$$

where  $[MgO]_m$  is the wt. % of MgO in the melt,  $[MgO]_b$  is the wt. % MgO of the initial mantle composition, and  $[MgO]_r$  is the wt. % MgO of the residual mantle. Similarly,  $[FeO]_m$  is the wt. % of FeO in the melt,  $[FeO]_b$  is the wt. % FeO of the initial mantle composition, and  $[FeO]_r$  is the wt. % FeO of the residual mantle. Once the oxides concentrations are determined using equations (11) – (13),  $Mg\#_m$  and  $NaK\#_m$ , the Mg and NaK numbers of the melt, are calculated using the following equations:

$$Mg\#_m = \frac{[MgO]_m}{[MgO]_m + [FeO]_m} \quad (14)$$

$$NaK\#_m = \frac{(Na_2O + K_2O)}{(Na_2O + K_2O + CaO)} \quad (15)$$

It is widely accepted that the process of melt generation beneath a mid-ocean ridge spreading center is adiabatic and occurs over a range of pressures [Klein and Langmuir, 1987]. Therefore, we utilize the polybaric incremental batch melting approach with incomplete melt withdrawal (Model 3 in KG92) to approximate fractional melting of the mantle. This approach assumes a constant melt production rate of 1% melt per 1 kbar of ascent. At each melting increment, 99% of the generated melt is removed and accumulated elsewhere; the remaining melt and depleted mantle ascend another 1 kbar where they are further melted by 1%. As melting proceeds, the latent heat effect of the melting reaction acts to decrease the mantle temperature. We incorporate the change in temperature,  $\Delta T$ , at each step in the calculation as a function of melt fraction, the latent heat of melting,  $L$ , and heat capacity,  $C_p$ , using the following formulation [Turcotte, 1982]:

$$\Delta T = \frac{FL}{C_p}. \quad (16)$$



To determine the temperature structure input into the KG92 melting model, the mantle potential temperature,  $T_p$ , at the base of the model domain is set to a value between 1300°–1400°C. Note that,  $T_p$  is defined as the mantle temperature at the surface extracted along an adiabatic gradient of 0.5°C/km to the base of the model space at 100 km depth. For example, a mantle potential temperature of 1350°C corresponds to a mantle temperature of 1400°C at 100 km depth.

In the original KG92 fractional melting model, pressure controls the cessation of melting, and fractional melting is assumed to stop at 4 kbars. In our implementation of KG92, melting begins when the adiabat crosses the solidus and continues until conductive cooling from the surface depresses the temperature below the solidus. We assume that the mantle is described by a four-phase assemblage (olivine, clinopyroxene, orthopyroxene, and an aluminous phase, either spinel or plagioclase depending on the pressure), and utilize the depleted upper mantle composition (DMM) of *Workman and Hart* [2005] as the initial mantle composition.

### 2.2.2 Step 2: Melt Migration

To calculate the final melt composition and the resultant crustal production, our model must determine how melt migrates from the melting region to a nearby spreading center. Previous 3-D melt migration models have proposed that melt percolating upward through the hot, permeable mantle will pool along a cooler less permeable boundary (e.g., the top of the melting region, the base of the lithosphere, or the cpx-out reaction zone) and then migrate laterally, “uphill”, along this boundary to the ridge axis [*Sparks and Parmentier*, 1991; *Sparks et al.*, 1993; *Magde and Sparks*, 1997; *Magde et al.*, 1997]. To simulate this two-step melt migration process, we assume that melt first migrates vertically to the top of the melting region and then migrates laterally up the slope of the melting region until it reaches a local minimum in the surface, which typically corresponds to a nearby spreading center. Melt migration patterns for the constant and visco-plastic mantle rheology models are shown for a 100 km-long transform fault

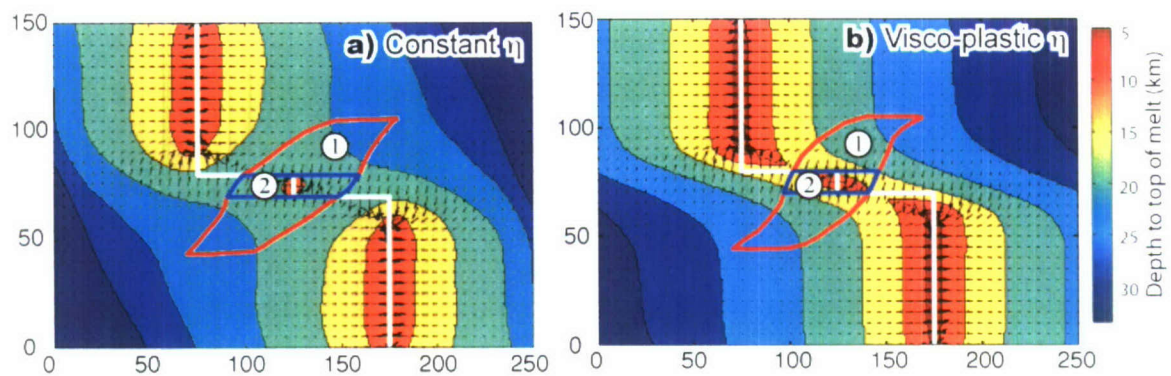


**Figure 4.** Depth to the top of melting with chosen pooling areas for (a) constant viscosity rheology and (b) visco-plastic rheology. Region 1 (delineated by red outline) pools the entire area of melts that have the potential to migrate towards the ITSC. In contrast, region 2 (outlined in blue) assumes that melts will not migrate across the transform fault. Black arrows indicate the gradient of the melt surface and the direction of melt migration.  $T_p = 1350^\circ\text{C}$ ,  $\text{Nu} = 4$ .

bisected by a 10 km-long ITSC (Figure 4). The depth to the top of the melt surface is contoured and the gradient of the surface (black arrows) is plotted to indicate the slope of the melt surface and the direction the melt will migrate.

Uncertainties with the melt migration model include: (1) how far melt will migrate along this boundary before it freezes; and (2) whether melt will be extracted vertically before it reaches the ITSC. To explore these processes, we investigate two end-member scenarios for melt migration beneath the transform fault domain. The first scenario assumes a wide pooling region in which all of the melt projected to migrate to the transform domain will aggregate at the ITSC (solid red lines in Figure 4). The second end-member scenario assumes that melt is unlikely to migrate across a transform fault or fracture zone due to the increased fracture permeability within the fault zone. In this case, melt is only pooled at the ITSC from a narrow region (solid blue lines in Figure 4). These models will be referred to as migration Model 1 – wide pooling region, and Model 2 – narrow pooling region in all subsequent discussions.

Crustal thickness at the ITSC is calculated by integrating the melt production rate over the entire pooling area that is tapped by the ITSC. The integrated melt production rate is then divided by the spreading rate and the length of the ITSC resulting in an average crustal thickness for the entire ITSC [Forsyth, 1993].

### 2.2.3 Step 3: Fractional Crystallization

Finally, to approximate fractional crystallization of the melt prior to eruption we use the approach of *Yang et al.* [1996]. This method assumes isobaric fractional crystallization and calculates the olivine-plagioclase-augite fractional crystallization path as a function of melt composition and pressure between 0.1 to 800 MPa. In our models, crystallization pressure is constrained by the depth at which the mantle no longer melts. *Yang et al.* [1996] uses algebraic relations obtained from experimentally determined phase boundaries for olivine-clinopyroxene-quartz and olivine-clinopyroxene-plagioclase in pseudo-ternary projections, and constraints from mineral-melt exchange reactions



derived from experimentally produced mineral-melt pairs. This model provides major element composition for each step of fractional crystallization.

The compositional information calculated with the *Yang et al.* [1996] approach is used to create liquid line of decent (LLD) plots and to determine proxies such as  $\text{Fe}_{8.0}$  and  $\text{Na}_{8.0}$ , which can be compared to observed major element variations. LLD plots represent the crystallization path the melt will take as it cools in the shallow parts of the mantle. Transitions in the crystallizing phase are illustrated by the kinks in the slope of the lines, which in most cases represent the transitions from the equilibrium phases of olivine + melt, to olivine + plagioclase + melt, to olivine + plagioclase + clinopyroxene + melt. LLD predictions for the oxides FeO and  $\text{Na}_2\text{O}$  are used as proxies for depth and extent of melting respectively.

### 3. NUMERICAL MODELING RESULTS

#### 3.1 Benchmark: Comparison to EPR 9°N

Lava compositions are first calculated in 2-D and compared to observations of crustal thickness and lava composition at 9°N on the EPR [Batiza and Niu, 1992; Canales *et al.*, 2003] to calibrate parameters such as  $T_p$  and the maximum horizontal distance for melt migration,  $W_{pool}$ . For a constant viscosity rheology, crustal thickness calculated for  $T_p = 1325^\circ\text{C} - 1350^\circ\text{C}$  correlates well with the seismic observations (Figure 5a). While pooling melt over a wider region results in greater crustal thicknesses, incorporating hydrothermal cooling ( $\text{Nu} = 4$  and 8) decreases the predicted crustal thickness (Figure 5a). As discussed above, the visco-plastic rheology produces a warmer temperature structure beneath the ridge axis resulting in thicker crust, and we find that  $T_p = 1325^\circ\text{C}$  best fits the observations at 9°N (Figure 5b). Incorporation of hydrothermal cooling with the visco-plastic rheology further focuses mantle upwelling beneath the ridge creating larger upwelling velocities and slightly thicker crust (Figure 5b).

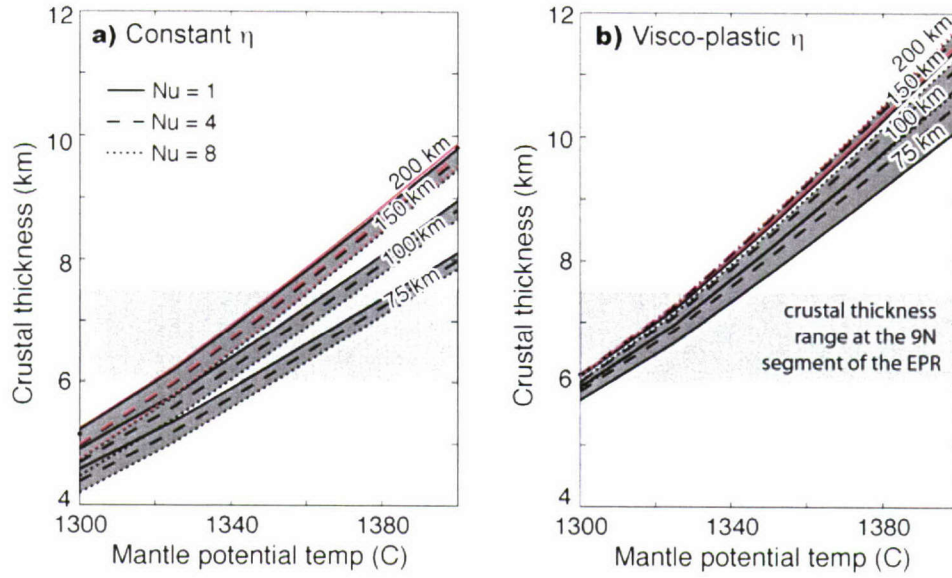


**Figure 5.** Comparison of the predicted crustal thickness at the ridge axis for various widths of the melt pooling regions ( $W_{pool} = 200, 150, 100,$  and  $75$  km) and hydrothermal cooling ( $Nu = 1, 4,$  and  $8$ ) for (a) constant viscosity rheology and (b) visco-plastic rheology. The light gray shaded region indicates the seismic crustal thickness variations observed at the  $9^{\circ}\text{N}$  segment of the EPR [Canales *et al.*, 2003].

We also investigate the sensitivity of  $\text{Fe}_{8,0}$  and  $\text{Na}_{8,0}$  to  $T_p$  and  $W_{pool}$  (Figure 6).  $\text{Fe}_{8,0}$  and  $\text{Na}_{8,0}$  are normalizations of wt. % FeO and wt. %  $\text{Na}_2\text{O}$  to 8 wt. % MgO [Klein and Langmuir, 1987].  $\text{Fe}_{8,0}$ , which is classically viewed as a proxy for the mean pressure of melting, increases as the pressure/depth of melting increases. Since Na is highly incompatible,  $\text{Na}_{8,0}$  is generally used as a proxy for the extent of melting, decreasing as the extent of melting increases. As  $T_p$  increases the depth of the onset of melting consequently increases, resulting in higher values of  $\text{Fe}_{8,0}$  (Figure 6). Additionally, raising  $T_p$  increases the extent of melting and thus  $\text{Na}_{8,0}$  is predicted to decrease (Figure 6). However, while  $\text{Fe}_{8,0}$  and  $\text{Na}_{8,0}$  are strongly dependent on  $T_p$ , they vary only slightly with mantle rheology and  $W_{pool}$ .

To calibrate the values for  $T_p$  and  $W_{pool}$  used in our models, we compare our 2-D ridge results to the geochemical observations of Batiza and Niu [1992]. The Batiza and Niu [1992] database is comprised of major element basaltic glass data from a comprehensive dredging program at  $\sim 9\text{-}10^\circ\text{N}$  along the EPR and its flanks. Specifically we find that,  $T_p = 1350^\circ\text{C}$ ,  $\text{Nu} = 4$ , and  $W_{pool} = 75\text{km}$  results in a reasonably good fit to the observed FeO and  $\text{Na}_2\text{O}$  data (Figure 7a, c). The pressure at the top of the melting triangle varies for each model run depending on  $T_p$  (solid black line in Figure 7). For  $T_p = 1350^\circ\text{C}$  the top of the melting region is 2.4 kbars for the constant viscosity model and 2.0 kbar for the visco-plastic rheology model. The dotted line indicates fractional crystallization at 0.2 kbars.

For models with a visco-plastic rheology, a  $T_p = 1325^\circ\text{C}$  provides the best match to the seismically observed crustal thicknesses at the EPR  $9^\circ\text{N}$  (Figure 5). However,  $T_p = 1350^\circ\text{C}$  better predicts the  $\text{Na}_2\text{O}$  and FeO values observed in microprobe analyses of glass samples from the EPR  $9^\circ\text{N}$ . There is also a discrepancy in the prediction of  $\text{Fe}_{8,0}$  and  $\text{Na}_{8,0}$ . The Batiza and Niu [1992] data indicate an  $\text{Fe}_{8,0}$  of  $\sim 9$ , which corresponds to our model prediction with  $W_{pool} = 75\text{ km}$  and  $T_p = 1325^\circ\text{C}$  (Figure 6). Furthermore, the Batiza and Niu [1992] data indicate  $\text{Na}_{8,0} \sim 2.4$ , which corresponds to our model prediction with  $T_p = 1360^\circ\text{C}$ . Some possible explanations for this disagreement include



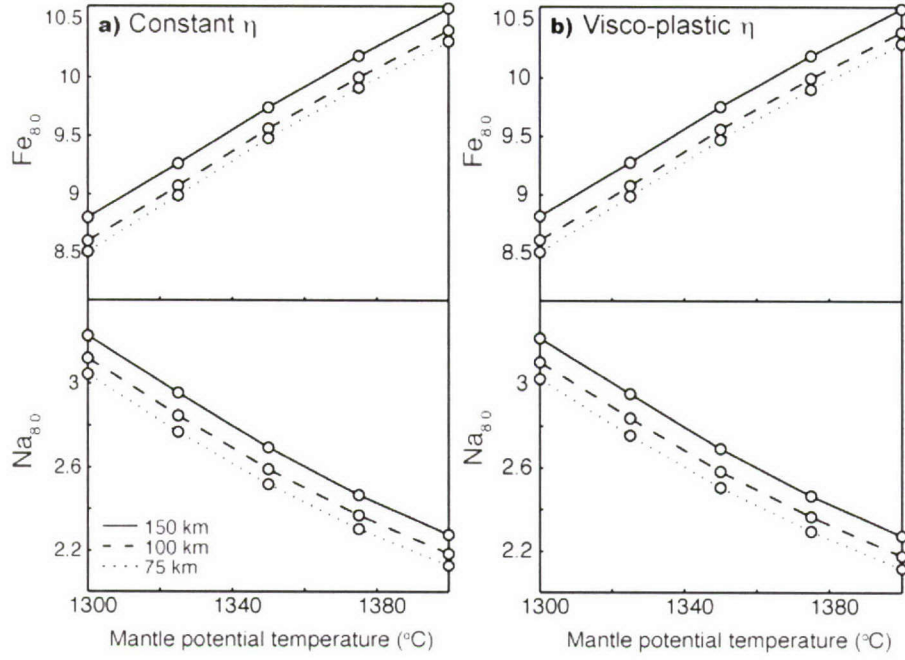


**Figure 6.** Calculated  $\text{Na}_{8,0}$  and  $\text{Fe}_{8,0}$  as a function of mantle potential temperature,  $T_p$ .  $T_p = 1350^\circ\text{C}$  and  $\text{Nu} = 4$ , for  $W_{\text{pool}} = 75 \text{ km}$ ,  $100 \text{ km}$ , and  $150 \text{ km}$ . (a) Constant viscosity rheology and (b) visco-plastic rheology. Open circles indicate values from individual model runs.

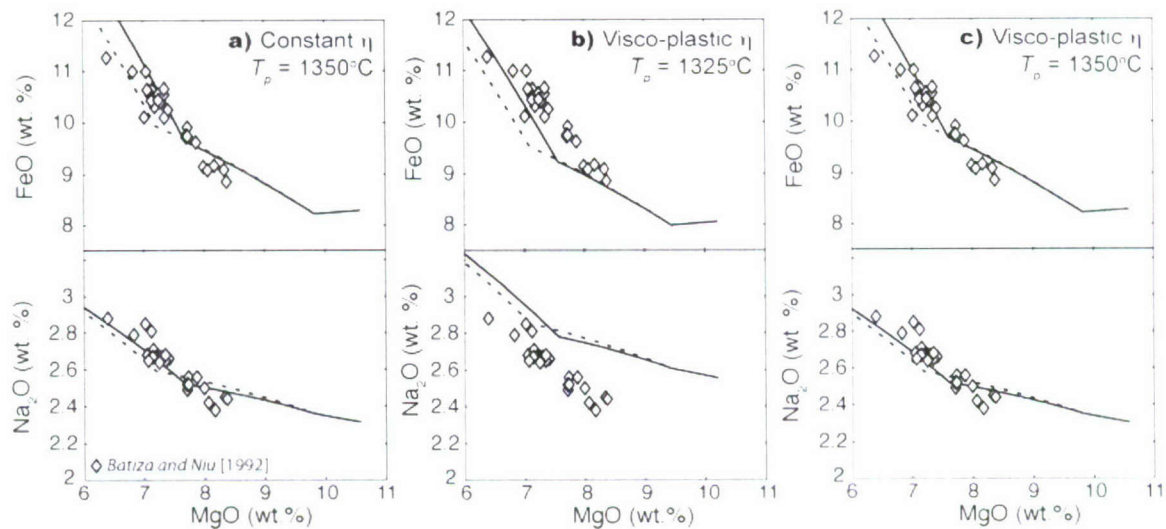


**Figure 7.** Calculated FeO (top panels) and Na<sub>2</sub>O (bottom panels) vs. MgO for 2D models of a ridge with a half spreading rate of 50 mm/yr,  $W_{pool} = 75$  km, and  $Nu = 4$ . Data points are from major element microprobe analyses of basalt glass samples collected along the 9°N segment of the EPR by *Batiza and Niu* [1992]. (a) Constant viscosity rheology model with  $T_p = 1325^\circ\text{C}$ . The solid black line indicates fractional crystallization at top of the melt column and the dashed line indicates crystallization at 0.2 kbars. Mantle potential temperature,  $T_p = 1350^\circ\text{C}$ . (b) Models for visco-plastic rheology with  $T_p = 1325^\circ\text{C}$ . (c) Models for visco-plastic rheology with  $T_p = 1350^\circ\text{C}$ .

mantle source heterogeneities, variations in the assumed melt production rate of 1% melt per kbar, and differences in the radius of melt pooling. Based on our 3-D model results, described later, we believe that these discrepancies arise from complexities in the pattern of melt migration, which controls crustal thickness variations. Because  $T_p = 1350^\circ\text{C}$  provides the best match to the major element compositions and  $T_p = 1325^\circ\text{C}$  best matches the crustal thickness data, we investigate 3-D models in later sections with both of these temperature constraints.

We also compare the melt productivity predicted by KG92 with two other melt models, *Reid and Jackson* [1981] (referred to as “RJ81”) and *Katz et al.* [2003] (hereafter “K03”). RJ81 incorporates a pressure-temperature solidus relationship and calculates melting linearly as a function of the difference between the temperature of the mantle and of the solidus at a given pressure. K03 incorporates the *Hirschman* [2000] solidus into a parameterized equation for mantle melting. KG92 differs from the melting approximations of the RJ81 and K03 models because its solidus is reached at shallower depths in the mantle [*Reid and Jackson*, 1981; *Katz et al.*, 2003]. As a result, the KG92 model produces lower extents of melting than the K03 and RJ81 models. Calculated maximum melt fractions,  $F_{max}$ , for the KG92 model reach only 13.9% for the constant viscosity case and 14.5% for visco-plastic rheology (Figures 3b, c). In contrast,  $F_{max}$  for RJ81 is 22.1% for constant viscosity and 25.5% for visco-plastic rheology, while  $F_{max}$  for K03 is 22.3% for constant viscosity and 27.4% for a visco-plastic rheology (Figures 3b, c). Mean extents of melting range from 5-6% for KG92, 9-10% for RJ81, and 7-9% for K03. These differences become increasingly important when estimating production of crust and the predicted lava composition. To match the crustal thicknesses observed at the EPR 9°N segment, the RJ81 and K03 models require much shorter distances of melt migration to the ridge axis and/or lower values of  $T_p$  compared to KG92.



### 3.2 3D Segmented transform fault results

We investigate the effects of fault segmentation on melt production and migration by exploring a series of models for different ITSC lengths (Figure 2). Using the ridge parameters that best fit the 2-D models at the EPR 9°N, we assume  $T_p = 1350^\circ\text{C}$ ,  $\text{Nu} = 4$ , and  $U_0$  of 50 mm/yr for the constant viscosity models and  $T_p = 1325^\circ\text{C}$  and  $1350^\circ\text{C}$ , for the visco-plastic rheology models. Similar to the 2-D results, for a specific value  $T_p$  the principal factor controlling crustal thickness is the size of the region over which melt is pooled (Figure 8). This is illustrated by investigating the change in crustal thickness,  $\Delta t_c$ , at the ITSC as compared to a reference crustal thickness of 6 km. For the wide melt pooling (Model 1) we find that as  $L_{ITSC}$  is increased,  $\Delta t_c$  decreases (Figure 8). This is because, regardless of their length, ITSCs pool melt from a similar sized mantle region. Hence, when the pooled melt is averaged over the length of the ITSC, there is a larger effect on predicted crustal thickness for shorter ITSCs. As the length of the ITSC increases, it behaves more like a steady-state ridge segment. For narrow pooling (Model 2) as the ITSC length is increased, the predicted crustal thickness also increases (Figure 8). Compared to calculations with a constant viscosity, the visco-plastic rheology model promotes focused upwelling in regions of increased strain rate beneath the transform and thus systematically predicts greater variations in crustal accretion.

Fault segmentation also influences melt composition at the ITSCs. For both wide and narrow melt pooling models, calculations with a constant viscosity predict both  $\text{Fe}_{8.0}$  and  $\text{Na}_{8.0}$  to decrease as the length of the ITSC increases (Figure 9a). These trends suggest that the extent of melting increases and the pressure of melting decreases as the ITSC length increases. This is consistent with the predicted mantle thermal structure, because increasing the length of the ITSC will eventually create a warmer, steady-state ridge segment with higher extents of melting and melting to shallower depths.

In contrast, cases with a visco-plastic rheology predict relatively uniform lava composition within the transform fault domain (Figure 9b). This occurs because the visco-plastic rheology predicts an overall warmer thermal structure at the ITSC, which is

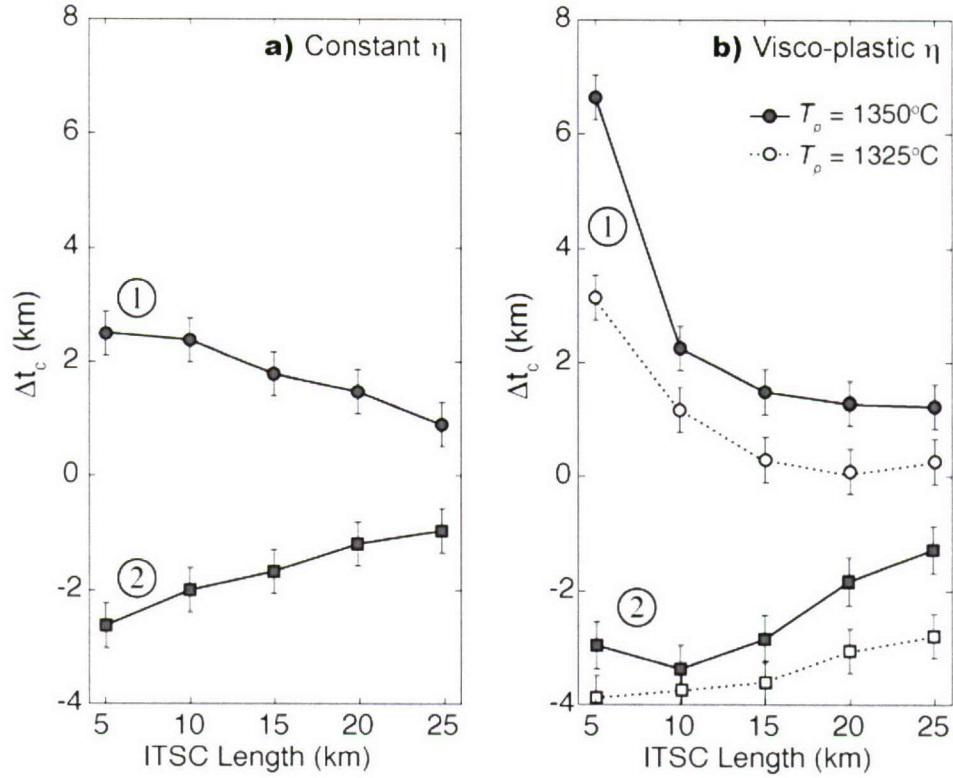


**Figure 8:** Calculated change in crustal thickness,  $\Delta t_c$ , as a function of  $L_{\text{ITSC}}$ , where  $\Delta t_c$  is defined as the difference between the predicted 3D crustal thickness at the ITSC and a reference model assuming 6 km of crust. Calculations were done for (a) constant viscosity rheology and (b) visco-plastic rheology. Model 1 incorporates melt from the wide pooling region (circle symbols), while Model 2 is for the narrow melt pooling region model (square symbols). Each symbol is the result of a single 3D model run. Top and bottom error bars indicate the range in the calculated crustal thickness by using the melt surface contour of 0.05 and 0.1, respectively. Calculations with  $T_p = 1350^\circ\text{C}$  and  $\text{Nu} = 4$  are indicated by filled symbols, whereas models with  $T_p = 1325^\circ\text{C}$  and  $\text{Nu} = 4$  are indicated by open symbols.

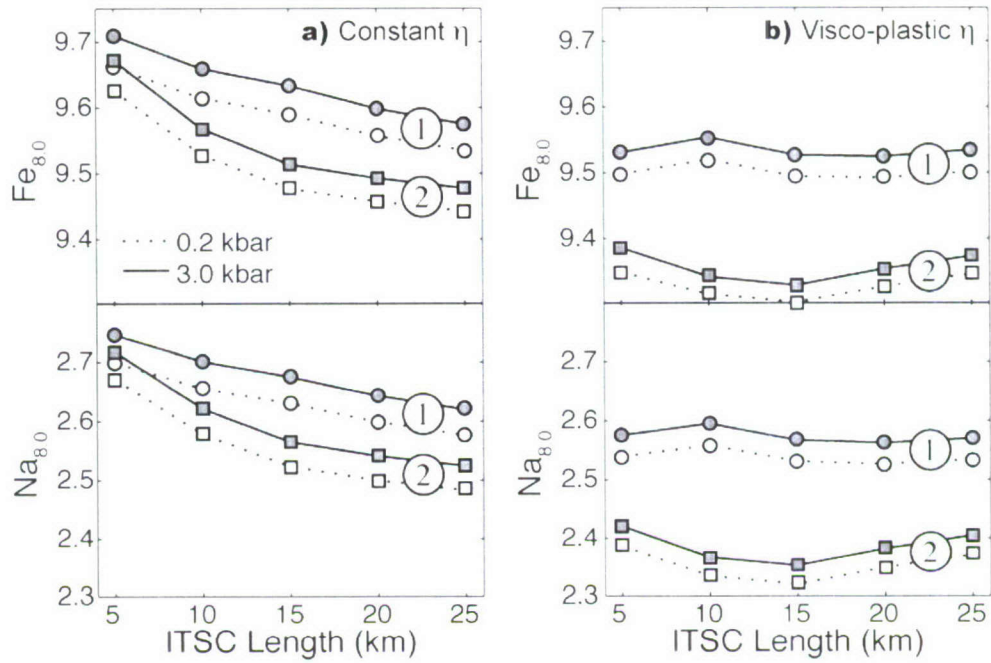


**Figure 9:** Calculated  $Fe_{8.0}$  and  $Na_{8.0}$  as a function  $L_{ITSC}$  for (a) constant viscosity rheology and (b) visco-plastic rheology. Model 1 is for wide melt pooling region, while Model 2 is for narrow melt pooling region. Gray circles on solid lines indicate calculations for fractional crystallization at 3.0 kbar. Open circles on dotted lines indicate calculations for fractional crystallization at 0.2 kbar. Each symbol represents the result of a single model run.  $T_p = 1350^\circ\text{C}$  and  $Nu = 4$ .



relatively insensitive to the length of the ITSC. This indicates that the compositional signature of the transform fault is sensitive to mantle rheology. Specifically, while models with a constant viscosity rheology predict a transform fault effect on ITSC lava chemistry, models with a visco-plastic rheology do not.

#### **4. APPLICATIONS TO THE SIQUEIROS TRANSFORM FAULT SYSTEM**

##### *4.1 Tectonic Setting*

The Siqueiros transform fault (Figure 1b) has been the site of several investigations including rock dredging and Alvin dives [Perfit *et al.*, 1996], magnetic [Carbotte and Macdonald, 1992] and gravity [Gregg *et al.*, 2007] surveys, and detailed geologic mapping [Fornari *et al.*, 1989]. This wealth of data makes it an ideal location to investigate the effects of fault segmentation. The Siqueiros transform system is a ~140 km-long left-lateral offset located between 8° 20'N and 8° 30'N on the EPR. The half slip-rate of the transform system is ~ 55 mm/yr [DeMets *et al.*, 1990; 1994]. Bathymetry and side-scan sonar collected from Siqueiros reveal that the transform system is segmented into five fault strands separated by four ITSCs labeled A–D from west to east (Figure 10) [Fornari *et al.*, 1989]. The current, segmented geometry of Siqueiros transform is thought to be the result of several discrete periods of counterclockwise rotation in the spreading direction (~ 4–8°) over the past 3 m.y. [Pockalny *et al.*, 1997].

Residual mantle Bouguer gravity anomalies (RMBA) calculated along the Siqueiros transform fault system suggest a mass deficit within the transform fault domain [Gregg *et al.*, 2007]. Assuming that the entire gravity anomaly is due to crustal thickness variations the RMBA data indicate excess crustal thickness (as compared to a reference crust of 6 km) of up to 1.5 km associated with bathymetric high associated with ITSC D (Figure 2c). Excess crust is also associated with ITSCs B and C along the central portion of the transform fault, and in the inactive fracture zones on either side of the Siqueiros transform system [Gregg *et al.*, 2007]. Gravity analysis did not reveal excess crust at ITSC A.

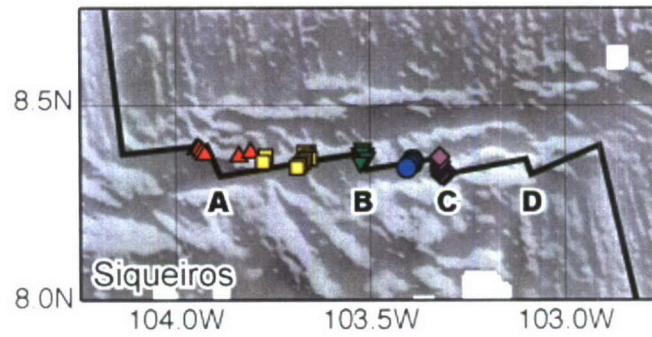


**Figure 10:** Shaded bathymetry for the Siqueiros Transform showing the locations of rock dredge and Alvin dive samples (colored symbols) collected along the transform fault [Hays, 2003]. The solid black line indicates the plate boundary, while the letters denote individual ITSCs.

We incorporate the geometry of Siqueiros transform system into a 3-D model to evaluate melting and melt migration beneath the fault zone. ITSCs A–D range in length from 10 km at ITSC A to < 5 km at ITSC D. Due to the obliquity of the ITSCs within the transform fault and the computational difficulty of the exact geometry, the orientations of each of the ITSCs have been squared off so that they are orthogonal to the transform fault strands and parallel to the adjacent ridge segments (Figure 11).

#### *4.2 Crustal Thickness Predictions at Siqueiros*

Model-predicted crustal thickness variations at the Siqueiros fault system are strongly dependent on mantle rheology (Figure 11a and b). The constant viscosity rheology predicts a cooler mantle beneath the transform system and, subsequently, lower extents of melting compared to the visco-plastic rheology (Figure 11a). Along the western portion of Siqueiros, the predicted crustal thickness variations due to the wide melt pooling (Model 1) match the gravity-derived crustal thicknesses calculated for ITSCs A and B (Figure 11c). However, the predicted crustal thickness diminishes to the east and does not match the observed gravity-derived crustal thicknesses at ITSCs C and D. Similar to the single ITSC models, segmentation geometry plays an important role in how the melt migrates into the transform fault. At ITSC A, the effect of the western ridge-transform intersection (RTI) results in a local minimum in the top of the melting region that is offset to the north of ITSC A. While we assume that these melts would be distributed along ITSC A, the offset suggests that this would not be a steady-state geometry. Because of the proximity of ITSC D to the eastern RTI and its relatively short length (~ 5km), ITSC D does not induce a local minimum in the top of the melting region. Therefore, melt produced near ITSC D is predicted to migrate to the eastern RTI and, thus, will not contribute to crustal accretion at ITSC D (Figure 11c).

The key difference between the visco-plastic and constant viscosity models is that the visco-plastic rheology predicts a warmer shallow mantle beneath the transform fault domain and higher overall extents of melting. The warmer temperature structure causes



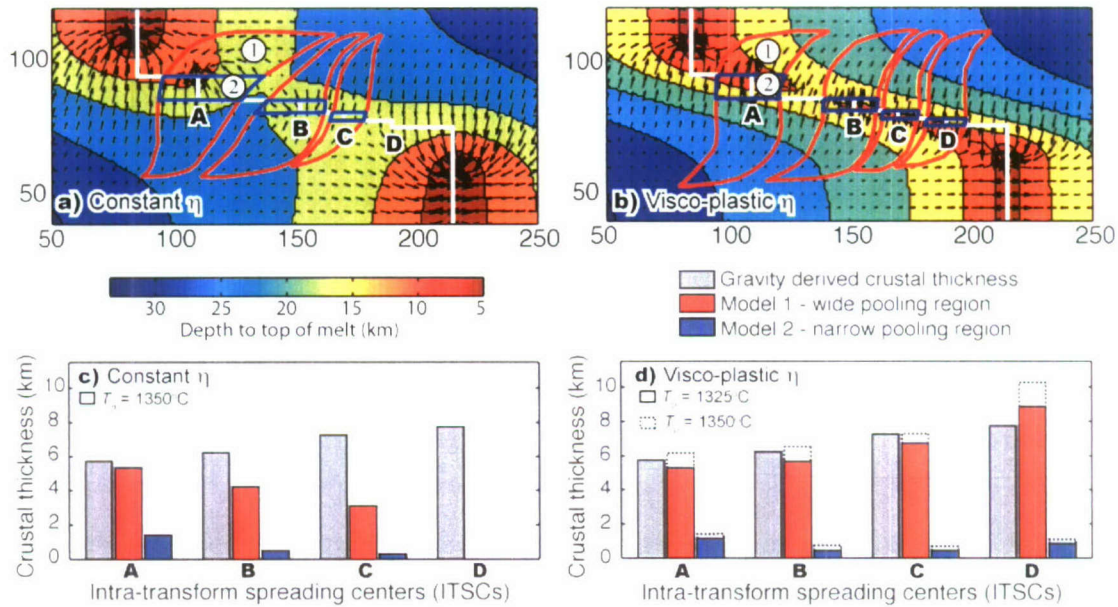


**Figure 11:** Results from the Siqueiros Transform melting models. (a) Depth to the top of melting calculated for a ridge-transform-ridge system with the geometry of Siqueiros and a constant viscosity rheology. Arrows indicate the local spatial derivative of the melt surface that is assumed to be the melt migration direction. Red solid line indicates wide melt pooling regions (Model 1). Blue solid lines indicate the narrow melt pooling regions (Model 2), which assumes that melt does not migrate across the transform fault. (b) The depth to the top of the melt surface for the visco-plastic rheology case. (c) Calculated and estimated crustal thickness values for the constant viscosity model.  $T_p = 1350^\circ\text{C}$  and  $\text{Nu} = 4$ . Gray bars show the gravity-derived crustal thicknesses at the Siqueiros transform fault from Gregg *et al.* [2007]. Red bars indicate the predicted crustal thickness for the wide pooling region model. Blue bars indicate the predicted crustal thicknesses for the narrow pooling region model. Note that no crustal accretion is predicted at spreading center D, as it is not a local minimum in the melt surface. (d) Crustal thickness predictions for the visco-plastic rheology model.  $T_p = 1325^\circ\text{C}$  and  $\text{Nu} = 4$ . Note that this model does a much better job of predicting the crustal thicknesses as observed from the gravity calculations. Crustal thickness predictions for  $T_p = 1350^\circ\text{C}$  are indicated by the dotted lines.

each ITSC to produce a local minimum in the top of the melting region and therefore enhances crustal accretion at each ITSC (Figure 11b). For  $T_p = 1325^\circ\text{C}$  the predicted crustal thickness for the wide pooling model (Model 1) generates a good fit to the gravity-derived crustal thickness data at all 4 ITSCs. Varying  $T_p$  from  $1325^\circ\text{C}$  to  $1350^\circ\text{C}$  (dotted bars in Figure 11d) results in predicted crustal thickness values that are approximately the same as those derived from gravity at ITSCs A, B, and C, but over-predicts the crustal thickness produced at ITSC D. Finally, the crustal thickness values predicted using narrow melt pooling (Model 2) for both the constant and visco-plastic rheologies are significantly smaller than those derived from the RMBA data, indicating that a wide melt pooling region is necessary to produce the crustal thickness variations calculated from the gravity anomaly.

#### 4.3 Geochemical Predictions at Siqueiros

We utilize major element analyses of the glassy chill margins from fresh basalts collected via dredge and Alvin dive along the Siqueiros fault system (Figure 10) [Perfit *et al.*, 1996; Hays, 2004]. Using the isobaric fractional crystallization model of Yang *et al.* [1996], the predicted liquid lines of descent (LLD) are compared to the observed major element composition of the Siqueiros transform lavas. Fractional crystallization pressure is fixed by the depth where melting ceases (solid lines in Figures 12 and 13) or at 0.2 kbars for the average seafloor depth (dashed lines in Figures 12 and 13).

In general, the visco-plastic rheology with wide pooling and  $T_p = 1350^\circ\text{C}$  does the best job of fitting the majority of the data (Figures 12 and 13). Both the constant and visco-plastic rheology models compare favorably to the observed FeO composition and there is very little difference between the wide and narrow pooling models. The warmer temperatures resulting from the visco-plastic rheology model produce lower FeO implying lower pressures of mantle melting compared to the constant viscosity rheology



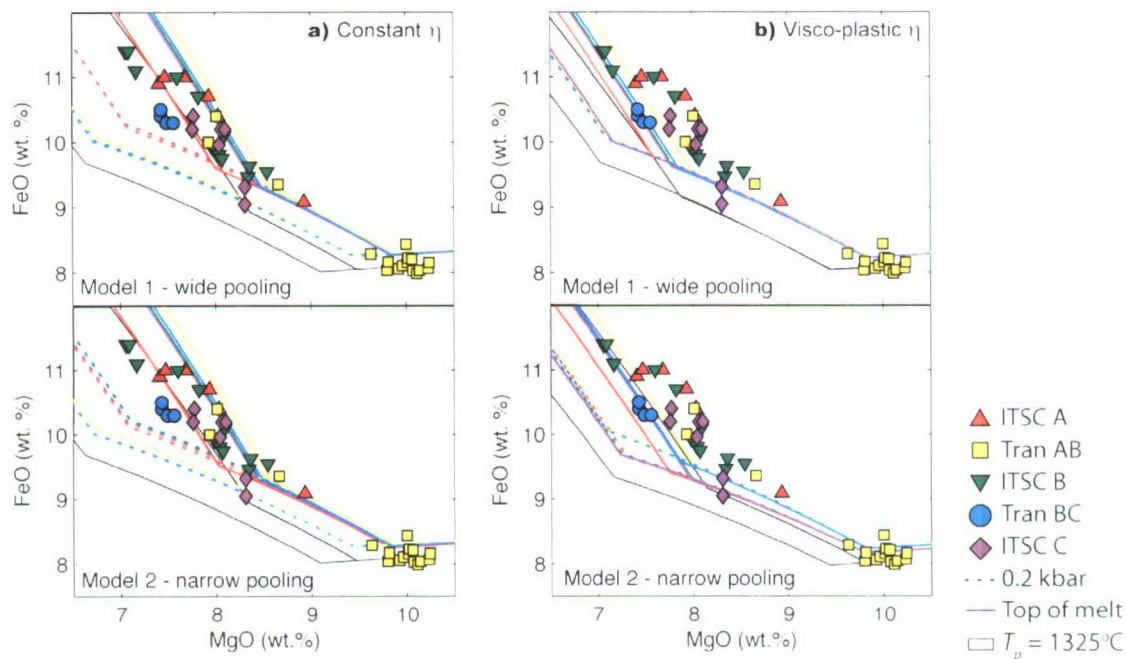


**Figure 12.** Liquid lines of descent (LLD) model calculations of FeO vs. MgO. Colored LLD in each panel correspond to the color of the data point for each ITSC or transform fault strand as shown in the legend on the lower right and in Figure 10. Solid LLD lines indicate fractional crystallization at the top of the melt surface, which ranges in depth from 18–24 km (6–8 kbars) for constant viscosity and 9–15.5 km (3–5 kbars) for visco-plastic rheology, while dashed LLD lines indicate fractional crystallization at 0.2 kbar which would be expected for fractional crystallization in a shallow magma lens. All models were run for  $T_p = 1350^\circ\text{C}$  and  $Nu = 4$ . The gray shaded regions indicate the predicted model region for  $T_p = 1325^\circ\text{C}$ . Models were run for (a) constant viscosity rheology and (b) variable rheology models and for a wide melt pooling region (top panels) and a narrow melt pooling region (bottom panels).



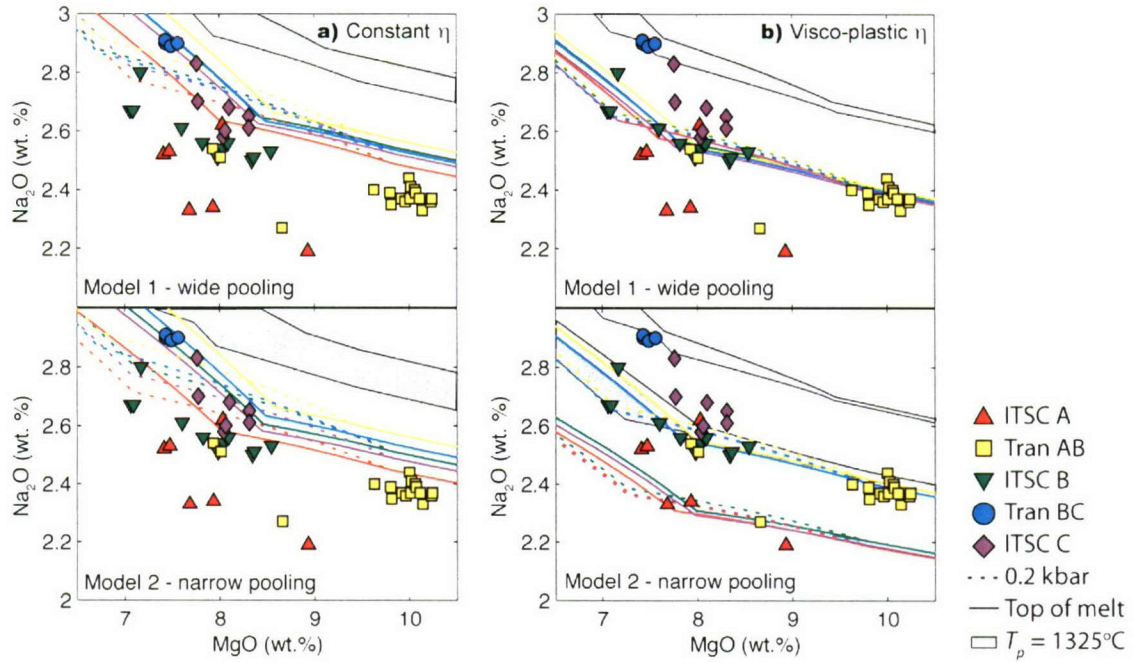


**Figure 13.** Liquid lines of decent (LLD) model calculations of  $\text{Na}_2\text{O}$  vs.  $\text{MgO}$ . Colored LLD in each panel correspond to color of the data point for each ITSC or transform fault strand as shown in the legend on the lower right and in Figure 10. Solid LLD lines indicate fractional crystallization at the top of the melt surface, which ranges in depth from 18–24 km (6–8 kbars) for constant viscosity and 9–15.5 km (3–5 kbars) for visco-plastic rheology, while dashed LLD lines indicate fractional crystallization at 0.2 kbar which would be expected for fractional crystallization in a shallow magma lens. All models were run for  $T_p = 1350^\circ\text{C}$  and  $\text{Nu} = 4$ . The gray shaded regions indicate the model region for  $T_p = 1325^\circ\text{C}$ . Models were run for (a) constant viscosity and (b) visco-plastic rheology models for a wide melt pooling region (top panels) and a narrow melt pooling region (bottom panels).

(Figures 12a, b). Fractional crystallization at the depth of melt termination, 18–20 km and 9–15.5 km for the constant and visco-plastic rheologies respectively (solid LLD in Figures 12 and 13), fits the data much better than fractional crystallization at shallower depths (dashed LLD in Figures 12 and 13). The discrepancy between the Siqueiros FeO data and the visco-plastic rheology predicted LLD may indicate that crystallization is polybaric and a mixture of melts fractionally crystallized at various depths (Figure 12b). Incorporating a lower  $T_p$  of 1325°C results in shallower melting with lower FeO and higher Na<sub>2</sub>O predictions that do not agree as well with the Siqueiros data for either mantle rheology. The constant viscosity model under-predicts the extent of melting, i.e., Na<sub>2</sub>O values that are too high, for both wide and narrow pooling (Figure 13a). This is consistent with the under-prediction of crustal thickness using the constant viscosity model.

The predicted trends in Fe<sub>8.0</sub> and Na<sub>8.0</sub> for the Siqueiros transform system are very similar to those predicted by the generic ridge-transform-ridge models (Figures 9a, b). As the ITSCs decrease in length from west to east along the Siqueiros transform fault, the visco-plastic rheology predicts little to no variation in the Fe<sub>8.0</sub> and Na<sub>8.0</sub> (Figure 14b). On the contrary, the constant viscosity rheology predicts that both Fe<sub>8.0</sub> and Na<sub>8.0</sub> will increase indicating that the extent of melting decreases and the depth of melting increases. The observed range in Na<sub>8.0</sub> (shown by the error bars in Figure 14) appears to increase slightly along the transform fault in agreement with the model predictions, but Fe<sub>8.0</sub> decreases slightly from west to east along the transform fault system. Both rheological models intersect the range of Fe<sub>8.0</sub> and Na<sub>8.0</sub> observed at all of the ITSCs and fault strand AB, but do not do a very good job of predicting the values observed at fault strand BC.

## 5. DISCUSSION

### 5.1 *Factors controlling crustal thickness variations*

Melt migration beneath mid-ocean ridge spreading centers is poorly constrained.

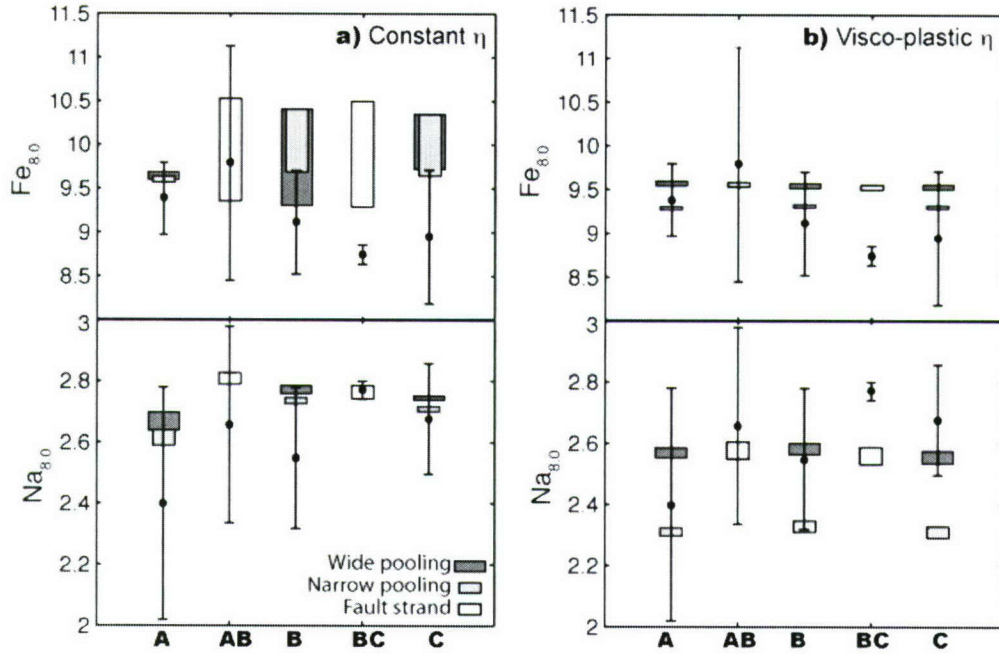


**Figure 14:**  $Fe_{8.0}$  and  $Na_{8.0}$  predictions for each of the ITSCs and their connecting fault segments at the Siqueiros Transform. Mean data values are indicated by solid dots [Hays, 2004], while error bars indicate the total spread observed in the data. Dark gray boxes indicate predictions for a wide melt pooling region and fractional crystallization from 0.2 kbar to the top of the melting region (~6–8 kbar for constant viscosity and 3–5 kbar for visco-plastic rheology). Light gray shaded boxes indicate the predictions for a narrow melt pooling region and fractional crystallization from 0.2 kbar to the top of the melting region (~6–8 kbar for constant viscosity and 3–5 kbar for visco-plastic rheology). Open boxes show the predictions for melts migrated to the transform fault strands AB and BC.



In 2-D ridge models, the predicted crustal thickness variations are sensitive to  $W_{pool}$  and  $T_p$ . For example, for  $U_0 = 50$  mm/yr,  $W_{pool} = 75$  km, and  $T_p = 1350^\circ\text{C}$ , the KG92 melt model predicts a crustal thickness of 6–7 km, while the K03 and RJ81 melting models predict thicker crust on the order of 8–10 km. Therefore, to match the crustal thickness variations observed at the EPR  $9^\circ\text{N}$  segment, the RJ81 and K03 models require the migration of melt over shorter distances to the ridge axis or lower values for  $T_p$ .

A similar relationship is observed in 3-D at ITSCs within a transform fault system. Previous studies have assumed that melts extruded at ITSCs came from directly below the transform fault domain or from the nearby ridge axis, and have discussed the possibility that melts may be drawn in across the transform fault from large regions of the surrounding mantle [Fornari *et al.*, 1989; Hekinian *et al.*, 1992; Hekinian *et al.*, 1995; Perfit *et al.*, 1996; Wendt *et al.*, 1999]. If we assume that the negative RMBA observed along the Siqueiros fault system is due to crustal thickness variations, melts must somehow focus into the transform fault from large regions of the mantle. The wide melt pooling model for the Siqueiros transform predicts that melts must travel, on average,  $\sim 40$  km to reach an ITSC. This is approximately half the distance that was required for melts to migrate (75 km) in order to match the EPR  $9^\circ\text{N}$  data in our 2-D melting models. However, since there are fresh lava flows observed along the fault strands separating the ITSCs, it is clear that some of the melt does not make it to the spreading segments [Perfit *et al.*, 1996]. Overall, we conclude that to generate enhanced crustal thickness within fast-slipping transform systems, melt must migrate into the transform domain from a wide region of underlying mantle.

RMBA derived crustal thickness variations [Gregg, *et al.*, 2007] at the Garrett transform fault also suggest that melt must come from a wide region of the mantle. However, the melt generated in the mantle surrounding the Garrett transform does not appear to migrate directly into the transform fault and aggregate at the ITSCs. The Garrett transform is  $\sim 130$  km-long with three ITSCs containing four ridges  $\sim 9$  km-long that lie in between four fault strands [Hekinian *et al.*, 1992]. Peridotites collected from

the Garrett transform are very depleted, indicating high degrees of melting in the mantle regions surrounding the fault system [Niu and Hekinian, 1997a; Niu and Hekinian, 1997b; Constantin, 1999]. However, the majority of the excess crust observed at the Garrett system is associated with the flanking topography correlating to the transform fault and fracture zones and not with the ITSCs within the transform domain. The Garrett ITSCs appear to correspond to regions of modest crustal thicknesses equal to or less than the adjacent ridge segments [Gregg *et al.*, 2007]. These observations suggest that the melts pooled from a wide mantle region surrounding the Garrett system are extruded on the flanks of the transform fault where more permeable pathways may have been produced by brittle deformation.

## 5.2 The Siqueiros Transform Effect on Mantle Melting

The geochemical transform fault effect suggests that the cooler mantle region surrounding the transform fault system will promote deeper and lower extents of melting [Bender *et al.*, 1978; Bender *et al.*, 1984; Langmuir and Bender, 1984; Langmuir *et al.*, 1986; Reynolds *et al.*, 1992; Reynolds and Langmuir, 1997]. However, previous studies have illustrated considerable overlap in the observed composition of lavas collected along the EPR 9°N segment and the Siqueiros transform fault system [Perfit *et al.*, 1996; Hays, 2004] and only modest along-segment variation in the composition of lavas from the 9°N ridge segment approaching the Siqueiros transform fault [Langmuir *et al.*, 1986]. Furthermore, the investigation of U-series disequilibria in basalts collected at the Siqueiros transform fault suggests that the upwelling and melting rates beneath the transform fault are very similar to those observed in samples from 9°30' N on the EPR [Lundstrom *et al.*, 1999].

The incorporation of the visco-plastic mantle rheology into the thermal models for a transform fault creates a warmer thermal structure beneath the transform fault domain. This viscosity effect coupled with a segmented transform fault geometry results in melting processes at ITSCs that mimic the processes occurring at nearby ridge segments, and predicts extents of melting and lava composition at the ITSCs that are comparable to



those observed at a steady-state ridge segment. Therefore, not only does the visco-plastic rheology model match the geophysical and geochemical observations at Siqueiros, this rheology does a very good job of explaining why the ITSCs of Siqueiros are producing EPR-like lavas.

### 5.3 High-pressure Fractional Crystallization

While high pressure fractional crystallization has been proposed by *Michael and Cornell* [1998] to explain compositional variability at slow-spreading ridges with low magma flux, *Langmuir et al.* [1992] maintain that there are many problems associated with this mechanism. The primary argument of *Langmuir et al.* [1992] is that in a ridge setting the lithosphere must be sufficiently thick to shut melting off at depth and that high-pressure crystallization must be consistent with melting processes. By combining fractional melting and crystallization models with mantle thermal models we are able to quantify both the termination of melting and the onset of crystallization. At the 9°N segment of the EPR our predicted fractional crystallization depth range of ~ 0–3 km (0.2–1.0 kbar) matches major element composition observations [*Batiza and Niu*, 1992] and crustal thickness variations [*Canales et al.*, 2003], as well as previous estimations for shallow crystallization beneath the EPR ridge axis [e.g., *Michael and Cornell*, 1998]. On the other hand, we find that models of fractional crystallization at much greater depths, 9–18 km (3–6 kbars), fit the observed variations in composition at the Siqueiros transform fault ITSCs [*Perfit et al.*, 1996; *Hays*, 2004]. In fact, models of shallow crystallization do a very poor job of predicting the observed major element variations at the Siqueiros transform fault. Specifically, if shallow-level fractional crystallization were occurring we would expect the observed compositions to fall upon the 0.2 kbar line in Figures 12 and 13. Since our models take into account the full melting process and begin crystallization at depths above melt termination, they are self-consistent given the physical constraints of melting and crystallization processes.



#### 5.4 Melt Extraction at Siqueiros Transform Fault

The observed major and trace element data from the Siqueiros transform system vary widely from enriched mid-ocean ridge basalt (EMORB) to depleted mid-ocean ridge basalt (DMORB). However, lavas from a single tectonic region within Siqueiros are relatively homogenous (e.g., Figure 13) [Perfit *et al.*, 1996; Hays *et al.*, 2004]. These findings have led previous researchers to suggest that there are multiple mantle sources beneath the transform fault and that each ITSC and fault strand is independent of its neighbor and taps a different melt lens and/or mantle supply [Fornari *et al.*, 1989; Perfit *et al.*, 1996; Hays, 2004]. Fornari *et al.* [1989] proposed that the variations in the observed lava chemistry result from melt accumulation at different depths due to the complex thermal structure of Siqueiros. The range of normal MORB compositions found in the lavas collected from the ITSCs suggest the existence of a frequently replenished melt lens beneath each ITSC [Perfit *et al.*, 1996]. Perfit *et al.* [1996] further suggested that the primitive lavas collected from fault strand AB might be the result of tapping into the unmixed, undifferentiated lower levels of a magma chamber, possibly from one of the adjacent ITSCs. All of these previous studies suggest that the three-dimensional magmatic regime beneath Siqueiros is convoluted, and are unclear as to how each ITSC is supplied from the mantle.

Until now, the process of melt feeding into the transform fault domain has been thought of as fairly two-dimensional in that the supply of melt must either come from directly below the transform fault or from the nearby ridge axis. Our 3-D thermal and melt models for Siqueiros indicate that melt present in the mantle regions flanking the transform fault should also supply the ITSCs. By using classic melt migration techniques [e.g., Sparks and Parmentier, 1990] that pool melts from a large region of the mantle and fractionally crystallizing them at the depth of melt termination, we can reproduce the same range of major element lava composition that is observed (Figures 12b, and 13b). The results of our models indicate that melts extracted at Siqueiros are aggregated from a wide region of the mantle and experience fractional crystallization at depths ranging from ~ 9–18 km. This suggests that the variations in the geochemistry of lavas from Siqueiros

transform fault can be explained by the complexities of migrating melt into the transform fault, and do not require (nor preclude) multiple sources beneath Siqueiros.

## 6. CONCLUSIONS

Our investigation of melt extraction at segmented oceanic transform faults illustrates that melt migration into the transform fault domain is a fully three-dimensional process that incorporates melts from a wide region of the mantle surrounding the transform fault. Assuming that melt is migrated into the transform fault domain from a large mantle region, we find that crustal production is enhanced at ITSCs by 2.5 km for models incorporating an isoviscous rheology and up to 3–6.5 km for visco-plastic rheology models. These model predictions may explain the systematic excess crustal thickness observed at intermediate and fast-slipping transform faults [Gregg *et al.*, 2007]. Specifically, to match the gravity-derived crustal thickness variations observed within the Siqueiros transform fault ( $> 1.5$  km), melt must aggregate from a wide pooling area. Finally, utilizing a visco-plastic rheology, with  $T_p = 1350^\circ\text{C}$ , in conjunction with the fractional melting model of Kinzler and Grove [1992a, b; 1993] and the fractional crystallization model of Yang *et al.* [1996], we demonstrate that the observed variations in major element composition from the Siqueiros transform fault can be explained by pooling melts from a wide region of the mantle and fractionally crystallizing them at the depth of melt termination,  $\sim 9$ –18 km.

## 7. ACKNOWLEDGEMENTS

We are grateful for helpful discussions with D. Forsyth, M. Jackson, M. Krawczynski, S. Hart, E. Roland, H. Schouten, Z. Wang, and the WHOI Geochemistry and Geophysics groups. We also thank H. Yang, and R. Kinzler for use of their original FORTRAN codes for developing our models.



## 8. REFERENCES

- Asimow, P. D., and C. H. Langmuir (2003), The importance of water to oceanic mantle melting regimes, *Nature*, *421*, 815-820.
- Baker, E. T., Y. J. Chen, and J. Phipps Morgan (1996), The relationship between near-axis hydrothermal cooling and the spreading rate of mid-ocean ridges, *Earth Planet. Sci. Lett.*, *142*, 137-145.
- Batiza, R., and Y. L. Niu (1992), Petrology and magma chamber processes at the East Pacific Rise similar to 9°30'N, *J. Geophys. Res.*, *97*, 6779-6797.
- Behn, M. D., M. S. Boettcher, and G. Hirth (2007), Thermal structure of oceanic transform faults, *Geology*, *35*, 307-310.
- Bender, J. F., F. N. Hodges, and A. E. Bence (1978), Petrogenesis of basalts from project Famous Area - Experimental-study from 0-kbar to 15-kbars, *Earth Planet. Sci. Lett.*, *41*, 277-302.
- Bender, J. F., C. H. Langmuir, and G. N. Hanson (1984), Petrogenesis of Basalt Glasses from the Tamayo Region, East Pacific Rise, *J. Petrol.*, *25*, 213-254.
- Canales, J. P., R. S. Detrick, J. Lin, J. A. Collins, and D. R. Toomey (2000), Crustal and upper mantle seismic structure beneath the rift mountains and across a nontransform offset at the Mid-Atlantic Ridge (35 degrees N), *J. Geophys. Res.*, *105*, 2699-2719.
- Canales, J. P., R. Detrick, D. R. Toomey, and S. D. Wilcock (2003), Segment-scale variations in the crustal structure of 150-300 kyr old fast spreading oceanic crust (East Pacific Rise, 8°15'N-10°5'N) from wide-angle seismic refraction profiles, *Geophys. J. Int.*, *152*, 766-794.
- Carbotte, S., and K. Macdonald (1992), East Pacific Rise 8° - 10° 30'N - Evolution of ridge segments and discontinuities from Seamarc II and 3-dimensional magnetic studies, *J. Geophys. Res.*, *97*, 6959-6982.
- Chen, Y. S., and W. J. Morgan (1990), A nonlinear rheology model for midocean ridge axis



- topography, *J. Geophys. Res.*, *95*, 17583-17604.
- Constantin, M. (1999), Gabbroic intrusions and magmatic metasomatism in harzburgites from the Garrett transform fault: implications for the nature of the mantle-crust transition at fast-spreading ridges, *Cont. Min. Pet.*, *136*, 111-130.
- DeMets, C., R. G. Gordon, D. F. Argus, and S. Stein (1990), Current plate motions, *Geophys. J. Int.*, *101*, 425-478.
- DeMets, C., R. G. Gordon, D. F. Argus, and S. Stein (1994), Effect of recent revisions to the geomagnetic reversal time-scale on estimates of current plate motions, *Geophys. Res. Lett.*, *21*, 2191-2194.
- Detrick, R. S., H. D. Needham, and V. Renard (1995), Gravity-anomalies and crustal thickness variations along the Mid-Atlantic Ridge between 33°N and 40°N, *J. Geophys. Res.*, *100*, 3767-3787.
- Escartin, J., and J. Lin (1995), Ridge offsets, normal faulting, and gravity anomalies of slow spreading ridges, *J. Geophys. Res.*, *100*, 6163-6177.
- Fornari, D. J., D. G. Gallo, M. H. Edwards, J. A. Madsen, M. R. Perfit, and A. N. Shor (1989), Structure and topography of the Siqueiros transform-fault system - Evidence for the development of intra-transform spreading centers, *Mar. Geophys. Res.*, *11*, 263-299.
- Forsyth, D. W. (1993), Crustal thickness and the average depth and degree of melting in fractional melting models of passive flow beneath mid-ocean ridges, *J. Geophys. Res.*, *98*, 16073-16079.
- Fox, P. J., and D. G. Gallo (1984), A tectonic model for ridge-transform-ridge plate boundaries: Implications for the structure of oceanic lithosphere, *Tectonophysics*, *104*, 205-242.
- Gregg, P. M., J. Lin, M. D. Behn, and L. G. J. Montesi (2007), Spreading rate dependence of gravity anomalies along oceanic transform faults, *Nature*, *448*, 183-187.
- Grove, T. L., R. J. Kinzler, and W. B. Bryan (1992), Fractionation of mid-ocean ridge

- basalt, in *Mantle Flow and Melt Generation at Mid-Ocean Ridges*, edited by J. Phipps Morgan, et al., pp. 281-310, American Geophysical Union, Washington D.C.
- Hays, M. R. (2004), Intra-Transform Volcanism Along the Siqueiros Fracture Zone 8°20' N - 8°30' N, East Pacific Rise, 251 pp, University of Florida, Gainesville.
- Hays, M. R., M. R. Perfit, D. J. Fornari, and W. Ridley (2004), Magmatism in the Siqueiros transform: Major and trace element evidence for mixing and multiple sources, *Eos Trans. AGU*, 85, Fall Meet. Suppl., Abstract T41A-1165.
- Hekinian, R., D. Bideau, M. Cannat, J. Francheteau, and R. Hebert (1992), Volcanic activity and crust mantle exposure in the ultrafast Garrett transform-fault near 13°28'S in the Pacific, *Earth Planet. Sci. Lett.*, 108, 259-275.
- Hekinian, R., D. Bideau, R. Hebert, and Y. L. Niu (1995), Magmatism in the Garrett transform-fault (East Pacific Rise near 13° 27'S), *J. Geophys. Res.*, 100, 10163-10185.
- Hooft, E. E. E., R. S. Detrick, D. R. Toomey, J. A. Collins, and J. Lin (2000), Crustal thickness and structure along three contrasting spreading segments of the Mid-Atlantic Ridge, 33.5°-35°N, *J. Geophys. Res.*, 105, 8205-8226.
- Katz, R. F., M. Spiegelman, and C. H. Langmuir (2003), A new parameterization of hydrous mantle melting, *Geochem. Geophys. Geosyst.*, 4, 19.
- Kinzler, R. J., and T. L. Grove (1992a), Primary magmas of midocean ridge basalts 2. Applications, *J. Geophys. Res.*, 97, 6907-6926.
- Kinzler, R. J., and T. L. Grove (1992b), Primary magmas of midocean ridge basalts 1. Experiments and methods, *J. Geophys. Res.*, 97, 6885-6906.
- Kinzler, R. J., and T. L. Grove (1993), Corrections and further discussion of the primary magmas of midocean ridge basalts, 1 and 2, *J. Geophys. Res.*, 98, 22339-22347.
- Klein, E. M., and C. H. Langmuir (1987), Global correlations of ocean ridge basalt chemistry with axial depth and crustal thickness, *J. Geophys. Res.*, 92, 8089-8115.
- Kuo, B. Y., and D. W. Forsyth (1988), Gravity anomalies of the ridge transform intersection system in the South Atlantic between 31 and 34.5°S: Upwelling centers

- and variations in crustal thickness, *Mar. Geophys. Res.*, *10*, 205-232.
- Langmuir, C. H., and J. F. Bender (1984), The Geochemistry of oceanic basalts in the vicinity of transform faults - Observations and implications, *Earth Planet. Sci. Lett.*, *69*, 107-127.
- Langmuir, C. H., J. F. Bender, and R. Batiza (1986), Petrological and tectonic segmentation of the East Pacific Rise, 5° 30' – 14° 30'N, *Nature*, *322*, 422-429.
- Langmuir, C. H., E. M. Klein, and T. Plank (1992), Petrological systematics of mid-ocean ridge basalts: Constraints on melt generation beneath ocean ridges, in *Mantle Flow and Melt Generation at Mid-Ocean Ridges*, edited by J. Phipps Morgan, et al., pp. 183-280, American Geophysical Union, Washington D.C.
- Lin, J., G. M. Purdy, H. Schouten, J.-C. Sempere, and C. Zervas (1990), Evidence from gravity data for focused magmatic accretion along the Mid-Atlantic Ridge, *Nature*, *344*, 627-632.
- Lin, J., and J. Phipps Morgan (1992), The spreading rate dependence of three-dimensional mid-ocean ridge gravity structure, *Geophys. Res. Lett.*, *19*, 13-16.
- Lundstrom, C. C., D. E. Sampson, M. R. Perfit, J. Gill, and Q. Williams (1999), Insights into mid-ocean ridge basalt petrogenesis: U-series disequilibria from the Siqueiros Transform, Lamont Seamounts, and East Pacific Rise, *J. Geophys. Res.*, *104*, 13,035-013,048.
- MacLennan, J., T. Hulme, and S. C. Singh (2005), Cooling of the lower oceanic crust, *Geology*, *33*, 357-360.
- Magde, L. S., and D. W. Sparks (1997), Three-dimensional mantle upwelling, melt generation, and melt migration beneath segment slow spreading ridges, *J. Geophys. Res.*, *102*, 20571-20583.
- Magde, L. S., D. W. Sparks, and R. S. Detrick (1997), The relationship between buoyant mantle flow, melt migration, and gravity bull's eyes at the Mid-Atlantic Ridge between 33°N and 35°N, *Earth Planet. Sci. Lett.*, *148*, 59-67.



- Menard, H. W., and R. L. Fisher (1958), Clipperton fracture zone in the northeastern equatorial Pacific, *Journal of Geology*, *66*, 239-253.
- Menard, H. W. (1967), Extension of northeastern-Pacific fracture zones, *Science*, *155*, 72-74.
- Menard, H. W., and T. Atwater (1969), Origin of fracture zone topography, *Nature*, *222*, 1037-1040.
- Michael, P. J., and W. C. Cornell (1998), Influence of spreading rate and magma supply on crystallization and assimilation beneath mid-ocean ridges: Evidence from chlorine and major element chemistry of mid-ocean ridge basalts, *J. Geophys. Res.*, *103*, 18325-18356.
- Nagle, A. N., R. C. Pickle, A. E. Saal, E. H. Hauri, and D. W. Forsyth (2007), Volatiles in basalts from intra-transform spreading centers: Implications for melt migration models, *Eos Trans. AGU*, *88*, Fall Meet. Suppl., Abstract DI43A-05.
- Niu, Y., and R. Hekinian (1997a), Spreading-rate dependence of the extent of mantle melting beneath ocean ridges, *Nature*, *385*, 326-329.
- Niu, Y. L., and R. Hekinian (1997b), Basaltic liquids and harzburgitic residues in the Garrett Transform: A case study at fast-spreading ridges, *Earth Planet. Sci. Lett.*, *146*, 243-258.
- Parmentier, E. M., and D. W. Forsyth (1985), 3-Dimensional flow beneath a slow spreading ridge axis - A dynamic contribution to the deepening of the median valley toward fracture-zones, *90*, 678-684.
- Perfit, M. R., D. J. Fornari, W. I. Ridley, P. D. Kirk, J. Casey, K. A. Kastens, J. R. Reynolds, M. Edwards, D. Desonie, R. Shuster, and S. Paradis (1996), Recent volcanism in the Siqueiros transform fault: Picritic basalts and implications for MORB magma genesis, *Earth Planet. Sci. Lett.*, *141*, 91-108.
- Phipps Morgan, J., E. M. Parmentier, and J. Lin (1987), Mechanisms for the origin of midocean ridge axial topography - Implications for the thermal and mechanical

- structure of accreting plate boundaries, *J. Geophys. Res.*, *92*, 12823-12836.
- Phipps Morgan, J., and D. W. Forsyth (1988), 3-Dimensional flow and temperature perturbations due to a transform offset - Effects on oceanic crustal and upper mantle structure, *J. Geophys. Res.*, *93*, 2955-2966.
- Phipps Morgan, J., and Y. J. Chen (1993), The genesis of oceanic-crust - Magma injection, hydrothermal circulation, and crustal flow, *J. Geophys. Res.*, *98*, 6283-6297.
- Pockalny, R. A. (1997), Evidence of transpression along the Clipperton Transform: Implications for processes of plate boundary reorganization, *146*, 449-464.
- Pockalny, R. A., P. J. Fox, D. J. Fornari, K. C. Macdonald, and M. R. Perfit (1997), Tectonic reconstruction of the Clipperton and Siqueiros Fracture Zones: Evidence and consequences of plate motion change for the last 3 Myr, *J. Geophys. Res.*, *102*, 3167-3181.
- Reid, I., and H. R. Jackson (1981), Oceanic spreading rate and crustal thickness, *Mar. Geophys. Res.*, *5*, 165-172.
- Reynolds, J. R., C. H. Langmuir, J. F. Bender, K. A. Kastens, and W. B. F. Ryan (1992), Spatial and temporal variability in the geochemistry of basalts from the East Pacific Rise, *Nature*, *359*, 493-499.
- Reynolds, J. R., and C. H. Langmuir (1997), Petrological systematics of the Mid-Atlantic Ridge south of Kane: Implications for ocean crust formation, *J. Geophys. Res.*, *102*, 14915-14946.
- Searle, R. C. (1983), Multiple, closely spaced transform faults in fast-slipping fracture-zones, *Geology*, *11*, 607-610.
- Sparks, D. W., and E. M. Parmentier (1991), Melt extraction from the mantle beneath spreading centers, *Earth and Planet. Sci. Lett.*, *105*, 368-377.
- Sparks, D. W., E. M. Parmentier, and J. Phipps Morgan (1993), 3-dimensional mantle convection beneath a segmented spreading center - Implications for along-axis variations in crustal thickness and gravity, *J. Geophys. Res.*, *98*, 21977-21995.

- Tolstoy, M., A. Harding, and J. Orcutt (1993), Crustal thickness on the Mid-Atlantic Ridge: Bulls-eye gravity anomalies and focused accretion, *Science*, 262, 726-729.
- Turcotte, D. L. (1982), Magma migration, *Annu. Rev. Earth Planet. Sci.*, 10, 397-408.
- Wendt, J. I., M. Regelous, Y. L. Niu, R. Hekinian, and K. D. Collerson (1999), Geochemistry of lavas from the Garrett Transform Fault: insights into mantle heterogeneity beneath the eastern Pacific, *Earth Planet. Sci. Lett.*, 173, 271-284.
- Workman, R. K., and S. R. Hart (2005), Major and trace element composition of the depleted MORB mantle (DMM), *Earth Planet. Sci. Lett.*, 231, 53-72.
- Yang, H. J., R. J. Kinzler, and T. L. Grove (1996), Experiments and models of anhydrous, basaltic olivine-plagioclase-augite saturated melts from 0.001 to 10 kbar, *Contrib. Mineral. Petrol.*, 124, 1-18.



## 9. TABLES

**Table 1.** Model parameters

| Parameter  |  | Value              |
|------------|--|--------------------|
| $A$        | Smoothing coefficient for hydrothermal cooling equation                        | 0.75               |
| $C_p$      | Specific heat capacity, $\text{J kg}^{-1} \text{ } ^\circ\text{K}^{-1}$        | $1.25 \times 10^3$ |
| $\eta_0$   | Reference maximum viscosity, Pa s  | $10^{23}$          |
| $k$        | Thermal diffusivity, $\text{m}^2 \text{ s}^{-1}$                               | $10^{-6}$          |
| $k_0$      | Reference thermal conductivity, $\text{W m}^{-1} \text{ } ^\circ\text{K}^{-1}$ | 3                  |
| $L$        | Latent heat of melting, $\text{J kg}^{-1}$                                     | 400                |
| $L_T$      | Transform fault length, km   | 100                |
| $L_{ITSC}$ | Intra-transform spreading center length, km                                    | 5 - 25             |
| $Nu$       | Nusselt number   | 1 - 8              |
| $Q$        | Activation energy, $\text{J mol}^{-1}$   | $250 \times 10^3$  |
| $\rho$     | Reference mantle density, $\text{kg m}^{-3}$                                   | 3300               |
| $R$        | Universal gas constant, $\text{J mol}^{-1} \text{ } ^\circ\text{K}^{-1}$       | 8.3114             |
| $T_c$      | Temperature at the surface of the thermal model, $^\circ\text{C}$              | 0                  |
| $T_{max}$  | Maximum temperature of hydrothermal fluid circulation, $^\circ\text{C}$        | 600                |
| $T_p$      | Mantle potential temperature used in melt models, $^\circ\text{C}$             | 1300 - 1400        |
| $U_0$      | Imposed spreading half-rate, $\text{mm yr}^{-1}$                               | 50                 |
| $W_{pool}$ | Horizontal length-scale for melt migration, km                                 | 75 - 200           |
| $z_{max}$  | Maximum depth of hydrothermal fluid circulation, km                            | 6                  |

**Table 2.** Variables

| Variable              |  |
|-----------------------|--|
| $C_0$                 | Initial oxide concentration  |
| $C_{i,m}$             | Concentration of oxide, i, in the melt   |
| $D_{i,s}$             | Bulk partition coefficient of oxide, i, in the initial solid                   |
| $\Delta t_c$          | Change in crustal thickness, km  |
| $\dot{\epsilon}_{II}$ | Second invariant of the strain rate tensor, $\text{s}^{-1}$                    |
| $F$                   | Melt fraction, %   |
| $F_{max}$             | Maximum melt fraction, %   |
| $\eta_{byr}$          | Brittle strength viscosity, Pa s   |
| $\eta_{td}$           | Temperature dependent viscosity, Pa s  |
| $\eta_{tot}$          | Total viscosity, Pa s  |
| $k$                   | Effective thermal conductivity, $\text{W m}^{-1} \text{ } ^\circ\text{K}^{-1}$ |
| $p$                   | Pressure of melting, kbars   |
| $p_r$                 | Lithostatic pressure, Pa   |
| $p_w$                 | Hydrostatic pressure, Pa   |
| $P_{i,m}$             | Bulk partition coefficient of oxide, i, in the melt                            |
| $S$                   | Maximum shear stress, Pa   |
| $T$                   | Temperature, $^\circ\text{C}$  |
| $T_s$                 | Solidus temperature, $^\circ\text{C}$  |
| $\mathbf{u}$          | Velocity field   |



## **APPENDIX: Seismicity characteristics of the equatorial East Pacific Rise and its offsets**

### **ABSTRACT**

We utilize hydroacoustic data collected from May 1996 to November 2001 by NOAA/PMEL's Equatorial Pacific autonomous underwater hydrophone (AUH) array to investigate the first order spatial and temporal variability of seismicity of the equatorial Pacific within the array and in particular, the East Pacific Rise (EPR). Our statistical analyses reveal strong evidence of seismic clustering along the EPR. The majority of earthquakes are clustered in seismic swarms in which individual events occurred within a few km and minutes or hours of each other. We examine the seismicity and segmentation characteristics of eight transform fault systems in our study area: Clipperton, Siqueiros, Quebrada, Discovery, Gofar, Yaquina, Wilkes, and Garrett transform faults. While the seismic moment release recorded in the CMT catalog over the past 30 years increases with increasing brittle area for each transform fault, the number of recorded AUH events does not appear to be correlated to brittle area. On the other hand, with the exception of Clipperton transform fault and the G3 segment of Gofar transform, the number of recorded AUH events increase with increasing transform segment length. More than 90% of the seismicity recorded on the ridge axis is associated with overlapping spreading centers (OSC). While many of these events can be attributed to tectonic activity on the OSC, there is also evidence for magmatically induced seismicity.



## TABLES

**Table 1.** First-order ridge segmentation within the study area

| Segment | North end |          | South end |          | Length, km | No. of seismic events |     |
|---------|-----------|----------|-----------|----------|------------|-----------------------|-----|
|         | Lat °N    | Lon °W   | Lat °N    | Lon °W   |            | AUH                   | CMT |
| 1       | 12.5      | -104.4   | 10.433    | -103.562 | 284.4      | 8                     | 0   |
| 2       | 10.04     | -104.33  | 8.45      | -104.208 | 177        | 49                    | 0   |
| 3       | 8.3       | -102.88  | 2.667     | -102.15  | 630.4      | 175                   | 0   |
| 4       | 1.167     | -102.15  | -3.7      | -102.6   | 542.5      | 142                   | 2   |
| 5       | -4.088    | -104.522 | -4.481    | -104.644 | 45.6       | 18                    | 0   |
| 6       | -4.565    | -106.323 | -6.12     | -106.85  | 173        | 151                   | 0   |
| 7       | -6.28     | -107.49  | -8.6      | -108.12  | 266.7      | 59                    | 0   |
| 8       | -8.95     | -109.775 | -13.4     | -111.35  | 522.9      | 21                    | 0   |

**Table 2.** Transform fault characteristics

| Transform  | Length<br>L<br>km | Full slip-<br>rate<br>V*<br>mm/yr | Brittle<br>area<br>A**<br>km <sup>2</sup> | No.<br>AUH<br>events | No. AUH<br>events/<br>A<br>km <sup>-2</sup> | No. AUH<br>events/<br>L<br>km <sup>-1</sup> | No. of<br>Segments | Segment<br>brittle area<br>A <sub>s</sub> ***<br>km <sup>2</sup> |
|------------|-------------------|-----------------------------------|---|----------------------|---|---|--------------------|--|
| Clipperton | 90                | 105.3                             | 326                                       | 129                  | 0.40  | 1.43  | 1                  | 326  |
| Siqueiros  | 140               | 111.9                             | 709.5                                     | 1356                 | 1.91  | 9.69  | 5                  | 277.2  |
| Quebrada   | 120               | 137.4                             | 450.75                                    | 1024                 | 2.27  | 8.53  | 4                  | 163.3  |
| Discovery  | 70                | 137.9                             | 196.7                                     | 586                  | 2.98  | 8.37  | 2                  | 121.4  |
| Gofar      | 190               | 138.8                             | 905.2                                     | 971                  | 1.07  | 5.11  | 3                  | 460.9  |
| Yaquina    | 60                | 141.4                             | 152                                       | 268                  | 1.76  | 4.47  | 2                  | 51.3   |
| Wilkes     | 180               | 145                               | 555                                       | 1505                 | 2.71  | 8.62  | 3                  | 364.9  |
| Garrett    | 130               | 149.8                             | 488                                       | 171                  | 0.35  | 1.32  | 4                  | 179.6  |

\*DeMets [1990]

\*\* The total brittle area of the transform fault is the area above the 600°C isotherm determined by a half-space cooling model for the given total transform fault length (L) and spreading rate (V).

\*\*\* Segmented brittle area is the sum of the areas above the 600°C isotherm determined by a half-space cooling model for each segment of a transform fault (A<sub>s</sub> given in Table 2).

**Table 3.** Transform fault segmentation characteristics

| Segment name        | Length<br>$L_s$<br>km | Brittle<br>area<br>$A_s$<br>$\text{km}^2$ | No.<br>AUH<br>events | No. AUH<br>events/<br>$A_s$<br>$\text{km}^{-2}$ | ITSC | $L_{\text{ITSC}}$<br>km |
|---------------------|-----------------------|---|----------------------|---|------|-------------------------|
| Siqueiros Transform |                       |   |                      |   |      |                         |
| S1                  | 33                    | 64.5                                      | 216                  | 3.35  | SA   | 18                      |
| S2                  | 42                    | 98.6                                      | 418                  | 4.24  | SB   | 8                       |
| S3                  | 24                    | 38  | 201                  | 5.29  | SC   | 5                       |
| S4                  | 23                    | 36.5                                      | 237                  | 6.49  | SD   | 5                       |
| S5                  | 25                    | 39.6                                      | 284                  | 7.17  |      |                         |
| Quebrada Transform  |                       |   |                      |   |      |                         |
| Q1                  | 40                    | 79  | 152                  | 1.92  | QA   | 7                       |
| Q2                  | 24                    | 34.4                                      | 231                  | 6.72  | QB   | 9                       |
| Q3                  | 22                    | 25.9                                      | 175                  | 6.76  | QC   | 10                      |
| Q4                  | 20                    | 24  | 466                  | 19.42   |      |                         |
| Discovery Transform |                       |   |                      |   |      |                         |
| D1                  | 30                    | 50  | 340                  | 6.80  | DA   | 6                       |
| D2                  | 37                    | 71.4                                      | 243                  | 3.40  |      |                         |
| Gofar Transform     |                       |   |                      |   |      |                         |
| G1                  | 49                    | 112                                       | 358                  | 3.20  | GA   | 11                      |
| G2                  | 35                    | 63.4                                      | 226                  | 3.56  | GB   | 20                      |
| G3                  | 89                    | 285.5                                     | 380                  | 1.33  |      |                         |
| Yaquina Transform   |                       |   |                      |   |      |                         |
| Y1                  | OSC                   |   | 40                   |   |      |                         |
| Y2                  | 31                    | 51.3                                      | 228                  | 4.44  |      |                         |
| Wilkes Transform    |                       |   |                      |   |      |                         |
| WN                  | Nannoplate            |   | 1435                 |   |      |                         |
| W1                  | 66                    | 34.8                                      | 395                  | 11.35   | WA   | 10                      |
| W2                  | 70                    | 236.3                                     | 1110                 | 4.70  |      |                         |
| Garrett Transform   |                       |   |                      |   |      |                         |
| G1                  | 18                    | 18.3                                      | 61                   | 3.33  | GA   | 17                      |
| G2                  | 34                    | 59.6                                      | 144                  | 2.42  | GB   | 15                      |
| G3                  | 22                    | 25.9                                      | 157                  | 6.06  | GC   | 15                      |
| G4                  | 40                    | 75.8                                      | 106                  | 1.40  |      |                         |

**Table 4.** OSC characteristics

| OSC    | Offset direction | Offset distance (km) | Overlap distance (km) | Overlap area (km <sup>2</sup> ) | AUH # | CMT # | AUH # /km <sup>2</sup> |
|--------|------------------|----------------------|-----------------------|---------------------------------|-------|-------|------------------------|
| 9.0°N  | right            | 9                    | 30                    | 270                             | 0     | 0     | 0                      |
| 7.2°N  | right            | 2                    | -                     | 2                               | 20    | 0     | 10.00                  |
| 5.5°N  | right            | 8                    | 13                    | 104                             | 9     | 0     | 0.09                   |
| 4.9°N  | right            | 5*                   | 20                    | 100                             | 1     | 0     | 0.01                   |
| 3.4°N  | right            | 13*                  | 9                     | 117                             | 69    | 0     | 0.59                   |
| 1.0°N  | left             | 5*                   | -                     | 5                               | -     | 0     | 0                      |
| 1.2°S  | left             | 4*                   | 6                     | 24                              | 8     | 0     | 0.33                   |
| 2.8°S  | left             | 27*                  | 21                    | 567                             | 65    | 2     | 0.11                   |
| 5.5°S  | right            | 15*                  | 11                    | 165                             | 129   | 0     | 0.78                   |
| 7.2°S  | right            | 6*                   | -                     | 6                               | 2     | 0     | 0.33                   |
| 9.6°S  | right            | 5*                   | 10                    | 50                              | 2     | 0     | 0.04                   |
| 10.9°S | right            | 6*                   | 13                    | 78                              | 6     | 0     | 0.08                   |

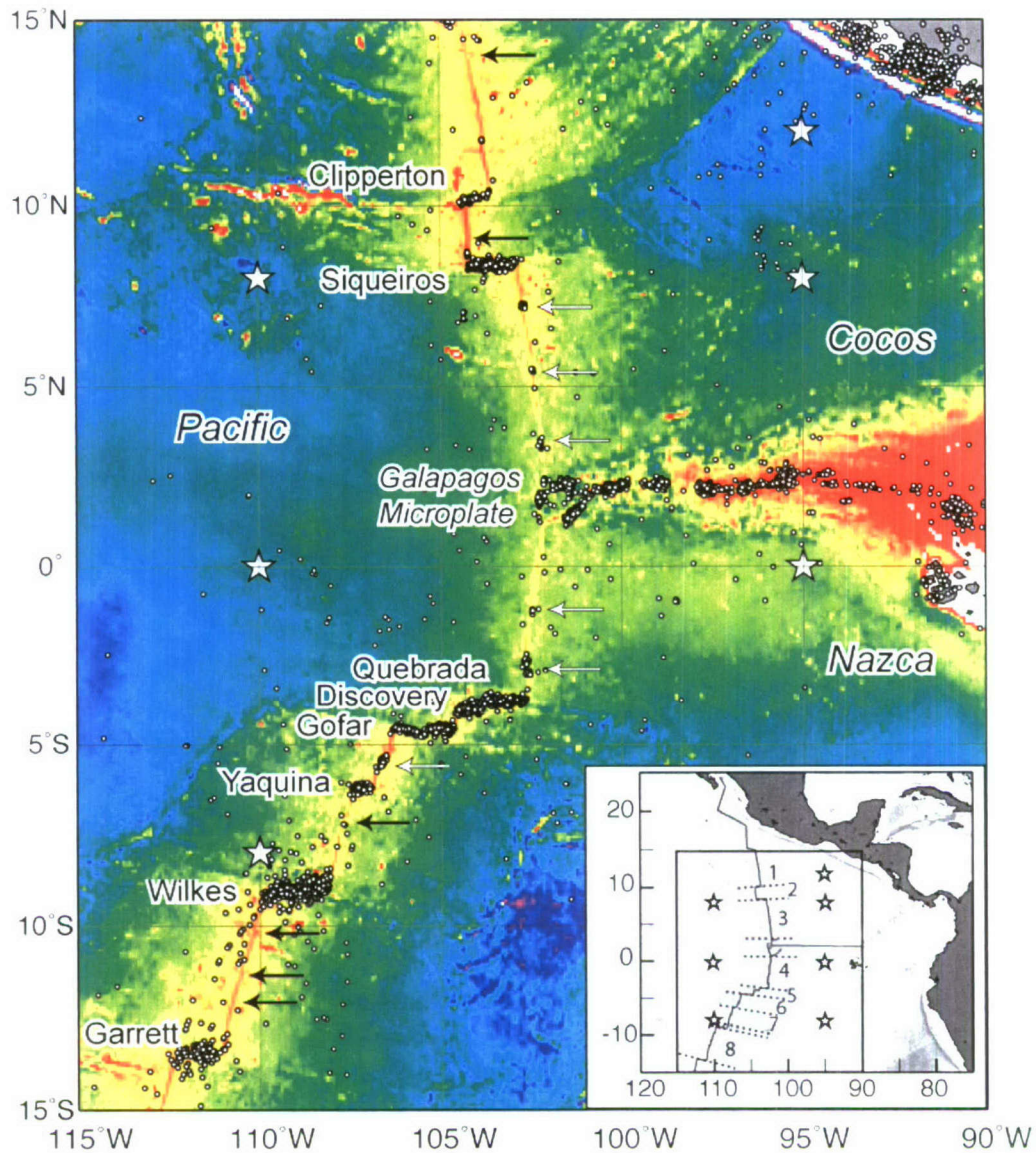
\* Data from *Lonsdale* [1989]

**Table 5.** Teleseismic and hydroacoustic events

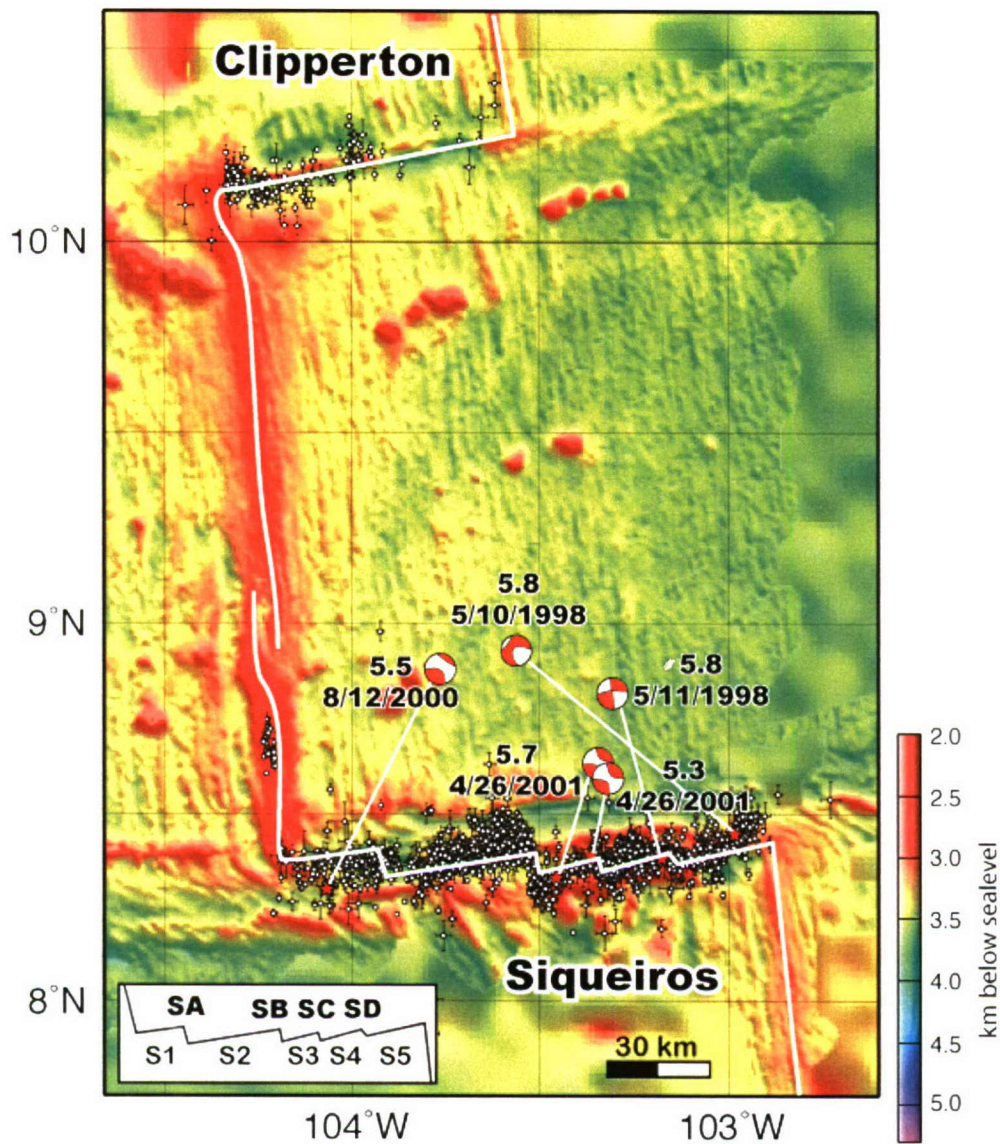
| Region       | Mw  | S L (dB) | Year | Jday | CMT Event |        |         | Hydrophone Event |        |         |         |
|--------------|-----|----------|------|------|-----------|--------|---------|------------------|--------|---------|---------|
|              |     |          |      |      | Time      | Lat    | Lon     | Time             | Lat    | Lon     | Phones  |
| Northern EPR |     |          |      |      |           |        |         |                  |        |         |         |
| Siqueiros    | 5.8 | 237.22   | 1998 | 130  | 6:35:51   | 8.93   | -103.56 | 6:35:50          | 8.45   | -102.98 | 12456   |
| Siqueiros    | 5.8 | 238.75   | 1998 | 131  | 1:34:40   | 8.82   | -103.30 | 1:34:42          | 8.38   | -103.18 | 12456   |
| Siqueiros    | 5.5 | 234.80   | 2000 | 225  | 14:13:15  | 8.87   | -103.76 | 14:13:11         | 8.30   | -104.07 | 23456   |
| Siqueiros    | 5.7 | 244.59   | 2001 | 116  | 18:59:56  | 8.59   | -103.33 | 19:00:00         | 8.33   | -103.46 | 1234567 |
| Siqueiros    | 5.3 | 240.90   | 2001 | 116  | 20:39:02  | 8.61   | -103.34 | 20:39:01         | 8.39   | -103.36 | 1234567 |
| Galapagos    | 5.3 | 203.52   | 2001 | 141  | 16:43:15  | 2.67   | -95.13  | 16:43:09         | 2.63   | -95.36  | 1234567 |
| Southern EPR |     |          |      |      |           |        |         |                  |        |         |         |
| 2.5SOSC      | 5.4 | 231.84   | 1998 | 169  | 19:03:45  | -2.85  | -102.57 | 19:03:45         | -2.90  | -102.57 | 12456   |
| 2.5SOSC      | 5.4 | 207.04   | 2001 | 298  | 9:04:47   | -2.70  | -102.69 | 9:04:49          | -2.70  | -102.65 | 1234567 |
| Discovery    | 5.9 | 236.76   | 1996 | 236  | 21:56:13  | -3.80  | -104.40 | 21:56:16         | -3.99  | -104.40 | 12346   |
| Discovery    | 5.8 | 236.88   | 1996 | 236  | 22:19:04  | -3.86  | -104.25 | 22:19:01         | -4.01  | -104.25 | 12346   |
| Discovery    | 5.5 | 224.35   | 1998 | 319  | 4:51:49   | -3.62  | -104.23 | 4:53:25          | -4.01  | -104.17 | 12456   |
| Discovery    | 6   | 249.68   | 2001 | 177  | 12:34:00  | -3.82  | -104.32 | 12:34:00         | -3.95  | -104.40 | 1234567 |
| Discovery    | 5.6 | 236.93   | 2001 | 211  | 4:34:51   | -3.85  | -104.04 | 4:34:50          | -4.03  | -103.98 | 1234567 |
| Garrett      | 5.7 | 236.42   | 1999 | 276  | 2:10:22   | -13.33 | -111.18 | 2:10:11          | -13.83 | -111.46 | 12356   |
| Garrett      | 5.2 | 237.75   | 2001 | 222  | 23:49:42  | -13.50 | -112.02 | 23:49:42         | -13.43 | -111.74 | 1234567 |
| Gofar        | 5.6 | 233.65   | 1997 | 84   | 8:09:25   | -4.48  | -105.49 | 8:09:28          | -4.65  | -105.55 | 123456  |
| Gofar        | 5.7 | 235.64   | 1997 | 97   | 17:53:05  | -4.46  | -105.26 | 17:53:09         | -4.60  | -105.28 | 123456  |
| Gofar        | 6.2 | 237.84   | 1997 | 227  | 7:37:56   | -4.39  | -105.95 | 7:38:07          | -4.61  | -105.92 | 123456  |
| Gofar        | 5.5 | 236.91   | 1999 | 261  | 4:01:11   | -4.19  | -104.84 | 4:01:38          | -4.60  | -104.82 | 12356   |
| Gofar        | 5.4 | 229.87   | 2000 | 294  | 19:47:30  | -4.70  | -106.04 | 19:47:22         | -4.56  | -105.90 | 23456   |
| Wilkes       | 5.3 | 235.61   | 1997 | 133  | 0:56:49   | -8.92  | -109.86 | 0:56:48          | -9.07  | -109.82 | 1245    |
| Wilkes       | 5.4 | 235.21   | 1997 | 202  | 7:46:48   | -8.67  | -108.00 | 7:46:39          | -9.01  | -108.27 | 12345   |
| Wilkes       | 5.4 | 238.17   | 1998 | 281  | 7:36:33   | -8.93  | -109.78 | 7:36:19          | -9.08  | -109.79 | 12456   |
| Wilkes       | 5.3 | 237.67   | 1999 | 90   | 23:18:12  | -8.60  | -109.51 | 23:18:11         | -9.24  | -109.68 | 12456   |
| Wilkes       | 5.5 | 206.47   | 2001 | 260  | 16:43:47  | -8.86  | -109.42 | 16:43:44         | -9.08  | -109.56 | 1234567 |
| Yaquina      | 5.3 | 236.23   | 1996 | 218  | 20:27:42  | -6.07  | -107.16 | 20:27:44         | -6.22  | -107.24 | 12346   |
| Yaquina      | 5.5 | 235.83   | 1999 | 314  | 2:25:46   | -6.16  | -107.16 | 2:25:58          | -6.21  | -107.23 | 12345   |



## FIGURES

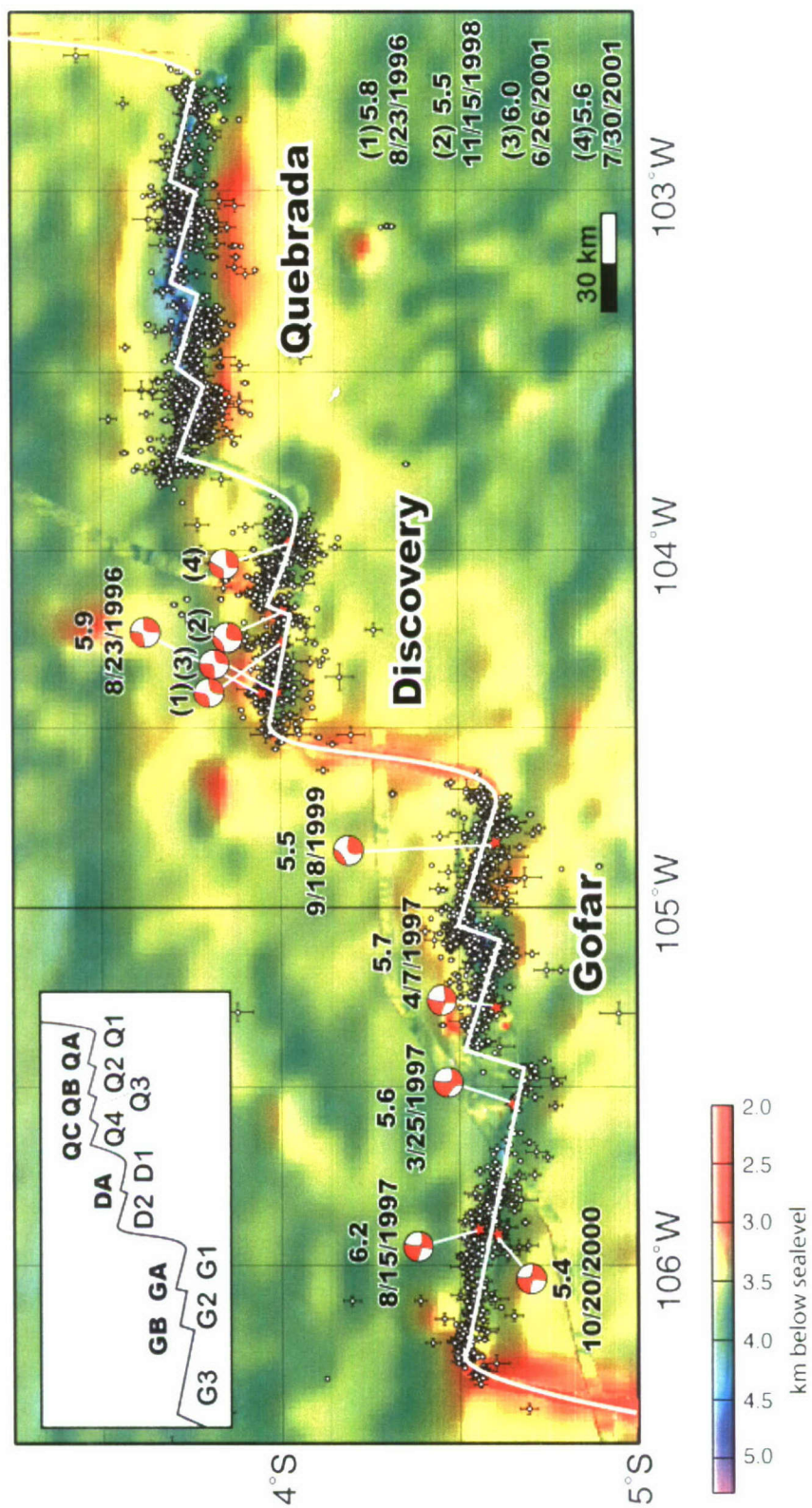


**Figure 1.** Location Map of the equatorial EPR showing the location of the NOAA/PMEL Equatorial Pacific hydrophone array and major tectonic features. The locations of the seven hydrophones are marked by white stars. White circles indicate the location of seismic events recorded by the AUH catalog from May 1996 to November 2001. Overlapping spreading center (OSC) locations are marked by white arrows (seismically active) and black arrows (no seismicity). Inset: Location of the study area. Dashed black lines and numbers illustrate the first-order segmentation of the EPR within the study area (Table 1).



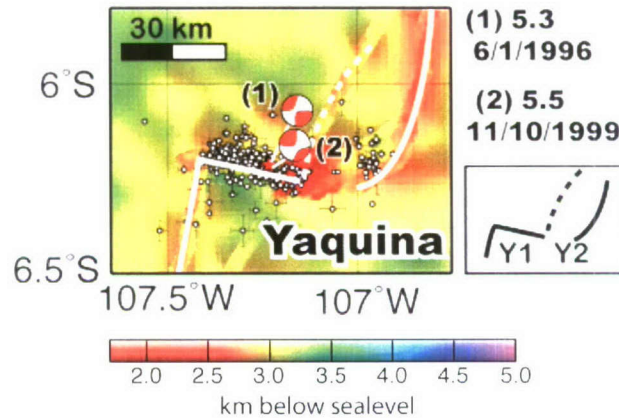
**Figure 2.** The Clipperton and Siqueiros transform systems. Plate boundary is delineated by the white line. Insert: The segmentation of the Siqueiros transform is shown as five fault segments, S1, S2, S3, S4, and S5, and four ITSCs, SA, SB, SC, SD, (data from *Fornari et al.* [1989]). White circles indicate location of AUH recorded seismicity. Error bars are given by the NOAA/PMEL source location error. CMT focal mechanisms are shown in red. Relocation to AUH-recorded event is shown by red stars.



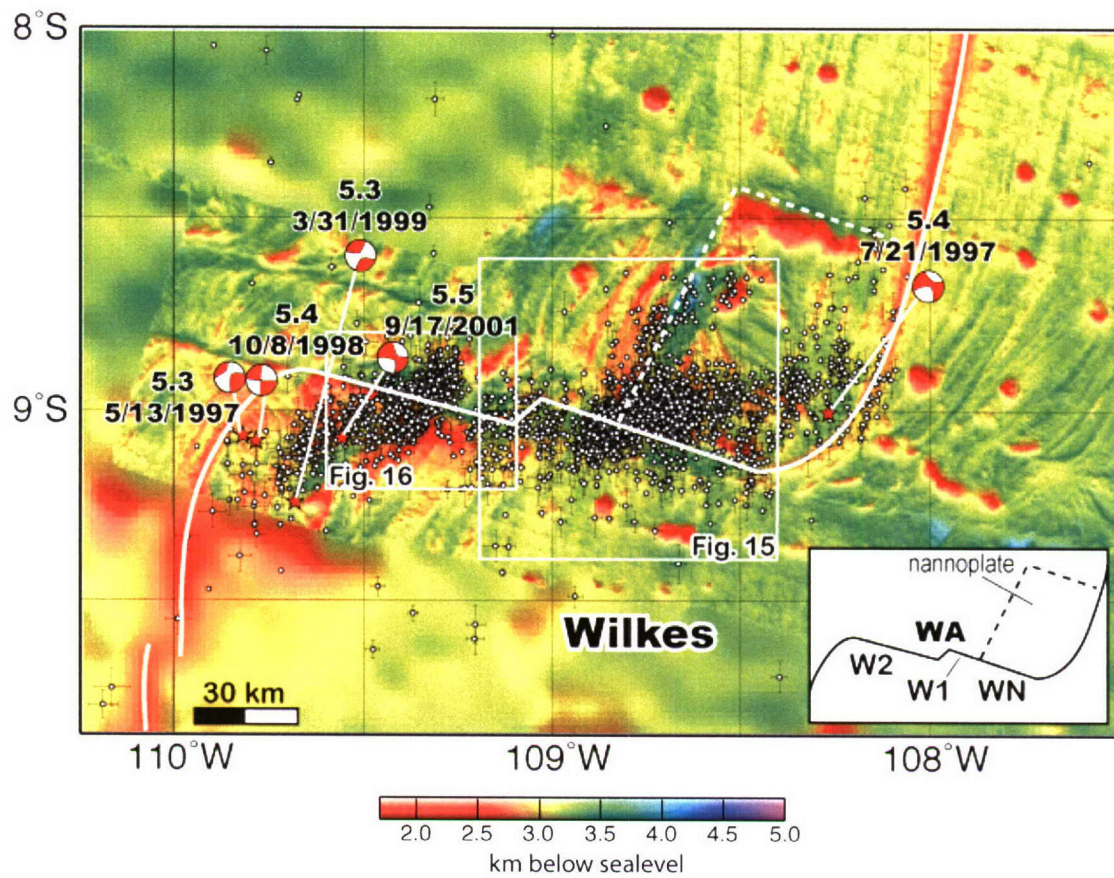




**Figure 3.** The Quebrada, Discovery, and Gofar transform fault systems. Plate boundary is delineated by the white line, and the geometry of the segmented systems (shown in the inset) is labeled from north to south from the plate boundary data given by *Searle* [1983]. White circles indicate location of AUH-recorded seismicity. Error bars are given by the NOAA/PMEL source location error. CMT focal mechanisms are shown in red. Relocation to AUH-recorded event is shown by red stars.

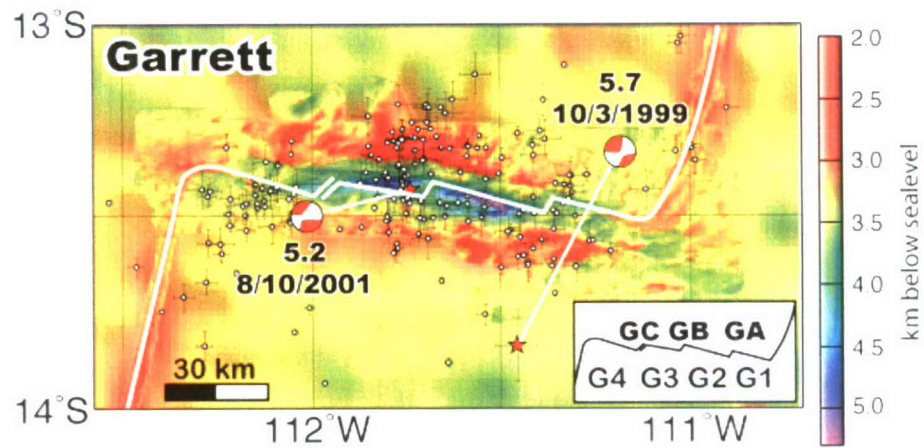


**Figure 4.** The Yaquina transform fault system. Plate boundary is delineated by the white line. The hybrid transform fault geometry (shown at the right panel) is from the plate boundary given by *Lonsdale* [1989]. White circles indicate location of AUH-recorded seismicity. Error bars are given by the NOAA/PMEL source location error. CMT focal mechanisms are shown in red. Relocation to AUH-recorded event is shown by red stars.

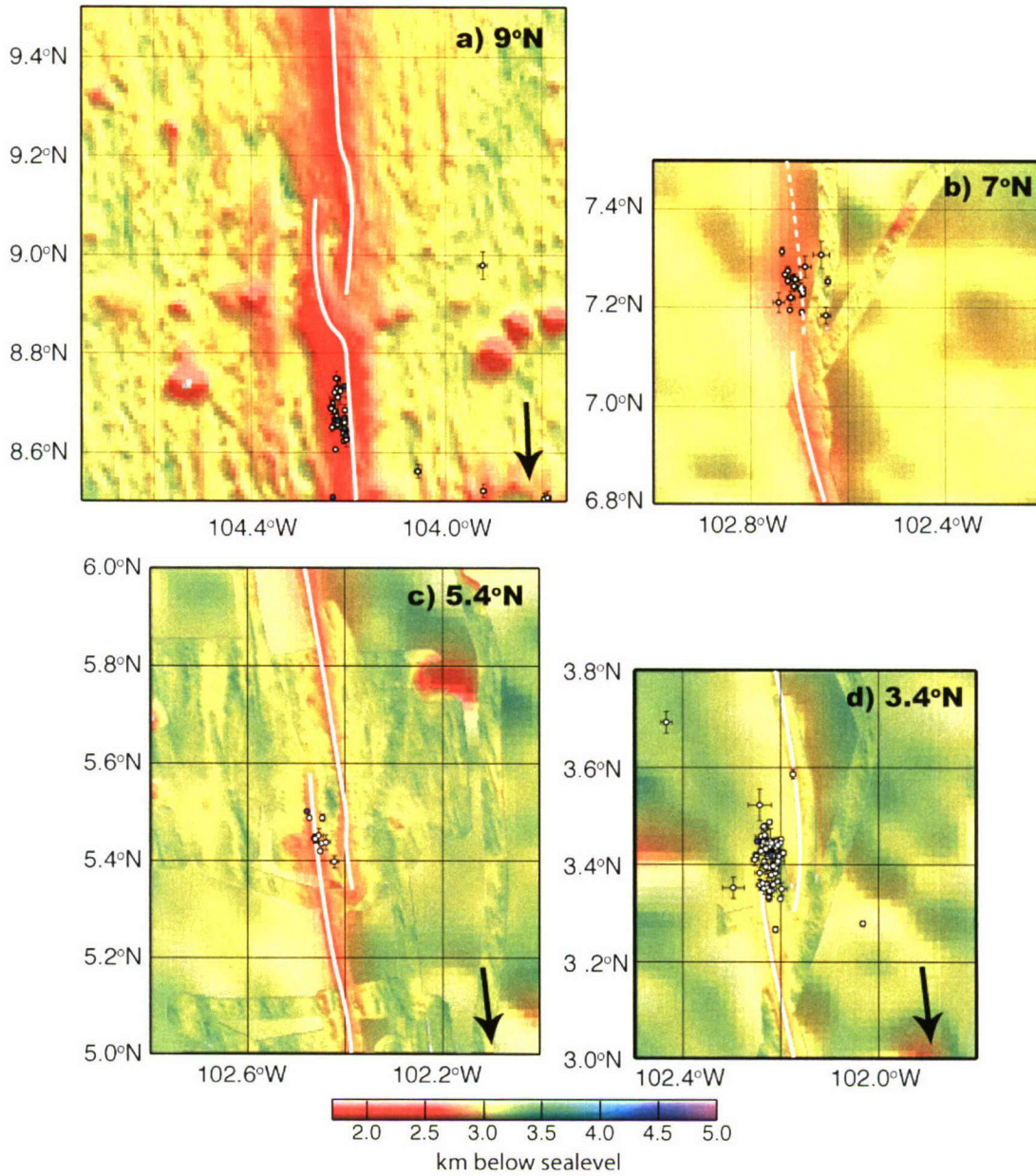


**Figure 5.** The Wilkes transform fault system. Plate boundary is delineated by the white line, and the geometry of the segmented systems (shown in the inset) is from the plate boundary data given by *Goff et al.* [1993]. White circles indicate location of AUH-recorded seismicity. Error bars are given by the NOAA/PMEL source location error. CMT focal mechanisms are shown in red. Relocation to AUH-recorded event is shown by red stars. White boxes indicate the regions shown in Figures 15 and 16.

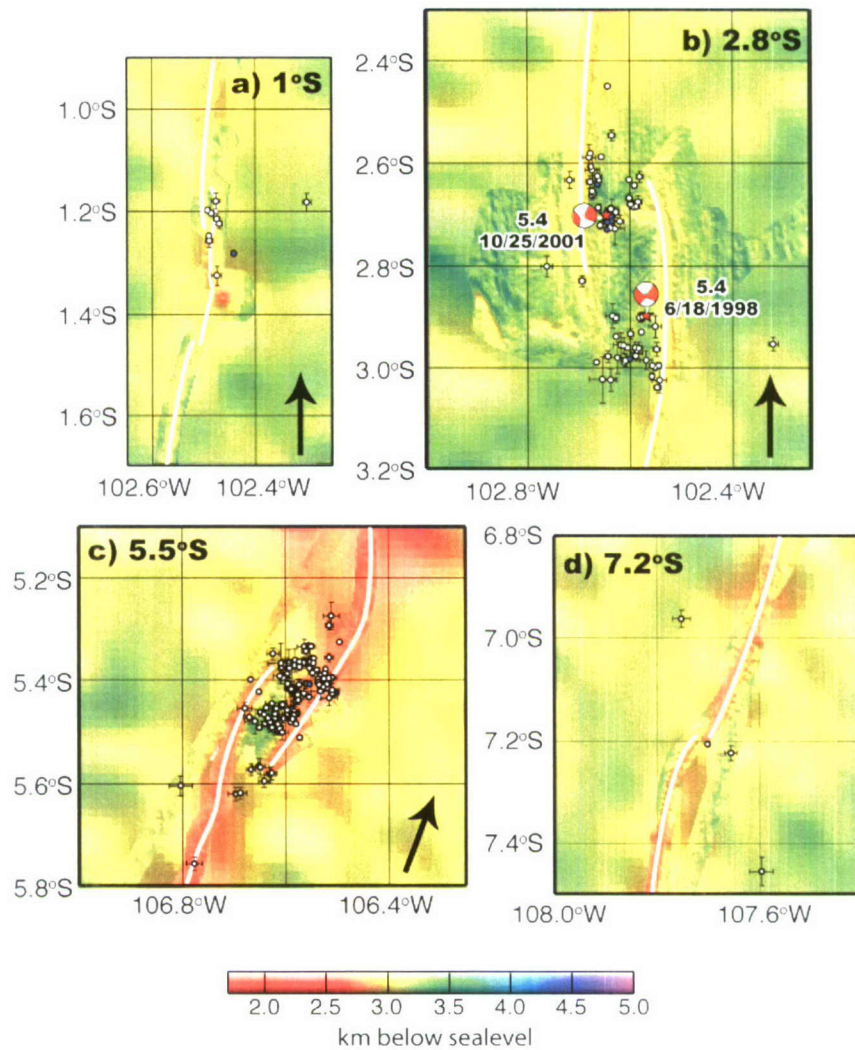




**Figure 6.** The Garrett transform fault system. Plate boundary is delineated by the solid white line, and the geometry of the segmented systems (shown in the inset) is labeled from north to south [Hekenian *et al.*, 1992]. White circles indicate location of AUH-recorded seismicity. Error bars are given by the NOAA/PMEL source location error. Events recorded in the CMT catalog with CMT source locations are given by the focal mechanisms. Relocation to AUH recorded event is shown by red stars.

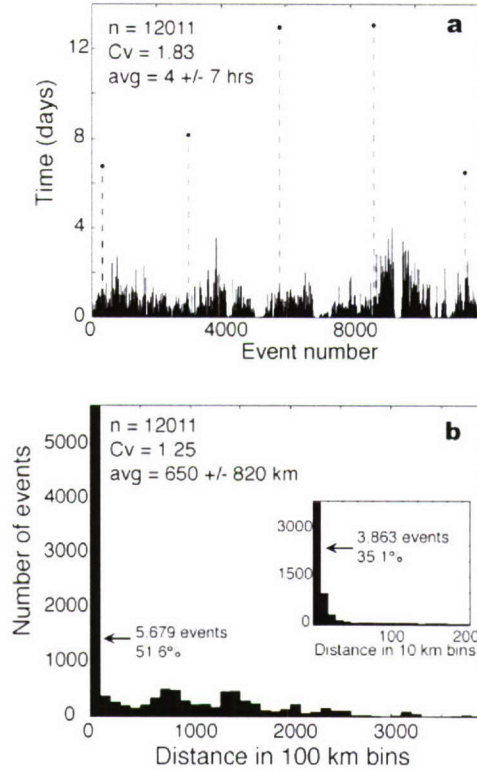


**Figure 7.** Northern OSCs. Plate boundary is delineated by the white solid line. In panel (b) dashed white line indicates the estimated plate boundary of *Lonsdale* [1985] based on off-axis segmentation. White circles indicate location of AUH-recorded seismicity, and blue circles indicate source levels large enough to be recorded in the REB catalog. Error bars are given by the NOAA/PMEL source location error. Black arrows indicate the direction of ridge propagation.

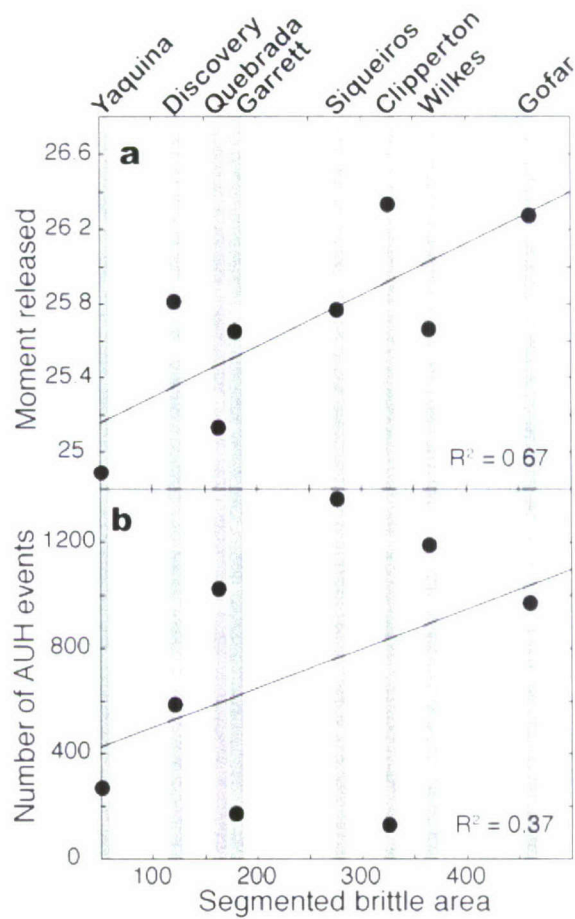


**Figure 8.** Southern OSCs. Plate boundary is delineated by the white solid line. White circles indicate location of AUH-recorded seismicity, and blue circles indicate source levels large enough to be recorded in the REB catalog. Error bars are given by the NOAA/PMEL source location error. Black arrows indicate the direction of ridge propagation. CMT focal mechanisms are shown in red. Relocation to AUH-recorded event is shown by red stars.

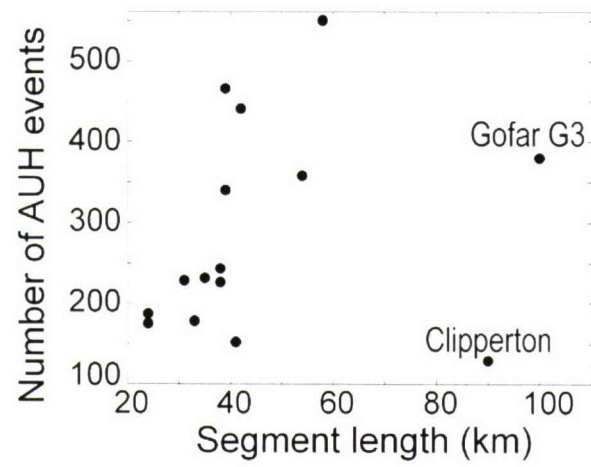




**Figure 9.** Temporal and spatial statistics of the T-phase catalog of AUH events. (a) Inter-event times of AUH events within our study region: Small inter-event times indicate earthquakes occurring closely spaced in time. Large inter-event times indicate a slower seismicity rate. The coefficient of variation ( $Cv$ ) describes the tendency for earthquakes in our study area to cluster temporally.  $Cv$  is defined as the standard deviation of the inter-event times divided by the mean inter-event time. Values for  $Cv$  are 0 for a periodic data set, 1 for Poissonian (random), and  $> 1$  for clustered processes [Kegan and Jackson, 1991]. (b) Inter-event distances of AUH events within our study region. Inter-event distances are grouped in bins of 100 km. Approximately 55% of recorded earthquakes occur within 0-100 km of each other. (inset) Inter-event distances grouped in bins of 10 km. This graph is zoomed in to the events occurring within distances of 250 km of each other to illustrate the large portion of events (nearly 1/3) that occur within 10 km.  $Cv$  is calculated to show the tendency of earthquakes to cluster spatially within our study area.

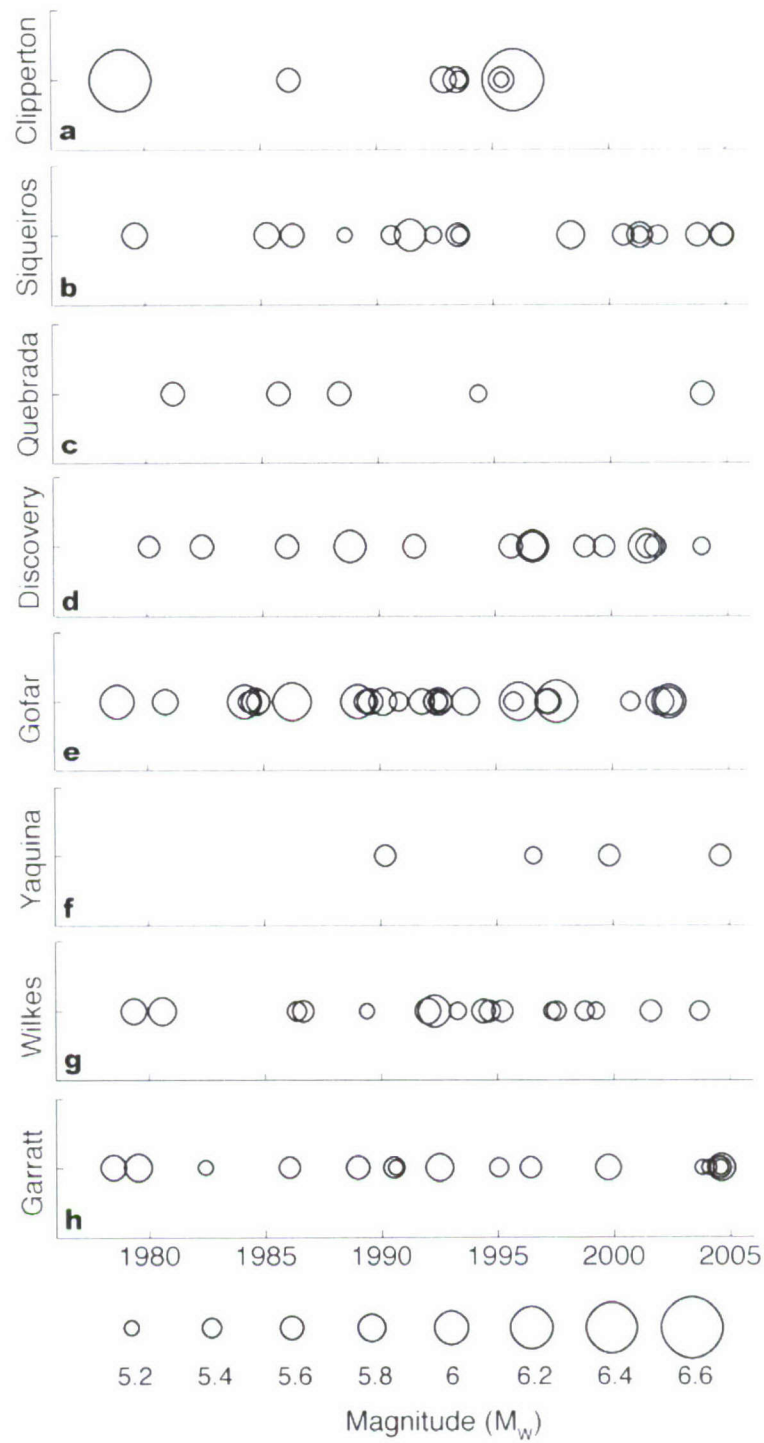


**Figure 10.** The relationship between the brittle area of the transform fault, given by the segmented brittle area in Table 2, with (a) total seismic moment released,  $M_0$ , as recorded in the CTM catalog and (b) total number of recorded AUH events. Linear fit is shown by solid lines, with the corresponding  $R^2$  fit values given.

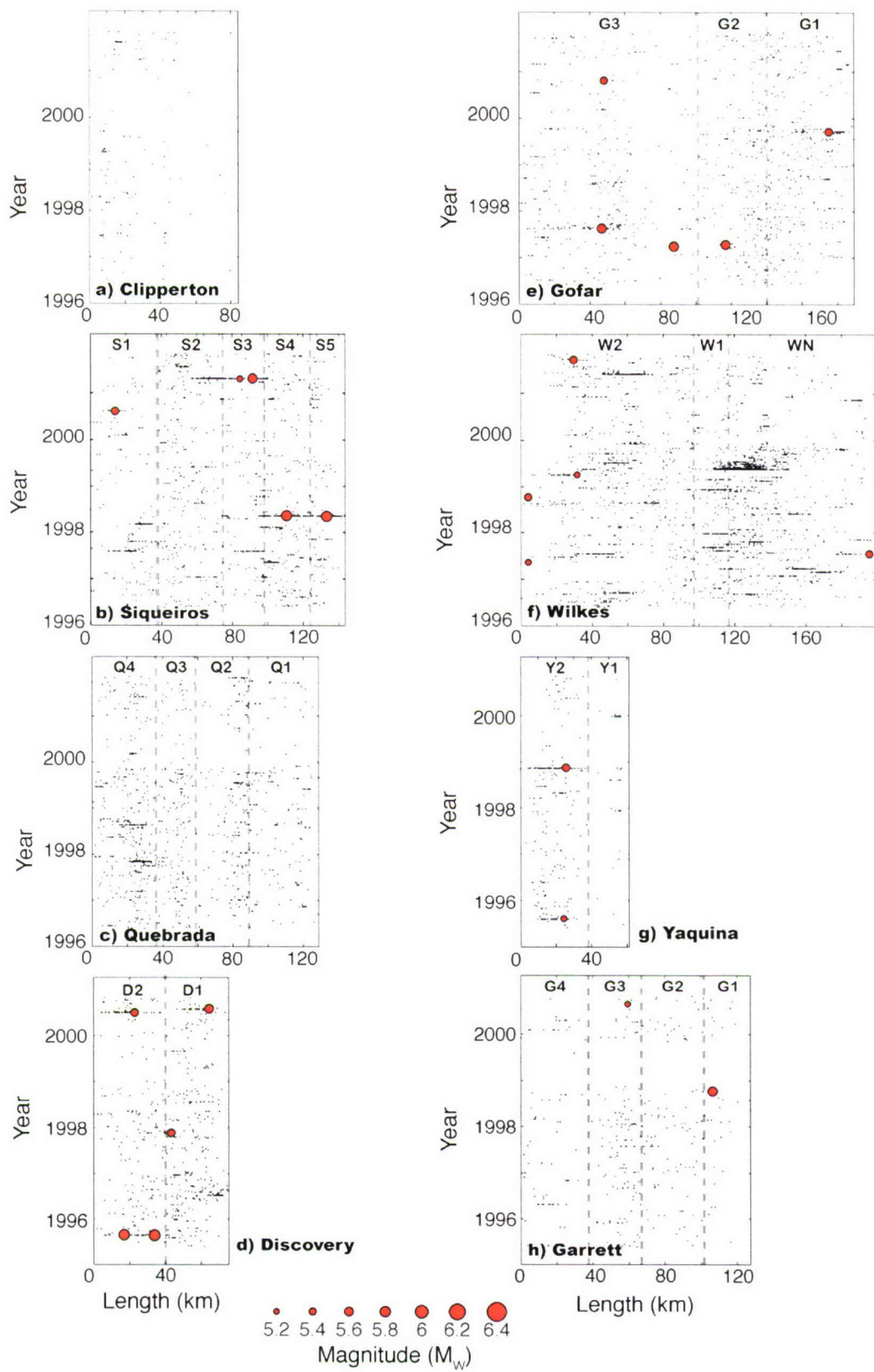


**Figure 11.** Number of recorded AUH events vs. transform fault segment length (Table 3).



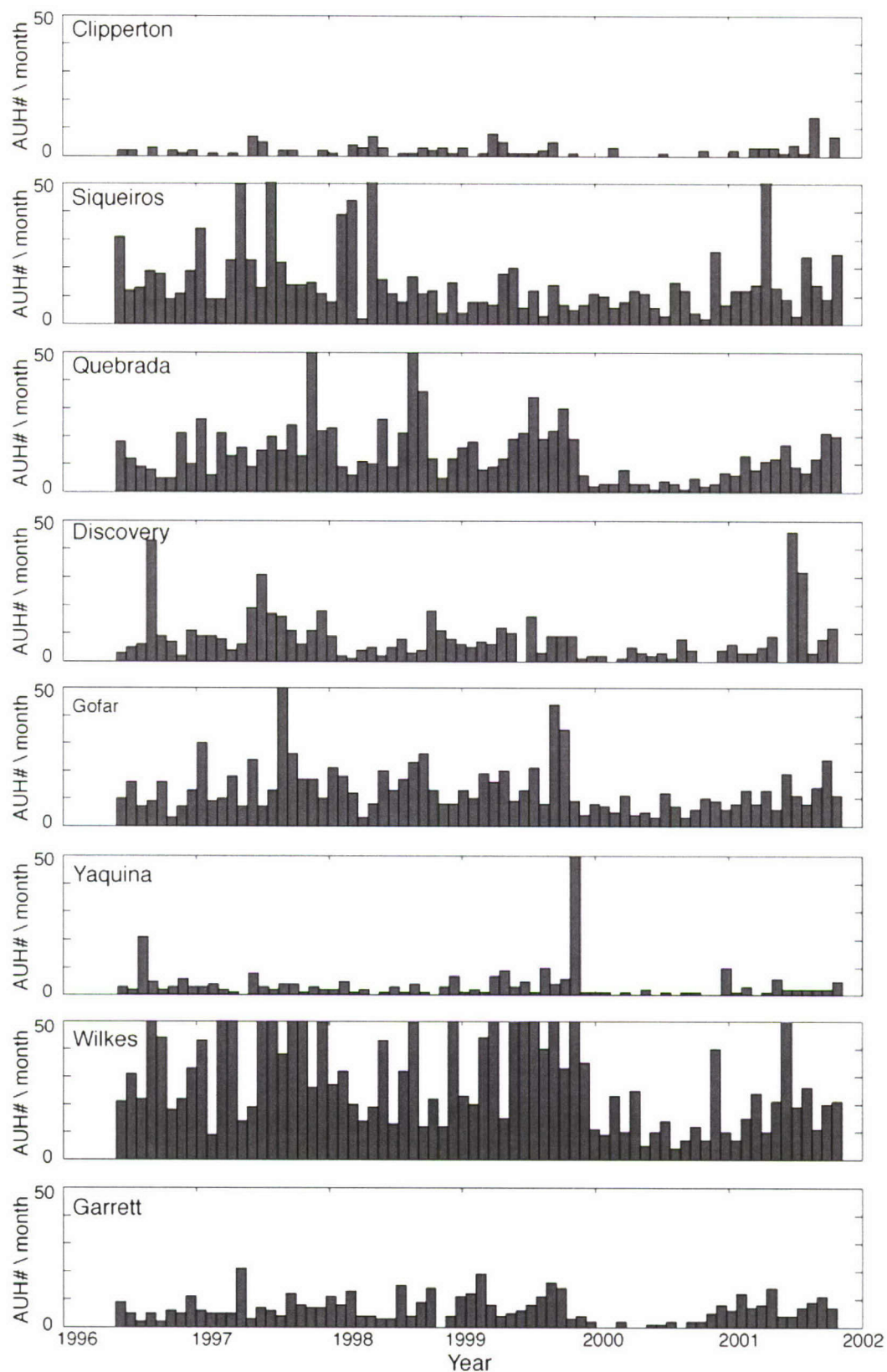


**Figure 12.** Earthquakes recorded in the CMT for each transform fault from 1976-2006. Event size is scaled based on CMT recorded magnitude ( $M_w$ ).

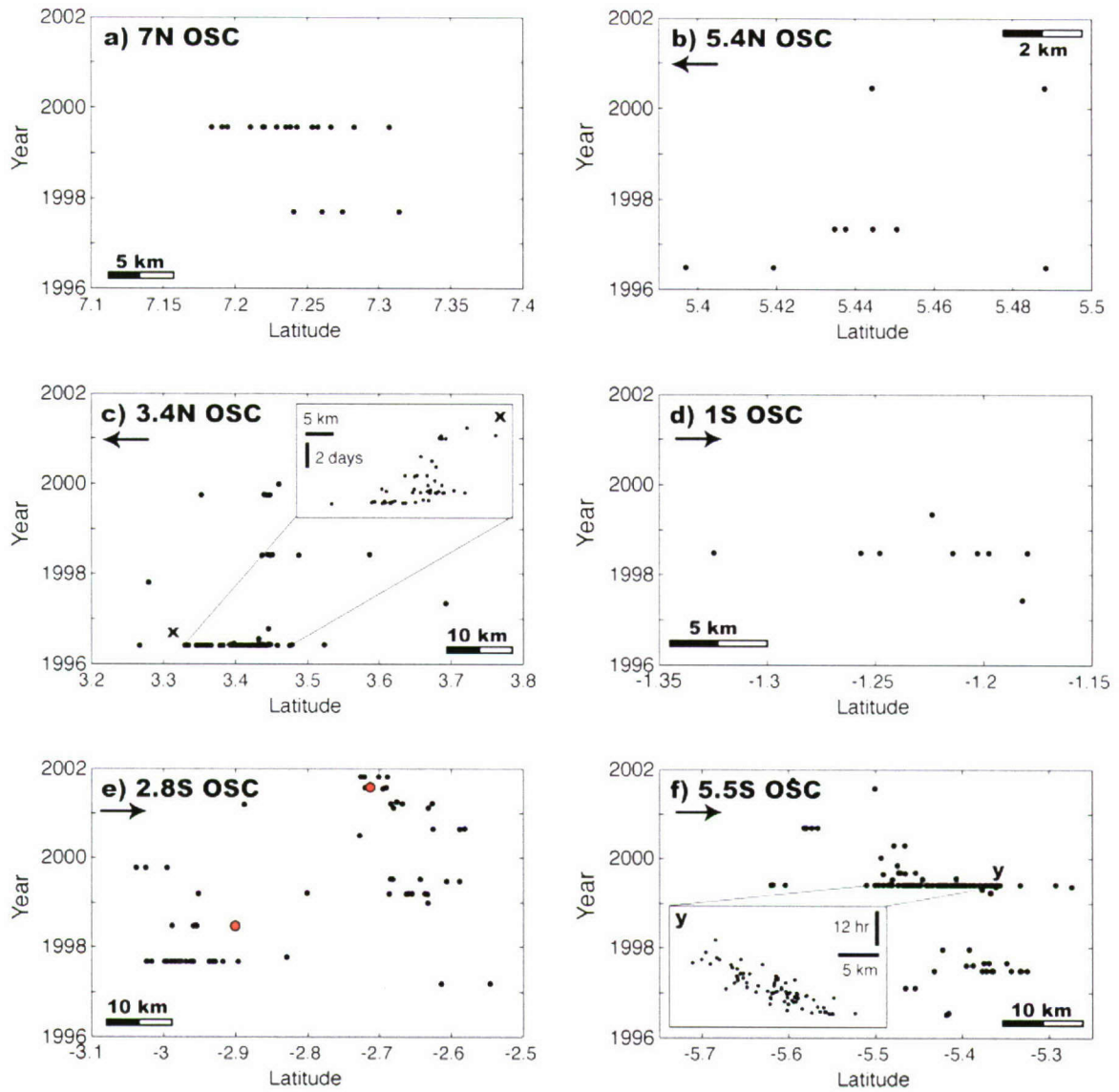


**Figure 13.** Recorded AUH events for each transform fault over the study period (1996-2002) plotted as their projected along-transform location. Earthquakes are projected back to the transform fault using Euler pole location and great circle rotation for each transform fault. ITSC location for each transform fault is indicated by the gray dashed lines. CMT recorded events are given by red circles, scaled to their recorded magnitude.



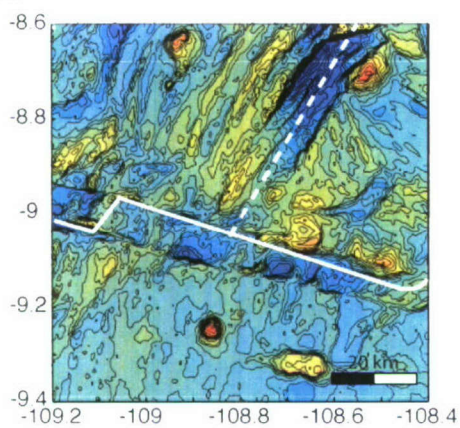
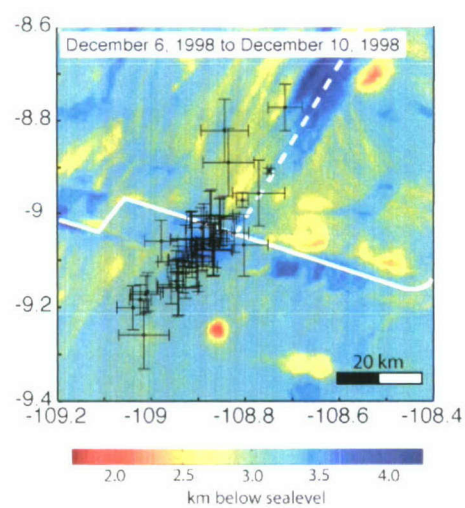
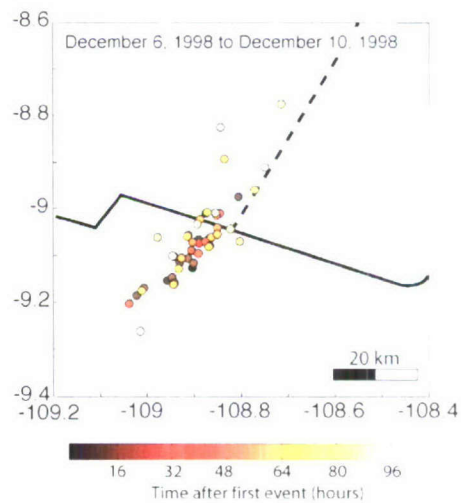
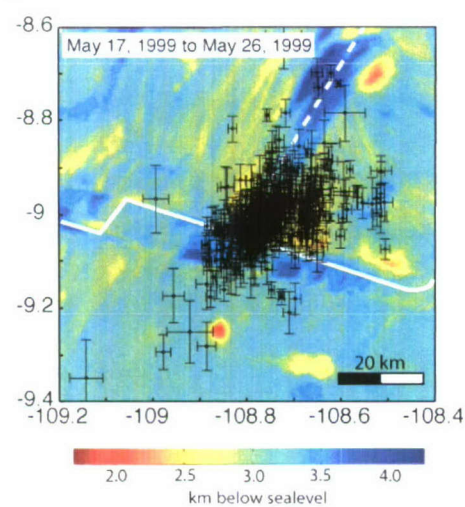
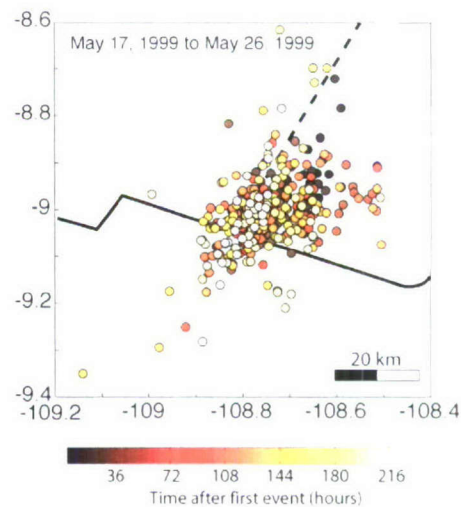


**Figure 14.** Time distribution of AUH events on each of the transform faults shown by 1 month bins. (Still need to add CMT events and increase y-axis)



**Figure 15.** OSC latitude vs. the timing of all recorded AUH events at each OSC to show rate and migration of seismicity. Black arrows indicate the propagation direction for each OSC. Insets in (c) and (f) are blowups of particular event sequences x and y, respectively, illustrating migration of earthquakes.



**a****b****c****d****e**

**Figure 16.** Two earthquake sequences recorded on the Wilkes nanoplate boundary: (b) and (c), December 6-10, 1998; and (d) and (e), May 17-26, 1999. Plate boundary is indicated by the solid white line (a, b, and d) and solid black line (c and e). Dashed white line (a, b, and d) and dashed black line (c and e) marks the location of the Wilkes nanoplate as discussed in *Goff et al.* [1993]. Earthquake locations are given by dots in panels (b) and (d) with location errors shown. Panels (c) and (e) illustrate the time progression of each earthquake sequence.

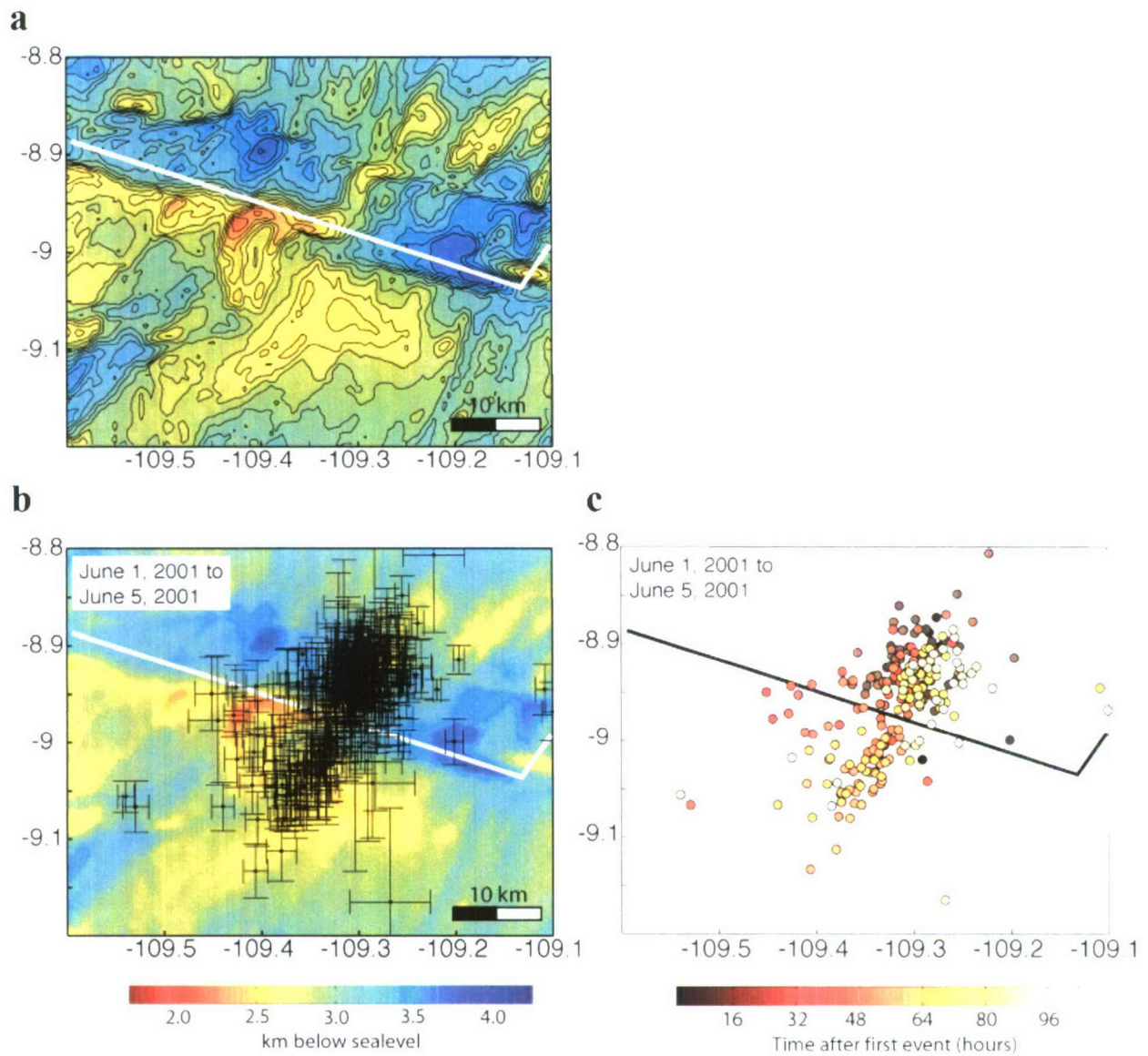


**Figure 17.** The June 1-5, 20001 seismicity sequence along the W2 segment of the Wilkes transform fault system. Plate boundary is indicated by the solid white line (a and b) and solid black line (c). (b) Earthquake locations, dots, with location errors shown. (c) Time progression of the earthquake sequence.



|   |  |  |  |
|---|--|--|--|
| <b>REPORT DOCUMENTATION PAGE</b>  | <b>1. REPORT NO.</b><br>MIT/WHOI 2008-06 | <b>2.</b>  | <b>3. Recipient's Accession No.</b>                            |
| <b>4. Title and Subtitle</b><br>The Dynamics of Oceanic Transform Faults: Constraints from Geophysical, Geochemical and Geodynamical Modeling   |  |  | <b>5. Report Date</b><br>June 2008                             |
| <b>7. Author(s)</b><br>Patricia Michelle Marie Gregg  |  |  | <b>6.</b>  |
| <b>9. Performing Organization Name and Address</b><br><br>MIT/WHOI Joint Program in Oceanography/Applied Ocean Science & Engineering  |  |  | <b>8. Performing Organization Rept. No.</b>                    |
| <b>12. Sponsoring Organization Name and Address</b><br>National Science Foundation Graduate Research Fellowship<br>WHOI Academic Programs Office  |  |  | <b>10. Project/Task/Work Unit No.</b><br>MIT/WHOI 2008-06      |
|   |  |  | <b>11. Contract(C) or Grant(G) No.</b><br>(C)<br>(G)           |
| <b>15. Supplementary Notes</b><br>This thesis should be cited as: Patricia Michelle Marie Gregg, 2008. The Dynamics of Oceanic Transform Faults: Constraints from Geophysical, Geochemical and Geodynamical Modeling. Ph.D. Thesis. MIT/WHOI, 2008-06.  |  |  | <b>13. Type of Report &amp; Period Covered</b><br>Ph.D. Thesis |
|   |  |  | <b>14.</b>   |
| <b>16. Abstract (Limit: 200 words)</b><br>Segmentation and crustal accretion at oceanic transform fault systems are investigated through a combination of geophysical data analysis and geodynamical and geochemical modeling. In Chapter 1, results of thermal modeling suggest that fault segmentation by intra-transform spreading centers (ITSC) drastically reduces the available brittle area of a transform fault and thus limits the available earthquake rupture area. Coulomb stress models illustrate that long ITSCs will prohibit static stress interaction between segments of a transform system and further limit the maximum possible magnitude of a given transform fault earthquake. In Chapter 2, residual mantle Bouguer gravity anomalies are investigated from a global set of oceanic transform fault systems. Negative anomalies are found within fast-slipping transform fault domains suggesting a mass deficit in these settings, which may be due to crustal thickness excesses in these locations. Finally, in Chapter 3, mantle thermal models for a viscoplastic rheology are developed to investigate the process of mantle melting and crustal accretion at ITSCs within segmented transform faults, and applied to the Siqueiros transform fault. Models in which melt migrates into the transform fault domain from a large region of the mantle best explain the gravity-derived crustal thickness variations observed at the Siqueiros transform. |  |  |  |
| <b>17. Document Analysis</b>  |  |  |  |
| <b>a. Descriptors</b><br>Transform<br>Fault<br>Siqueiros  |  |  |  |
| <b>b. Identifiers/Open-Ended Terms</b>  |  |  |  |
| <b>c. COSATI Field/Group</b>  |  |  |  |
| <b>18. Availability Statement</b><br>Approved for publication; distribution unlimited.  |  | <b>19. Security Class (This Report)</b><br><b>UNCLASSIFIED</b> | <b>21. No. of Pages</b><br>133                                 |
|   |  | <b>20. Security Class (This Page)</b>                          | <b>22. Price</b>   |